Search for the Standard Model Higgs Boson at $D\emptyset$ in the Final State with Two τ's and Two Jets

A Dissertation Presented

by

Kathryn Ann Tschann-Grimm

to

The Graduate School

in Partial Fulfillment of the

Requirements

for the Degree of

Doctor of Philosophy

in

Physics

Stony Brook University

August 2011

Stony Brook University

The Graduate School

Kathryn Ann Tschann-Grimm

We, the dissertation committee for the above candidate for the **Doctor of Philosophy** degree, hereby recommend acceptance of this dissertation.

Professor Paul Grannis, Thesis Advisor
Department of Physics

Professor Rod Engelmann, Chairman of the defense committee
Department of Physics

Professor Patrick Meade
C. N. Yang Institute of Theoretical Physics

Dr. Hong Ma, Outside member
Brookhaven National Lab
Upton, NY

This dissertation is accepted by the Graduate School.

Lawrence Martin
Dean of the Graduate School

Abstract of the Dissertation

Search for the Standard Model Higgs Boson at $D\emptyset$ in the Final State with Two τ's and Two Jets

by

Kathryn Ann Tschann-Grimm

Doctor of Philosophy

in

Physics

Stony Brook University

2011

The Standard Model (SM) is a very successful description of particle physics, and its predictions have stood up to a multitude of precision experimental tests. But one of the central elements of the SM, the Higgs mechanism, has yet to be verified. The Higgs mechanism (and the associated Higgs Boson) generates electroweak symmetry breaking and consequently allows for W and Z bosons and fermions to be massive. This thesis presents a search for the SM Higgs boson at the $D\emptyset$ experiment using the Tevatron particle accelerator at Fermilab in the final state $\tau\tau$ + jet jet with 4.3 fb^{-1} of data. This final state is sensitive to the Higgs production mechanisms gluon-gluon fusion and vector-boson fusion, and to the Higgs produced in association with a W or Z, for Higgs masses from 100 to 200 GeV. We see no evidence for the Higgs boson, but by itself our search does not rule out the SM Higgs. When this analysis is combined with other searches at the Tevatron the Higgs can be ruled out at a 95% confidence level for the mass range from 156 to 177 GeV.

Contents

List of Figures

List of Tables

List of Abbreviations and Terms

- Cross section: a measure of the probability of a particular particle interaction. It has the units of length squared (or Energy squared).
- eV: electron (e) volt (V), the unit of energy used in particle physics. An electron volt is defined as the energy required to accelerate an electron through a potential difference of one volt. In this thesis the standard energies are quoted in giga electron volts, or GeV. For convenience, units are quoted with the assumption that c, the speed of light, and $\hbar$, Planck's constant, are 1, so that masses and momentums are also quoted in terms of eV or GeV.
- KS test: The Kolmogorov Smirnov test is a measure of how well the shape of two distributions match. Unlike a χ^2, the KS test aims to disregard differences in absolute normalization between two distributions. A full description is given here: [1]
- Luminosity: relates the event rate to the interaction cross section at a collider. It is given by,
$$\mathcal{L} = f\frac{n_1 n_2}{4\pi\sigma_x\sigma y} \tag{1}$$
where n_1 and n_2 are the number of particles in the colliding bunches, f is the frequency of collision, and σ_x and σ_y characterize the Gaussian transverse beam profiles in the horizontal and vertical directions [5].
- MET: Abbreviation for Missing Transverse Energy (also, $\not\!\!E_T$), which is used to account for neutrino transverse energy. This is described in section 2.3.12.
- pion (π): a meson made of up (u) and down (d) quarks. It can be negatively charged ($d\overline{u}$), positively charged ($u\overline{d}$), or neutral ($\frac{1}{\sqrt{2}}(u\overline{u}+d\overline{d})$)
- p_T: the transverse momentum. This quantity is invariant to boosting in the beam direction and is conserved in observed particle collisions at DØ or ATLAS because of the $4\ \pi$ coverage of the detectors.

Coordinates:

- Z_{vtx}: The distance from the interaction point along the beam line.
- ϕ: The direction perpendicular to the beam. Following the coordinates in Fig. 2.3 this is the angle in the $x-y$ plane. The ϕ=0 reference is defined as the $+y$ direction (straight up from the floor of the detector hall) and ϕ=π is the $-y$ direction (straight down to the floor).
- η: the pseudorapidity. Using the spherical coordinates r, θ, ϕ, the pseudorapidity is defined as $\eta = -ln[tan(\frac{\theta}{2})]$. The variable θ is defined such that $\theta = 0^\circ$ is the direction of the proton beam, and $\theta = 180^\circ$ is the direction of the anti-proton beam. Consequently large positive values of η are in the direction of the proton beam, large negative values of η are in the direction of the antiproton beam and η of 0 is perpendicular to the beam at the interaction point. In the limit where particle mass goes to zero, the pseudorapidity is close to the rapidity, defined as

$$y = \frac{1}{2} ln(\frac{E + p_L}{E - p_L}) \tag{2}$$

  where p_L is the component of the momentum along the beam direction. Rapidity differences are invariant to Lorentz boosting along the beam direction.
- ΔR in detector space is $\Delta\eta \oplus \Delta\phi$ ($\oplus$ indicates sum in quadrature)

Acknowledgements

I would like to sincerely thank the many people at Stony Brook, BNL, CERN, and Fermilab who helped me during graduate school.

Thanks to Rod, for all his help on ATLAS. Many thanks to Katie, Adam, and Moustapha for endless help with banks, bread, cars, physics when I arrived in France. And big thanks to Subhendu and Paul for their patience, attention and goodwill as we worked on the Higgs analysis– it has been a pleasure to work with with them.

And thank you to Jason for the constant support throughout grad school.

0.1 Introduction

This thesis describes the search for the Standard Model Higgs boson at DØ in the final state with two taus and two jets. The theoretical motivation for the Higgs boson is described first, along with theoretical bounds on the Higgs mass. Then a description of the Tevatron and DØ is given, followed by the presentation of the tau tau jet jet Higgs search.

There is also a section describing the calibration of the Liquid Argon EM calorimeters at ATLAS using $Z \rightarrow ee$ decays. This was my main project during the years I spent on the ATLAS experiment. A brief introduction of this work is presented in Part 3, and a copy of the ATLAS note describing the calibration is in the Appendix.

Part I

Theoretical Motivation and Tools for the Higgs Search

Chapter 1

The Standard Model and ElectroWeak Symmetry Breaking

1.1 Overview of the Standard Model

The Standard Model (SM) is an SU(3) x SU(2) x U(1) gauge theory that aims to provide a complete theory of the strong, weak, and electromagnetic interactions of elementary particles. (In a very non-precise explanation, U(1) is the symmetry group associated with electric charge (or hyper charge), SU(2) with isospin, and SU(3) with the three quark colors.) The elementary particles including quarks, gauge bosons, and leptons are listed in Tables 1.1 through 1.3. These fall into two catagories: bosons and fermions. Bosons are particles with integer spin that obey Bose-Einstein statistics. The bosons listed in Table 1.2 are elementary bosons, which are force carriers. There are also composite bosons which are hadrons with integer spin (such as pions). Fermions are particles with half integer spin which obey Fermi-Dirac statistics and the Pauli exclusion principle. Most matter is made up of fermions.

Fermions and bosons interact via the fundamental forces in the following ways:

- *The Electromagnetic Force.* The photon is the force carrier for electromagnetism. A photon can be exchanged or created/absorbed by any particle with electric charge. Photons are massless and can travel infinite distances, so the range of the EM force is infinite.

- *The Weak Force.* The W and Z bosons are the carriers of the weak force. The weak force can change the flavor of quarks and leptons, and it is the force at work in radioactive decays.

- *The Strong Force.* Gluons are the carriers of the strong force, which is responsible for holding nuclei together. Gluons act on particles with

color charge, which are quarks and themselves. The strength of the strong force increases with distance. Because of this quarks are confined and do not exist alone as single particles.

Charge	Quark (mass)		
$+\frac{2}{3}$	up (1.7-3.3 MeV)	charm (1.27 GeV)	top (172.0 GeV)
$-\frac{1}{3}$	down (4.1-5.8 MeV)	strange (101 MeV)	bottom (4.19 GeV)

Table 1.1: The quarks and their charges and approximate masses. (Masses have a model dependence. See description in [5].)

Gauge Bosons	Mass	Associated Coupling
γ (photon)	0	$\alpha \approx \frac{1}{137}$
Z (weak boson)	91.1876 GeV	$\alpha_W = \frac{\alpha}{(M_W/m_p)^2} \approx 10^{-6}$
$W^{\pm}$ (weak boson)	80.399 GeV	α_W
g (gluon)	0	$\alpha_s \approx 1$

Table 1.2: The force carriers [5].

Massive Lepton	Mass	Associated Lepton Neutrino
e	0.51 MeV	ν_e
μ	105 MeV	ν_μ
τ	1.78 GeV	ν_τ

Table 1.3: The leptons [5].

The Standard Model has been a very successful predictive tool. It has, for example, predicted the existence and mass of the the W and Z bosons, as well as the charm quark, the top quark, and many couplings. But the Standard Model Lagrangian describes massless particles. In order for it to describe the massive Z and W bosons and the masses of fermions, something must be added to introduce a mass term without breaking the gauge invariance of the Lagrangian. A simple addition to the current theory which achieves this is the Higgs Mechanism.

1.2 The Higgs Mechanism

Write down the most simple Lagrangian for a $U(1)$ gauge theory [2]:

$$L = -\frac{1}{4}F_{\mu\nu}F^{\mu\nu} \tag{1.1}$$

Local gauge invariance says that the Lagrangian should be invariant under local gauge transformations. Adding a mass term at this point would violate local gauge invariance. This equation describes the massless photon.

Now add a complex scalar field to the lagrangian that is the minimal coupling to the photons with charge e.

$$L = -\frac{1}{4}F_{\mu\nu}F^{\mu\nu} + |D_\mu\phi|^2 - V(\phi) \tag{1.2}$$

where D is the covariant derivative (so $|D_\mu\phi|^2$ is the kinetic part) and V is the most generic renormalizable potential

$$D_\mu = \partial_\mu - ieA_\mu \tag{1.3}$$

$$V(\phi) = \mu^2|\phi|^2 + \lambda(|\phi|^2))^2. \tag{1.4}$$

Here μ is a mass and λ is the coupling of the 4-boson vertex. In this most generic potential, the μ^2 term can be either positive or negative. If it is positive the scalar potential looks like the curve in Figure 1.1 with the minimum at $\phi = 0$. In order to describe massive particles the potential needs to have a non-zero stable minimum. If μ^2 is negative then the potential has the shape in Figure 1.2 like a sombrero. Here the minimum energy states are not at $\phi = 0$, but rather at

$$\phi = \pm\sqrt{\frac{-\mu^2}{\lambda}} \tag{1.5}$$

To examine quantum fluctuations we do a perturbative expansion around one of the minimums. (It doesn't matter which minimum we choose to expand around, but we do have to pick one, and once we do, the symmetry of the potential will be broken. This is called electro-weak symmetry breaking.)

$$\phi = \pm\sqrt{\frac{-\mu^2}{\lambda}} + \sigma(x) \tag{1.6}$$

then the lagrangian looks like this

$$L = \frac{1}{2}(\partial_\mu\sigma)^2 + \mu^2\sigma^2 - (\sqrt{\frac{-\mu^2}{\lambda}}\lambda\sigma^3 + \frac{1}{4}\lambda\sigma^4) + X \tag{1.7}$$

where the higher order terms are absorbed into X. The third term represents the interaction of the field with itself, and the second term is a mass term, such that

$$m = \sqrt{-2\mu^2} \tag{1.8}$$

So by choosing μ^2 to be negative the Lagrangian now describes particles with mass.

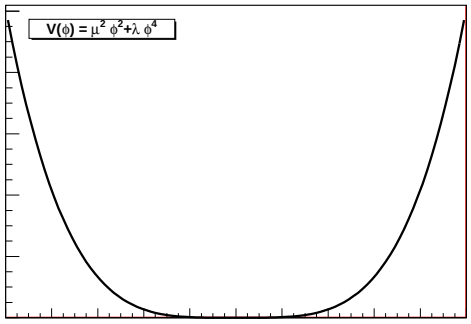

Figure 1.1: The scalar potential with $\mu^2 > 0$

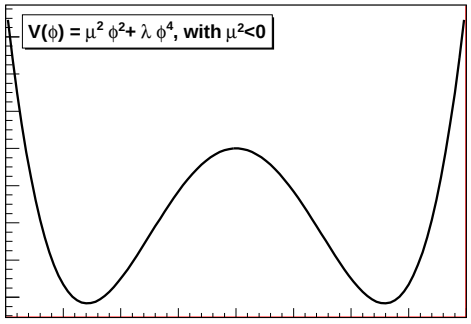

Figure 1.2: The scalar potential with $\mu^2 < 0$

1.3 Theory Arguments for Constraining the Higgs Mass

Bounds can be placed on the possible mass of the Higgs using arguments of "triviality" and vacuum stability [3] [6].

The triviality argument involves placing a bound on the Higgs coupling to scalars (which depends on the Higgs mass) so that it is not zero and not infinity. A coupling of zero would mean that the Higgs does not couple with any other field, making the theory trivial. A coupling of infinity would provide no predictors (perturbation theory would not be possible) and make the theory useless.

First consider the Lagrangian for just a scalar theory, without coupling to gauge bosons or fermions. Write a kinetic term plus a potential part:

$$L = \partial^\mu \phi \partial_\mu \phi^\dagger - \mu^2 \phi\phi^\dagger - \lambda(\phi\phi^\dagger)^2 \tag{1.9}$$

where here λ is the Higgs coupling to scalars which depends on the Higgs mass and the vacuum expectation value, v:

$$\lambda = \frac{M_h^2}{2v^2}. \tag{1.10}$$

Also define Q_o and Q as the energy scale at which we know λ and some other energy scale, respectively. In the Standard Model we take Q_o to be equal to v. Quantum field theory gives us an expression for the change in λ with respect

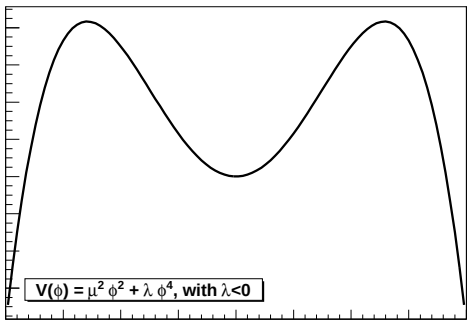

Figure 1.3: The scalar potential with $\lambda < 0$

to Q due to self interactions of the scalar field:

$$\frac{d\lambda}{dt} = \frac{3\lambda^2}{4\pi^2}, \tag{1.11}$$

where $t \equiv log(Q^2/Q_o^2)$. This equation can be solved to get λ as a function of Q:

$$\frac{1}{\lambda(Q)} = \frac{1}{\lambda(Q_o)} - \frac{3}{4\pi^2}\log(\frac{Q^2}{Q_o^2}) \tag{1.12}$$

Make the choice that the "other energy scale", Q, is the highest energy scale to which the Standard Model is valid, Λ. This bound for new physics is often taken to be 10^{16} GeV. (The scale for Grand Unification, in many theories.) Rewrite eq. 1.12 with $Q = \Lambda$ and $Q_o = v$:

$$\frac{1}{\lambda(\Lambda)} = \frac{1}{\lambda(v)} - \frac{3}{4\pi^2}\log(\frac{\Lambda^2}{v}). \tag{1.13}$$

Now make the requirement that λ is not infinite.

$$\frac{1}{\lambda(\Lambda)} > 0. \tag{1.14}$$

Rewrite in terms of eq. 1.13:

$$\frac{1}{\lambda(v)} - \frac{3}{4\pi^2}\log(\frac{\Lambda^2}{v}) > 0. \tag{1.15}$$

Substitute eq. 1.10:

$$\frac{1}{\frac{M_h^2}{2v^2}} > \frac{3}{4\pi^2}\log(\frac{\Lambda^2}{v}) \tag{1.16}$$

which can be written as an upper bound on the Higgs mass:

$$M_h^2 < \frac{8v^2\pi^2}{3\log(\frac{\Lambda^2}{v})} \tag{1.17}$$

Taking Λ as 10^{16} GeV and v taken as 150 GeV, near the most sensitive range at the Tevatron and LHC, gives a limit:

$$M_h < 160GeV. \tag{1.18}$$

If we take Λ as 3 TeV there is a weaker limit:
$M_h < 600GeV$.

This calculation is for the case of a scalar Higgs field. When interactions to fermions and gauge bosons are added, the coupling becomes more complicated, and most, relevantly, depends on heavy fermion masses, namely the top mass.

$$\frac{d\lambda}{dt} = \frac{1}{16\pi^2}[12\lambda^2 + 12\lambda g_t^2 - 12g_t^4 - \frac{3}{2}\lambda(3g^2 + g'^2) + \frac{3}{16}(2g^4 + (g^2 + g'^2)^2)] \quad (1.19)$$

Now if we calculate the bound for $\Lambda = 10^{16}$ GeV and a top mass of 175 GeV, the Higgs mass must be less than 170 GeV.

To bound the Higgs on the lower side, we consider vacuum stability. In the potential in Figure 1.2 V(v) is smaller than V(0). Referring to Eq. 1.4 we can say this is essentially the same as requiring that λ is positive. If this were not true, if you had a potential like the one shown in Figure 1.3, there would be no global minimum (and the local minimum would be at 0, removing the raison d'etre of the Higgs mechanism).

If we assume small values of λ, we can drop the λ and λ^2 terms in Eq. 1.19, leaving only the constant terms. (Since λ is the coefficient in front of the higher order ϕ^4 term we expect it to be small.)

$$\frac{d\lambda}{dt} = \frac{1}{16\pi^2}[-12g_t^4 + \frac{3}{16}(2g^4 + (g^2 + g'^2)^2)] \quad (1.20)$$

When Eq. 1.20 is integrated we get:

$$\lambda(\Lambda) = \lambda(v) + \frac{1}{16\pi^2}[-12g_t^4 + \frac{3}{16}(2g^4 + (g^2 + g'^2)^2)] \log(\frac{\Lambda^2}{v^2}) \quad (1.21)$$

Now substitute in Eq. 1.10 and put in our requirement that $\lambda(\Lambda) > 0$ to get a bound on the Higgs boson mass:

$$M_h^2 > \frac{v^2}{8\pi^2}[-12g_t^4 + \frac{3}{16}(2g^4 + (g^2 + g'^2)^2)] \log(\frac{\Lambda^2}{v^2}). \quad (1.22)$$

We can get an idea of the value of the bound if we take Λ as 10^{16} GeV (this calculation also uses some higher order terms [4])

$$M_h^2(GeV) > 130 + 2(m_t - 170) \quad (1.23)$$

or

$$M_h^2(GeV) > 134 \quad (1.24)$$

with the value of the top mass included [5].

So together Eq. 1.24 and 1.18 say that the Higgs mass should be between 134 and 160 GeV. If we had chosen a lower value for Λ we would get a larger range for the Higgs mass (see Figure 1.4).

1.4 Theory behind event simulation

The Monte Carlo simulations used in this analysis start with the generators Alpgen and Pythia. These programs are described briefly below. The biggest challenge for Monte Carlo simulation is accurately describing jet and multi-jet processes. In general there are two methods to do this: with Parton Shower Models, and with Matrix Element calculations. The Matrix Element procedure is to calculate all the possible Feynman diagrams for a chosen jet multiplicity. This requires choosing the order to which you will calculate the amplitudes and choosing a cut off for calculating soft and collinear poles. It is hard to calculate events with more than a few jets in this way. The parton shower method tries to approximate all terms, rather than calculating a few terms of the expansion exactly. [8]

The pieces of jet events which need to be modeled are:

- the hard process: the interaction of the initial colliding partons (well understood with perturbative calculations)
- the parton shower: production and cascade of particles from accelerated charged particles and accelerated colored particles (fairly well understood–

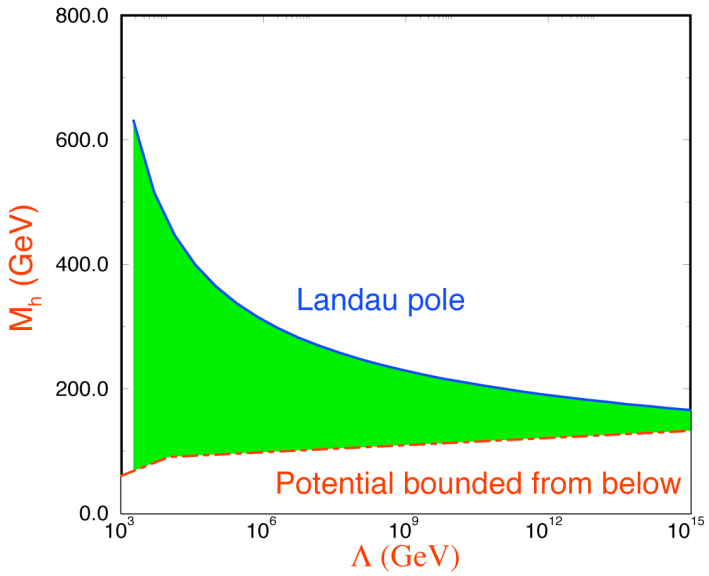

Figure 1.4: Bounds on the Higgs mass as a function of Λ, the scale to which the Standard Model is valid.

perturbative calculations plus approximations)

- hadronization: formation of jets (See 2.3.10) (less well understood, but models are well constrained by data)

- the underlying event (least understood)

PYTHIA

The signals and the diboson background in our analysis are generated using Pythia [10]. Pythia's strong suit is modeling hadronization and showering. (It is less good at modeling multijet events.) Pythia generates events according to Leading Order (LO) calculations of cross section and them uses parton showers to model QCD and radiation. The string model is used to approximate hadronization, based on the ideas of linear confinement.

ALPGEN

The backgrounds $W + jets$, $Z + jets$, and $t\bar{t}$ in this analysis are generated using Alpgen [17]. Alpgen is also a LO generator but it uses exact Matrix Element calculations to generate QCD processes and EM interactions at the parton level. It is quite successful in modeling multijet events, but not as good at modeling showering and hadronization. For this reason many of our background samples are simulated with Alpgen at the parton level and then with Pythia for the hadronization and showering.

When Pythia and Alpgen are used together, care must be taken to avoid double counting events in multijet production. "Matrix element matching" aims to eliminate double counting by matching jets to partons from the hard scattering process; this way each parton corresponds to 1 jet.

The single top background is simulated with CompHEP, which is a next-to-leading over generator. CompHEP calculates cross sections at next-to-leading order using the squared Feynman diagram technique.

In order to better match what is seen in data, corrections are applied to MC jets: referred to as Jet Smearing, Shifting, and Removal (JSSR):

- The jet transverse energy is smeared in order to give MC jets a resolution more similar to data jets. The smearing factor is taken from a Gaussian distribution with a width σ_{smear}, where

$$\sigma_{smear} = \sqrt{\sigma_{data}^2 - \sigma_{MC}^2} \tag{1.25}$$

  with σ_{data} and σ_{MC} denoting the widths of the jet transverse momentum distributions in data and MC.

- When the jet energy scale (JES) corrections derived for data are applied to MC, the jet energies become a little too high. A shift is applied to bring them down to match data.
- Jet ID efficiency is slightly higher in MC than in data so a percentage of MC jets are removed until their ID efficiency matches that of data.

Part II

The $\tau\tau$ jet jet Higgs Search at D$\emptyset$

Chapter 2

Description of the Tevatron and DØ

2.1 Introduction

The Tevatron is located at Fermi National Lab in Batavia, IL. It is the largest of 7 accelerators at the lab, used to take protons and antiprotons to a final center-of-mass energy of $\sqrt{s} = 1.96$ TeV. Protons and antiprotons are collided at two points along the Tevatron, and the collisions are recorded by two multi-purpose detectors: CDF and DØ. The sections below outline how the protons and anti-protons are created, how they are accelerated, and how they are collided. This thesis uses data from the DØ detector, which is described in some detail in section 2.3.

2.2 The Tevatron

First Steps in proton acceleration: Magnetron Chamber, Cockcroft-Walton Generator, Linac. The high-energy collisions at the Tevatron start with a small bottle of hydrogen gas (H_2). This canister holds enough hydrogen gas (H_2) to supply the Tevatron with protons for 6 months. In the first step toward acceleration, the hydrogen is ionized in a magnetron chamber (becoming H^-) and then sent along an electric field to a Cockcroft-Walton generator. A diagram of a magnetron is shown in Figure 2.1. The Cockcroft-Walton generator is a voltage multiplier that takes the H^- ions across higher and higher voltages, finally giving them 750 keV. Then the H^- is bunched in a radio frequency (RF) cavity and sent into the Linac. The Linac is a series of RF cavities which accelerate the H^- ions. The cavities and varying electric field are constructed so that particles are pulled from negative to positive voltage, then shielded as the field oscillates to what would be a decelerating direction, and then exposed again to the next accelerating voltage. After a series of

these cavities and gaps the particles reach an energy of 400 MeV. The timing and spacing of the gaps, cavities, and voltages keep the particles in bunches. Particles at the front of the bunches are accelerated less and those at the end of the bunches are accelerated more. On leaving the Linac the particles are grouped in bunches with a frequency of approximately 200 MHz.

The Booster and Main Injector. The limitation of a linear accelerator is that particles can only be accelerated through it once. For further acceleration the protons are sent through a series of circular accelerators. (The Main Injector cannot accept particles at the energies they come out of the linac because it would be hard to maintain a stable guide field for particles with an energy range from 400 MeV to 150 GeV. The series of circular accelerators increase the particle energy in steps.) The H^- ions from the Linac are passed through a carbon foil to strip their electrons as they are injected in to the first circular accelerator, a 475m synchrotron called the Booster. (Here one might ask why the H^+ was ionized to H^- in the first place if the electrons need to be stripped off again before entering the Booster. The answer is that, unlike positive charged particles, H^- ions approaching the Booster can be bent to the central orbit by the same field that is guiding the protons.) The Booster uses 18 RF cavities to accelerate the particles to 8 GeV after about 20,000 rotations. Magnets keep the particles in line around the Booster. The final step before going into the Tevatron is acceleration in the Main Injector (MI).

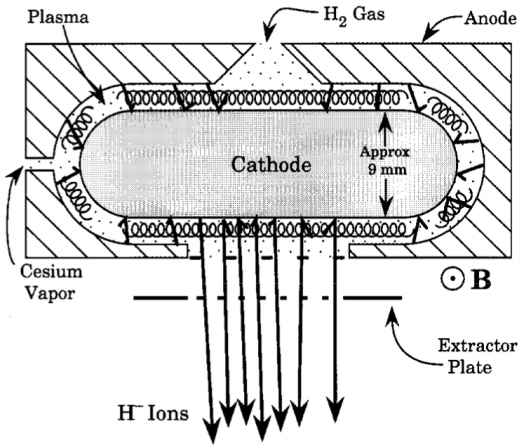

Figure 2.1: Diagram of a magnetron, which is used to produce negative H ions. A plasma is created out of the injected H_2 gas and the positive ions pick up electrons by hitting the cathode. The magnetron replaced an earlier duoplasmatron, which created H^+ ions, in order to increase the beam quality in the Booster [7].

Here protons from the Booster are brought to 150 GeV before being sent to the Tevatron [24].

Antiproton Production: Target, Debuncher, Accumulator. During stacking the MI is also used to accelerate protons to 120 GeV to be used in antiproton production. The 120 GeV protons are shot at a nickel alloy target to create antiprotons. Antiprotons are produced in the p+Ni interaction along with pions, kaons, muons, and other particles. It takes around 100 000 protons to produce a few antiprotons. A pulsed dipole magnet selects (negatively charged) antiprotons with 8 GeV away from the other particles. The antiprotons will be held in the Accumulator but first their momentum and transverse spread is reduced ("cooled") so they can be efficiently transfered and so that enough antiproton bunches can be stacked in the Accumulator for high Luminosity running. The bunches are cooled in the Debuncher, a triangular synchrotron at the Antiproton Source. Only one pulse of antiprotons is in the Debuncher at a time (these are the antiprotons created with the 82 proton bunches sent to the target at a time.) Antiprotons enter the debuncher from the target in pulses that are short in time; RF bunch rotation turns the bunches in phase space so that they are spread in time but have a small momentum width. Adiabatic debunching further reduces the momentum spread by lowering the RF voltage. Stochastic cooling is also used in the Debuncher. As particles go around the Debuncher, pickups measure their position. If they are at the edges of the compact $\overline{p}$ bunch, a message is sent across the Debuncher so that when the particles reach the other side the kicker there will push them back in line. Bunched antiprotons are transfered to the Accumulator (the second triangular synchrotron) and stacked there until enough have been accumulated to be transfered back to the MI (currently about 12 hours). While in the Accumulator the antiproton momentum spread is kept at a desired level with RF bunch rotation and stochastic cooling.

During shot setup antiprotons are extracted from the Accumulator and sent to the Recycler and then the MI. The recycler also uses stochastic cooling and electron cooling to create compact bright bunches of antiprotons. (Previously it also accepted "recycled" antiprotons from the Tevatron but this is no longer done.) These bunches are injected into the MI and then the Tevatron.

Tevatron and Collisions. Once inside the Tevatron protons and antiprotons are accelerated from 150 GeV to 980 GeV, and are collided at a center of mass energy of 1.96 TeV. The proton and antiproton beams are accelerated and held in their circular paths with over 1000 superconducting magnets with field strengths of 4 T and more than 1100 Radio Frequency cavities. Because the beams have opposite charges and go in opposite directions, the same magnets can be used to accelerate and contain both beams. During normal operation

each beam is comprised of 36 bunches of protons and 36 bunches of antiprotons with about 10^{11} particles in each bunch. The Tevatron is currently running at very high luminosities, and recently set a record luminosity of 431x10^{30} cm^{-2} s^{-1} at DØ. The beams are focused and made more dense with quadrupole magnets (called "going to low beta" or "squeezing") before crossing at the CDF and D0 detector sites.

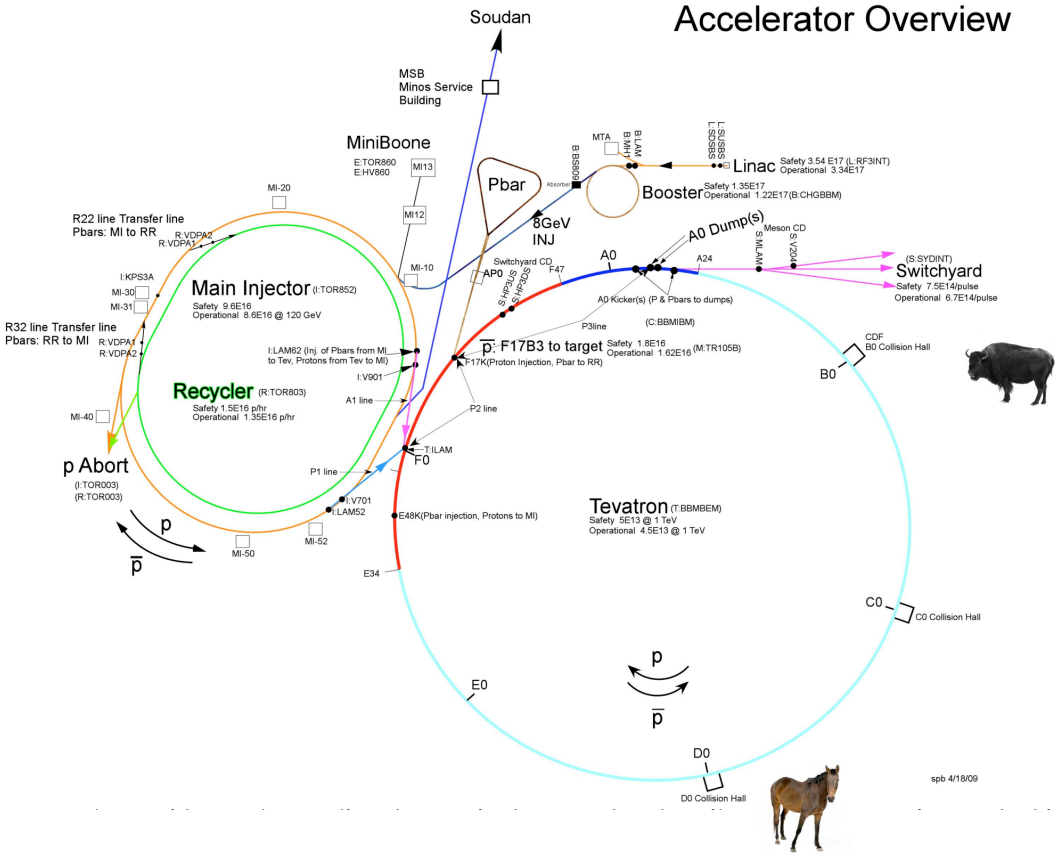

Figure 2.2: The Tevatron complex of accelerators. Animals are shown for above-ground orientation.

2.3 The DØ Detector

A schematic of the DØ detector is shown in Fig. 2.3. The detector encircles the beam pipe and is centered on the beam crossing interaction point. It is 20 m long, 13 m high and wide, and has a solid angular coverage of almost 4π. It is comprised of a concentric detector systems: a tracking system surrounded by a 2 T solenoid, a calorimeter with electromagnetic and hadronic sections, and a muon detector. The DØ detector began taking data in 1992. Between 1996 and 2001 the detector underwent significant upgrades including a new silicon vertex detector (SMT), the addition of the solenoid, the preshower detectors, improved resolution and triggering capability in the muon detector, and very significant trigger upgrades. Data taken after 2001 is called Run 2. In 2006 there were further upgrades: the addition of Layer 0 in the SMT, and further updates to the trigger. This analysis only uses data from the Run 2b period from 2006 to 2009, and so only the upgraded detector is described.

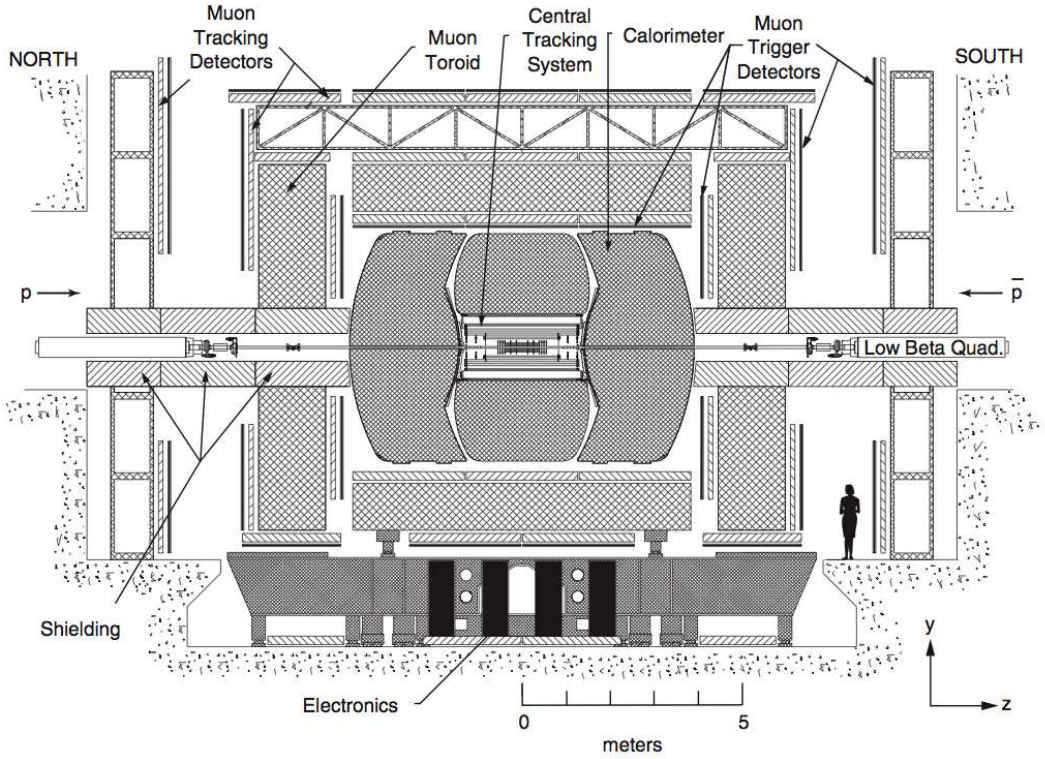

Figure 2.3: A diagram of the *DØ* detector.

2.3.1 Detector Subsystems: The Tracking System

The tracking system consists of the Silicon Microstrip Tracker (SMT) and the Central Fiber Tracker (CFT), surrounded by the solenoid magnet. This is the inner-most piece of the DØ detector, with the SMT surrounding the beam pipe and the CFT surrounding the SMT. They are designed to detect the tracks of particles coming out of collisions (which are curved by the magnetic field) and can locate the primary interaction vertex with a resolution of 35 μm along the beamline. Precision vertex locating is especially important in jet b-tagging. The tracking system makes it possible to tag a b-jet with a resolution in the distance of closest approach to the beam axis of 15 μm in the $r - \phi$ plane for particles at small η. The b-tagging relies on the fact that b quarks form B mesons, and B mesons travel on the order of 1 mm (corresponding to an average lifetime of 10^{-12}s) before decaying. Therefore, vertex resolution smaller than 1 mm is essential for b-tagging.

Silicon Microstrip Tracker (SMT)

The SMT is used for both triggering and vertexing. The design of the SMT is shown in Fig. 2.4. It is advantageous for the silicon strip planes to be positioned perpendicular to the direction of particle tracks so that each particle goes through as many layers of the tracker as possible and maximum information about the particle track is recorded. This is why the tracker is a barrel shape with interspersed disks at low eta and a series of disks along the beam pipe at higher eta. There are 6 barrels sections, each consisting of layers of silicon detector strips. The strips are made of doped silicon semiconduc-

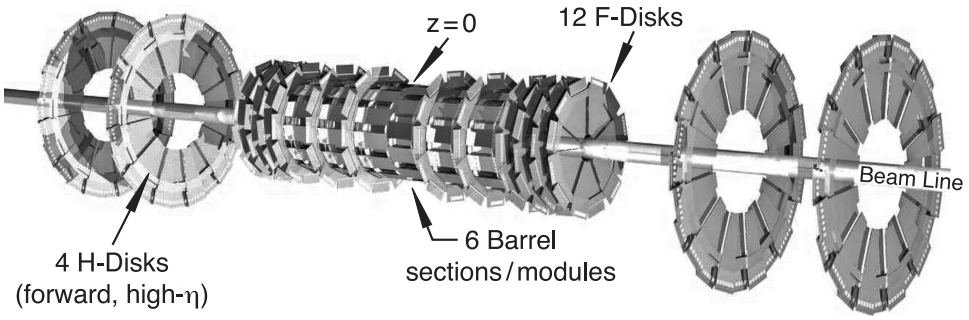

Figure 2.4: A diagram of the SMT. The H-disks are shown in addition to F-disks, but these were removed in Run2b. (Their readout channels were replaced with "Layer 0".)

tor and each one has a voltage difference across it. When a charged particle passes through it creates electron-hole pairs, and the applied voltage makes the charge collect on one or both sides (there are single-sided and double-sided versions) where it can be digitized and read out, to be used to reconstruct the spatial track of the particle. Each barrel has a module of microstrips called an F disk at the high η end. Then at higher eta on each side of the interaction point there are three more F disks. In Run2b (starting in 2006) an extra layer of barrel silicon detectors were added, called Layer 0, to compensate for aging effects and provide improved secondary vertex resolution [12].

Central Fiber Tracker (CFT)

The Central Fiber Tracker (CFT) surrounds the SMT. It is made of scintillating fibers which run parallel (or nearly parallel) to the beam pipe and occupy the radial area from 20 to 52 cm (see Fig. 2.6). The fibers are laid in layers held in 8 concentric cylinders– the 6 outer-most of these are 5.52 m long and extend over the full length of the beam pipe ($|\eta| < 1.7$). In each cylinder pairs of layers of fibers alternate between an orientation exactly parallel to the z-axis, and about $+$ or $-$ 3 degrees off of this axis. The fibers are made of polystyrene (PS) doped with paraterphenyl (paraT) and with a small concentration of 3-hydroxyflavone (3HF). When a charged particle goes through the fibers the PS excites and causes the paraT to fluoresce in 340 nm wavelength light. The 3HF absorbs the 340 nm radiation and re-emits it at 530 nm, which is more easily transmitted through PS. The scintillation light travels down the fiber to a wave guide and out to a visible light photon counter (VLPC). VLPCs are silicon avalanche photodetectors that operate at a temperature of 9 K (they are housed with their main components in the cryostat below the detector). They are able to detect single photons, have a quantum efficiency above 75%, and can operate in a high background environment [12]. VLPCs are also used for readout in the preshower detector.

2.3.2 Detector Subsystems: Preshower

Between the tracking system and the calorimeter is the preshower scintillator detector. It is made up of a central part (CPS) around the outside of the solenoid ($|\eta| < 1.3$), and two forward detectors (FPS) on the inner faces of the calorimeter end caps ($1.5 < |\eta| < 2.5$). These are shown in Fig. 2.11. The preshower detector aids in spatial matching between the tracking system and the calorimeter. It acts as both a calorimeter and tracker itself because it is able to give fast energy and position measurements.

A drawing of the configuration of scintillators in the preshower detector is shown in Fig. 2.7. Triangular strips of polystyrene plastic scintillator are interleaved providing continuous coverage between strips. The center of each

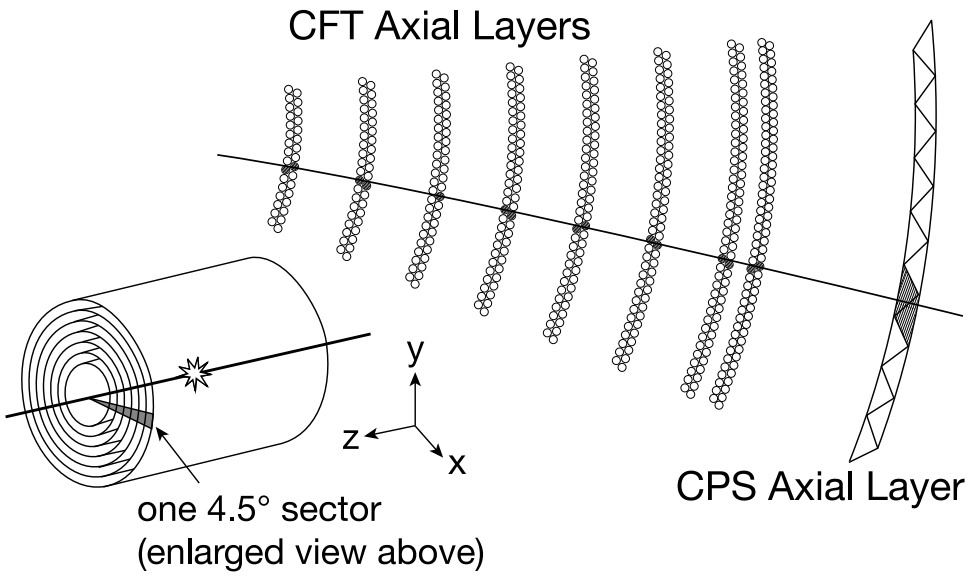

Figure 2.5: The 8 CFT axial doublet layers and CPS axial layer [12].

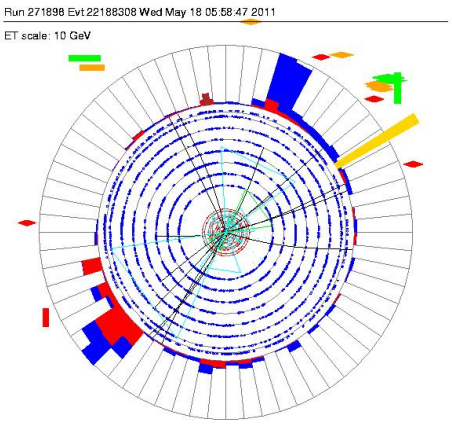

Figure 2.6: Event view of a collision at DØ. Hits in the tracking system are shown as dots on the concentric circles representing the layers of the SMT and CFT. Arcs and lines have been draw where tracking algorithms determined particle tracks.

strip has a wavelength shifting fiber that carries light to the end of the detector. The light is read out using VLPCs (described above). The CPS consists of three layers of 1280 strips each, oriented along the z axis and at stereo angles of about $\pm 24^o$. The FPS has two layers of strips on each side of a lead and steel absorber. The layers inside (closer to the interaction point) the absorber are called the minimum ionizing particle layers (MIP) and the layers outside the absorber are called the shower layers. Charged particles will leave minimum ionizing signals in the MIP layer. Electrons and photons will shower in the absorber and leave wide signals in the shower layers. Hadrons are less likely to shower in the absorber and will leave a second MIP signal in the shower layers.

2.3.3 Detector Subsystems: The Calorimeter

The calorimeter is designed to measure the energy of electrons, photons and jets. It is also used in object identification, and to measure transverse energy balance in events (to indirectly measure neutrinos). A picture of the calorimeter is shown in Figure 2.8. It is made of a central barrel-shaped calorimeter (the "CC") that encircles the tracking and preshower detectors and two end cap calorimeters that extend to η of 4.2. Each of these is contained in its own cryostat and kept at 90 K [12]. The part of the calorimeter closest to the beam is the electromagnetic section, followed by a fine hadronic section, and finally a coarse hadronic section. It is a sampling calorimeter that uses liquid argon (LAr) as the active material. Each part of the calorimeter is constructed with layers of absorber plates and copper pads with a resistive coating separated by LAr filled gaps. Fig. 2.10 shows the absorption/gap structures used in the calorimeter. The calorimeter absorber layers are designed to stop electrons and photons in the EM layers and hadronic particle in the outer layers.

Electrons lose energy in a medium through ionization and bremsstrahlung. Bremsstrahlung ("braking radiation") is the process in which an electron is accelerated by the electric field of a nucleus and so releases a photon ($e \rightarrow e\gamma$). Photons lose energy through pair production ($\gamma \rightarrow e^+e^-$). Radiated photons from bremsstrahlung will pair produce, and electrons from pair production will bremsstrahlung, so that as primary electrons and photons are stopped in the calorimeter there is a shower of particles.

When particles pass through the layers of absorber plates, the absorbed energy ionizes atoms in the LAr. A voltage difference is held between the absorbers and the resistive coating on the copper pads, which causes the electrons from the ionized LAr to drift towards the pads. A charge is read out from the copper pads which is proportional to the energy lost in the absorbers.

The electron drift time is about 450 ns across the LAr gap. The mean

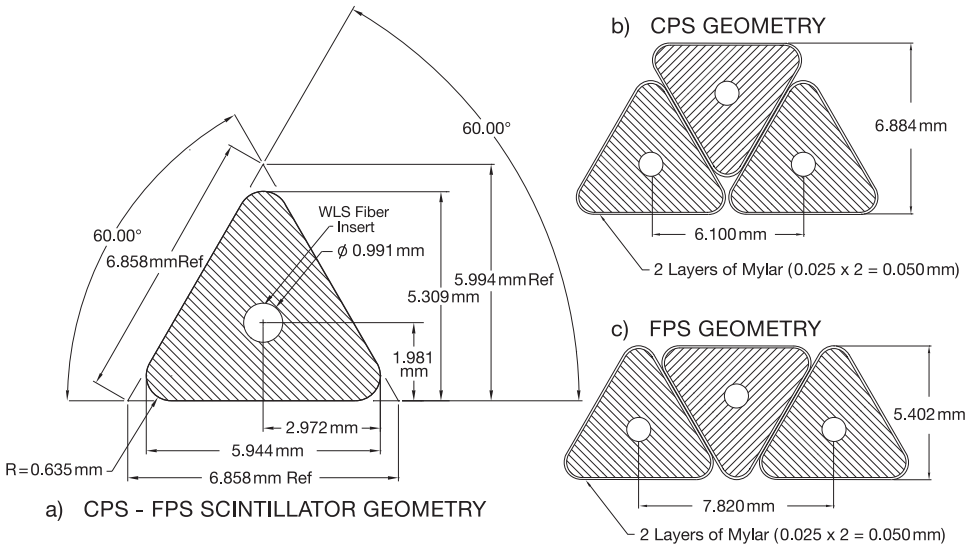

Figure 2.7: Diagram of the scintillator strips used in the preshower detector.

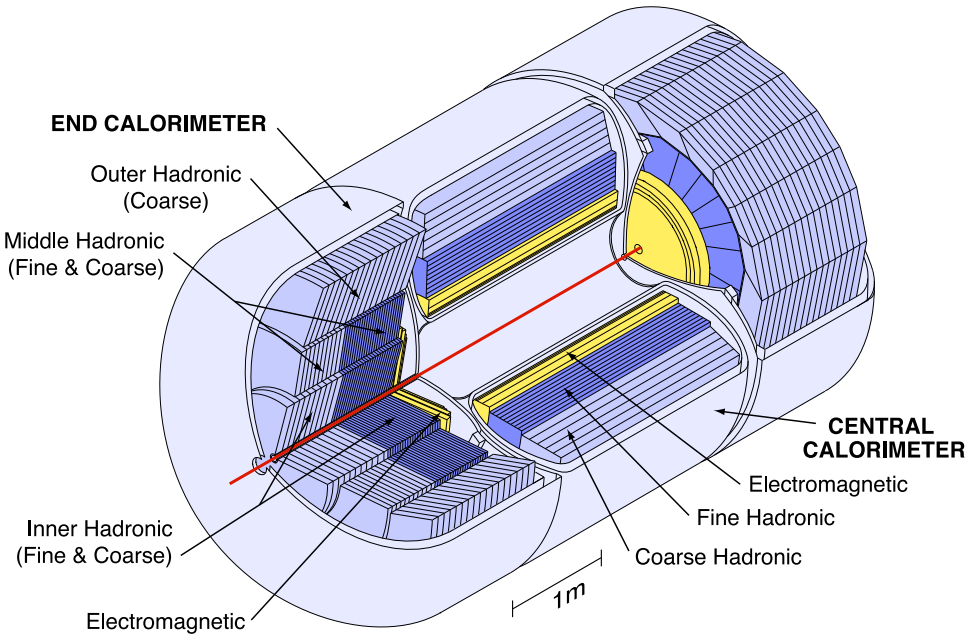

Figure 2.8: The calorimeter.

bunch crossing time is 396 ns, so there can be some pile up of energy in the detector. As part of the the calorimeter readout, the signal from 396 ns before (the previous crossing) is subtracted to remove pile up.

The materials and thicknesses used for absorbers in the different sections of the calorimeter is based on the ways that EM objects (electrons and photons) and hadronic objects (jets made mostly of pions) lose energy in the calorimeter.

Energy loss through ionization is described by the Bethe-Bloch formula (see [2]). Taking ionization and bremsstrahlung together, the energy of an electron passing through a material of thickness x is on average

$$E = E_0 e^{-x/X_0} \tag{2.1}$$

where E_0 is the initial energy of the electron and X_0 is the radiation length, a property of the medium.

As photons pair produce their intensity goes down by a factor of e after a

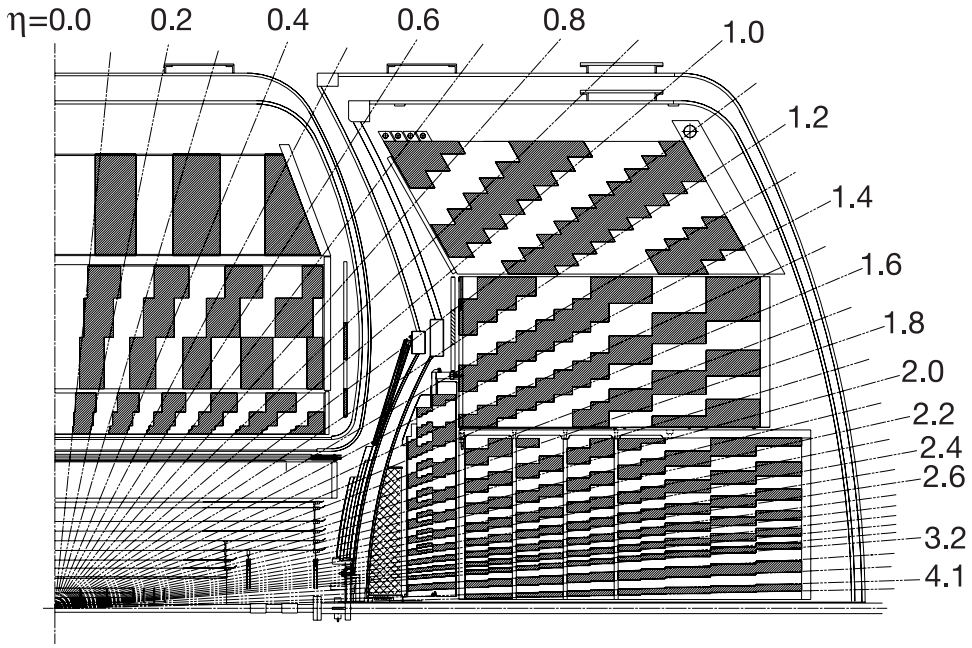

Figure 2.9: Cross section of a quarter of the tracking system and the calorimeter. The calorimeter part has shaded cells representing the calo towers. The centers of the cells lay along lines projecting from the interaction points. The area between $1.1 < \eta < 1.4$ is the Inner Cryostat Region.

distance of $\frac{9}{7}X_0$ in a medium.

The absorbers in the EM section are made of thin pieces of uranium (3 mm thick in the CC and 4 mm thick in the EC). The depths of the EM layers of the calorimeter are designed to optimally sample EM showers, which on average will peak in the middle of the layers (though the shower maximum position is logarithmically energy dependent). The thicknesses of the four layers are 1.4 X_0, 2.0 X_0, 6.8 X_0, and 9.8 X_0 [2]. The cells are $\Delta\eta = 0.1$ by $\Delta\phi \approx 0.1$ (or $\Delta\eta = 0.05$ by $\Delta\phi = 0.05$ in EM layer 3); this contains most EM showers [12].

Hadrons lose the majority of their energy in material through strong interactions. Pions and protons (or other hadrons) interact with the nuclei in the material via the strong force and form new particles with lower energies. These resulting particles repeat the process, creating a shower of lower and lower energy particles. The particles lose energy to ionization, but this does not change the fractional energy until the particles get down to low energies from strong interactions. Then ionization takes over as the stopping force. The mean free path of a particle before it has an inelastic collision with a nucleus is called the absorption length, λ_A. The absorption length is larger than the radiation length, so it takes more material to contain a hadronic shower than an EM shower (more material to stop a hadron than an EM particle), and for this reason the hadronic layers of the calorimeter are thicker than the EM layers.

In the fine hadronic section of the calorimeter niobium-uranium is used as the absorber in thicknesses of 6 mm. The coarse hadronic section uses copper

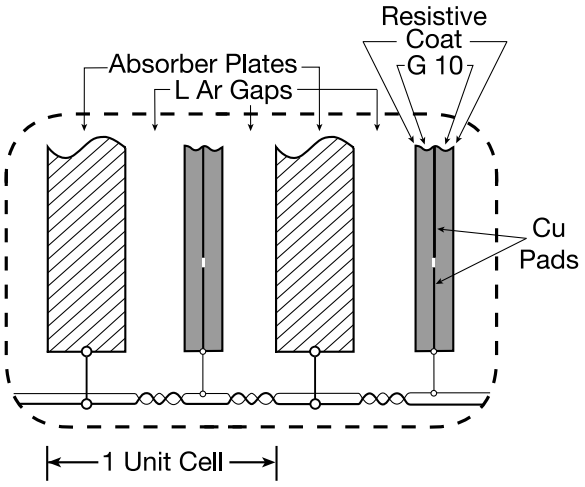

Figure 2.10: The absorption/gap structures used in the calorimeter.

in the CC and steel in the EC, both 46.5 mm thick. The unit cells (see Figure 2.10) vary in thickness between about 1 absorption length in the fine hadronic section (there are four unit cells in the CC and 4 in each EC) and about 4 λ_A in the coarse section (there is one unit cell in the coarse hadronic portion of the CC and one in each EC). The cells are also $\Delta\eta = 0.1$ by $\Delta\phi \approx 0.1$ in size, but as the hadronic layers are further out from the beam than the EM layers this is a larger area and adequate to contain the hadronic showers.

2.3.4 Detector Subsystems: The InterCryostat Detector

Between the central calorimeter (CC) and end cap calorimeters (EC) there are regions of lower resolution due to dead material from cables, supports, and the cryostat walls. See rapidity region $0.8< |\eta| <1.4$ in Figure 2.9. To get back some of the lost energy response in this region scintillating sampling material is attached to the exterior surfaces of the cryostats. This is called the InterCryostat Detector (ICD). The position of the ICD is shown in Figure 2.11. The scintillating part of the detector is made of Bicron BC-400 scintillating tiles, which are housed in aluminum boxes to shield against outside light. Signals are carried through optical fibers to photomultiplier tubes. There are also calorimeter cells called massless gaps inside the cryostats at the ends of CCFH modules and the front face of ECMH modules, which give information on the unsampled material in the region.

2.3.5 Detector Subsystems: The Muon Detector

Muons only deposit a small amount of energy in the calorimeter. Although electrons lose energy through emitted photons as they are decelerated by the electric field of nucleons in the calorimeter, it takes much more to slow a muon, with a mass about 200 times larger. (Energy loss from Bremsstrahlung $\propto 1/m^4$.)

The muon detector is placed outside of the calorimeter so that other particles are contained before we try to detect them. A diagram of the pieces of the muon detector is shown in Fig. 2.12. It consists of scintillator counters, 3 solid iron toroid magnets, and drift tubes.

Drift tubes are arranged in sheets on all sides of the detector. Proportional Drift Tubes (PDTs) are a part of the original Run1 detector and cover to η of 1.0. For Run 2 Mini Drift Tubes (MDTs) were added out to $\eta \approx 2.0$. The PDTs are filled with Argon gas (84% Argon, 8% CF_4, and 8%CH_4), with a wire running down the center. MDTs are filled with 90% CF_4, and 10%CH_4.

When muons pass through the tubes they ionize the gas. The wires are kept at high voltage so the ionized charge collects on them and is read out as a signal, where the charge is proportional to the energy lost by the muon. The MDTs have an improved drift time (time for ionized electrons drifting to the wire) to the PDTs, providing good timing to the muon measurements. The good drift tube time is converted to a precision position measurement.

There is a central toroidal magnet (1.8 T) and two forward toroidal magnets (1.9 T) as a part of the muon detector. The magnets curve muons and allow for additional p_T and charge information (beyond tracker information) to be measured by the muon detector. In both the forward and central regions there are three layers of drift tubes: the first layer (the A layer) is inside the toroidal magnet and the other two are on the outside (the B and C layers). Scintillation counters are mounted on the "layer-A" PDTs between the calorimeter and the magnets. There are also scintillation counters on the outside of layers B and C. These all provide fast information for triggering, muon ID, and rejecting out-of-time background events (like cosmic rays). There is a gap in

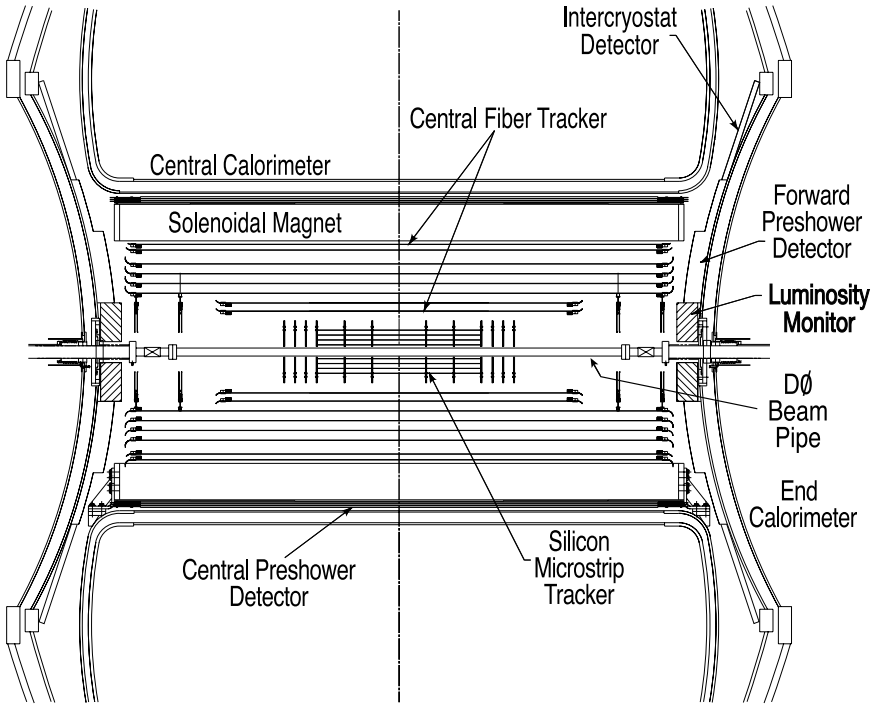

Figure 2.11: A cross section of the DØ detector. Note the position of the Intercryostat Detector.

the scintillators and PDTs on the bottom of the detector to provide room for support structures. This reduces muon acceptance by approximately 12%.

In identifying a muon object coincidence is required between the scintillator and drift tube hits, both inside and outside the toroid magnet.

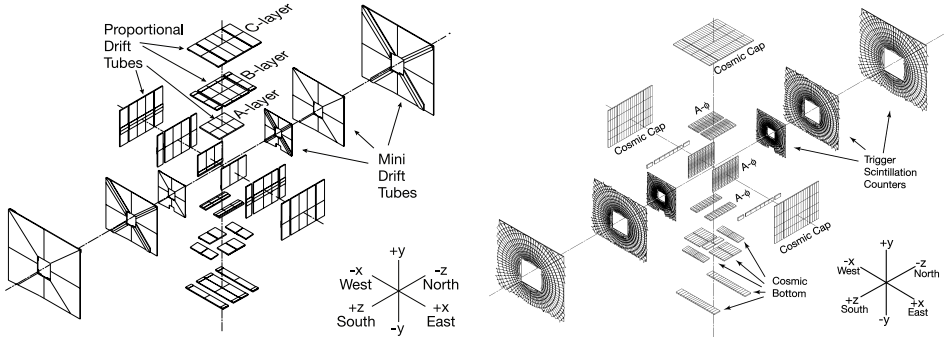

Figure 2.12: An exploded view of the muon detectors. The left figure shows the drift tubes and the right figure shows the scintillators.

2.3.6 Luminosity

Luminosity is calculated with information from the Luminosity Monitors (LM). The Luminosity Monitors are plastic scintillation counters located at the end of the tracker at $z = +140cm$ and $z = -140cm$ (see Figure 2.11) that detect inelastic $p\overline{p}$ collisions. To distinguish inelastic collisions from beam halo the LMs calculate the z vertex using the difference in time of flight for particles hitting the + 140cm LM (t_+)and the -140cm LM (t_-):

$$z_{vtx} = (c/2)(t_- - t_+) \tag{2.2}$$

Real $p\overline{p}$ collisions should have z_{vrt} <100 cm. Above this the beam halo begins to show up.

The luminosity is then calculated using the average number of true inelastic events per beam crossing as measured by the LM, $\overline{N}_{LM}$,

$$L = f\overline{N}_{LM}/\sigma_{LM} \tag{2.3}$$

where f is the beam crossing frequency and σ_{LM} is the effective cross-section for the LM that takes into account its acceptance and efficiency [12]. Also see [23].

2.3.7 Triggering

The collision rate at the Tevatron is 1.7 MHz. It would be impossible (financially and technologically) to store the data from every collision, so a series of triggers cuts out uninteresting events. The trigger system has 3 levels:

- L1: A hardware trigger with an accept rate of about 2 kHz. L1 uses a pattern of 128 trigger terms incorporating information from the calorimeter, the CTT, muon system, and the FPD. Terms are calculated in 132 ns, creating a deadtimeless L1 decision.

- L2: Hardware and software together, with some object ID. The accept rate is about 1 kHz. Simplified physics objects are reconstructed in parallel from each subsystem and then event topologies and correlations between subsystems are evaluated. See Figure 2.13 for a diagram of the data flow through L1 and L2.

- L3: A farm of microprocessors which uses algorithms to reduce the rate to about 50 Hz. This software trigger performs limited event reconstruction using reference tables with algorithm parameters (the jet algorithm cone size or the EM fraction, for example).

Events passing the L3 trigger are recorded for offline reconstruction.

The $e\tau jj$ analysis uses data collected with the *single em trigger OR*. This is a logical OR of many EM trigger terms that effectively requires that all events have at least one loosely defined EM object. In theory, taking all data events rather than just those passing the em trigger would increase background.

2.3.8 Object Identification: Electron Selection

Electrons are identified using information from the tracking system and the electromagnetic section of the calorimeter. Reconstruction begins with clusters of cells in the calorimeter that contain energy deposits above a certain threshold. A cone algorithm is used to build the initial cluster of cells. The initial clusters must have an isolation within a maximum value (default = 0.2) to distinguish them from electromagnetic jet fragments. The isolation is the ratio of the total energy (the sum of EM and hadronic calorimeter energy) within a circle of radius $R = 0.4$ around the highest p_T calorimeter tower in a cluster to the energy in a circle of radius 0.2. The clusters are then matched to a track and a preshower cluster. Unmatched clusters are attributed to photons and removed. Appropriately weighted energy from the preshower is added to that of the calorimeter cluster, and the position of the calorimeter

cluster+preshower cluster is recalculated. The track information is used, along with the energy, to determine the particle momentum.

Further criteria are used to define a "good" electron are discussed in Section 3.4.1. Some of the variables used are described below.

- The E_T of the electron is calculated from the EM cluster energy and position and the primary vertex location.
- The p_T is calculated from the curvature of the track in the tracker and the energy in the calorimeter.
- EMfraction: The fraction of energy in the EM layers of the calorimeter compared to EM layers + hadronic layers. The calorimeter is designed so that electrons should deposit most of their energy before reaching the hadronic layers, so a cut near 90% helps ensure that the particle is an electron rather than a hadron.
- Track match: A spatial fit is performed to match EM clusters to tracks from the CFT and SMT detectors. The χ^2 probability of the match is defined by

$$\chi^2_{spatial} = (\frac{\Delta\phi}{\sigma\phi})^2 + (\frac{\Delta z}{\sigma z})^2 + (\frac{E_T/pT - 1}{\sigma_{(E_T/p_T)}}) \tag{2.4}$$

  where $\Delta\phi$ and Δz are the difference in position between the track and the EM cluster, and $\sigma\phi$ and σz are the RMS's of these values. The third term constrains the ratio of calorimeter transverse energy to the p_T calculated from the track; this term is only included for electrons in the central calorimeter.

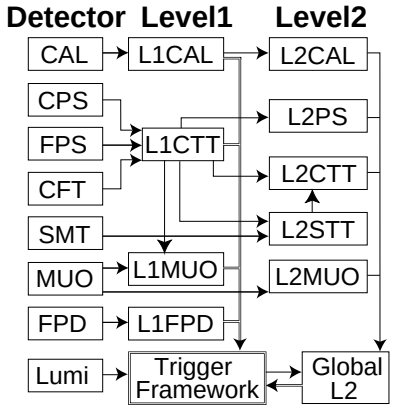

Figure 2.13: A diagram of the data flow in the L1 and L2 trigger systems.

- The H-matrices, HMx7 and HMx8: The H-matrix is the χ^2 of the covariance matrix built with the following inputs: the shower energy fraction in each of the first 4 EM layers of the calorimeter, the cluster size in the 3rd layer of the calorimeter, the total shower energy, the primary vertex position, and (in the MHx8 case) the transverse width of the shower.

- LogLikelihood(8): The likelihood uses the probability that an event is an electron based on 8 variables : EMFraction, HMx7 and HMx8, E_T $/p_T$, Total track p_T in a cone of radius 0.4, Number of tracks in a cone with R= 0.05, The spatial track match χ^2 probability, and the Distance of Closest Approach (DCA), defined as the shortest distance from the selected track to the line parallel to the z-axis which passes through the primary vertex position.

2.3.9 Object Identification: Tau Selection

Tau leptons decay to electrons or muons 35% of the time and to hadrons 65% of the time. (When they decay to electrons or muons they are not distinguished from prompt electrons and muons; signal electrons sought in this analysis may have come from taus, but may also have come from W's.) When τs decay to hadrons, detecting them is complicated because they look like jets. To detect a hadronic tau DØ uses information from the hadronic calorimeter, the electromagnetic calorimeter, and the tracker. Specifically we use the following quantities:

- A hadronic calorimeter cluster: Energy in the hadronic calorimeter found with the Simple Cone Algorithm with ΔR < 0.5.

- An EM sub-cluster: Energy in the EM calorimeter found using the Nearest Neighbor Algorithm with a seed in the 3rd EM layer, which has finer segmentation. Energy in the EM subcluster is required to be above 800 MeV.

- Tracks: Tracks within a cone of radius 0.3 around the hadronic calorimeter cluster, each with $p_T > 1.5$ GeV, and with the track invariant mass consistent with the tau mass.

Hadronic taus can be put into three groups based on typical decay mode signatures in the detector.

- **Type 1** : Calorimeter cluster, with one associated track and no EM sub-cluster. This is designed to identify the decay: ($\tau^{\pm} \rightarrow \pi^{\pm}\nu$). ($\tau$s decay this way 11.6 % of the time.)

- **Type 2** : Calorimeter cluster, with one associated track and at least one EM sub-cluster. This should identify the decay: ($\tau^{\pm} \rightarrow \rho^{\pm}\nu \rightarrow \pi^{\pm}\pi^{0}\nu$). (BR 36.5%)

- **Type 3** : Calorimeter cluster, with more than one associated track and with or without EM sub-cluster. Candidates with two opposite sign tracks, for which the tau charge is ambiguous, are rejected. This is should identify the decay: ($\tau^{\pm} \rightarrow a_1^{\pm}\nu \rightarrow \pi^{\pm}\pi^{\pm}\pi^{\mp}(\pi^{0}s)\nu$). (BR 15.2%)

DØ uses a neural net to train taus against backgrounds. Figure 2.14 shows the output of the neural net, which is trained separately for each tau type. The neural net takes input such as calorimeter isolation, track isolation, cluster width, energy per calorimter layer.

Besides this general tau neural net for the three types, there is an additional neural net specifically for distinguishing Type 2 taus and electrons (NNel) since their topologies are similar.

2.3.10 Object Identification: Jet Selection

Because the strong force increases with distance, quarks and gluons, which are bound together by the strong force, are "confined" and can never appear separately. If quark- antiquark pairs acquire enough kinetic energy to be ripped from each other (as they do in collisions at the Tevatron), new quark-antiquark pairs are created from the vacuum so that quarks always exist in bound states. Consequently, quarks and gluons do not appear in our detectors as single particles, but instead as jets of many particles. These hadrons additionally shower in the calorimeter and create even more particles. This makes it hard to measure the energy of the initial quarks and gluons, since one has to add up all of the resulting particles. DØ uses a method called the RunII Cone Algorithm to find jets and calculate their energy. The algorithm follows these steps:

- Clusters of calorimeter cells with energy over a certain threshold are selected as seeds.

- All clusters within a cone radius of $\Delta R < 0.5$ of the seed are grouped into a "proto-jet".

- If neighboring proto-jets are closer together than a minimum distance they are merged into one jet, otherwise they are kept as separate jets. The resulting set of jets are kept so long as they have $E_T > 6$ GeV.

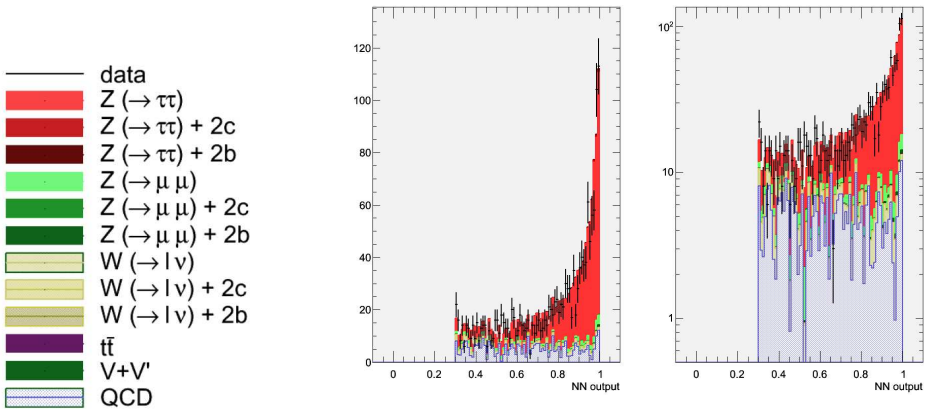

Type 1

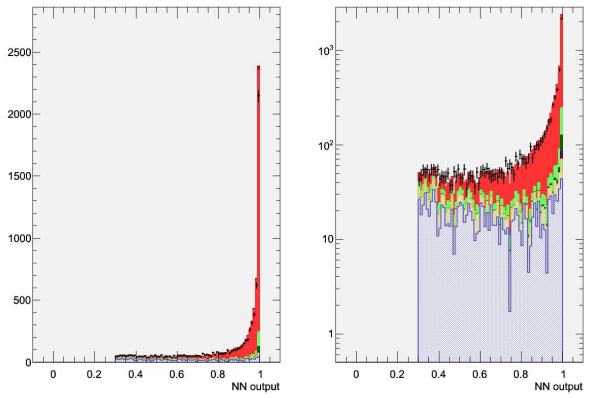

Type 2

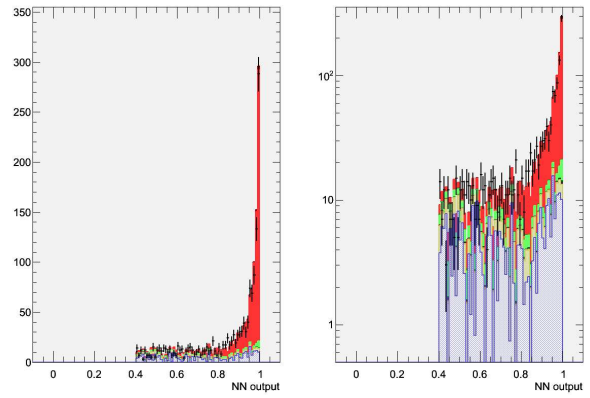

Type 3

Figure 2.14: The TauNN output. Real τs are pushed to the signal side. This analysis uses τs with TauNN above 0.9, 0.9, and 0.95 for the three types. [19]

- To help remove sensitivity to soft radiation ("infrared safety") the midpoint between two jets at this stage is used as a seed for a proto-jet.

- To avoid double counting, jets are not allowed to share more than 50% of another jet's initial cluster energy.

Using this algorithm the jets do not yet have energies matching the particles they correspond to. A number of corrections are applied− called the Jet Energy Scale (JES) corrections− on an event by event basis to make the energy more correct:

$$E_{jet} = \frac{E_{\rm jet}^{\rm measured} - O}{F_\eta \cdot R \cdot S} \tag{2.5}$$

where $E_{\rm jet}^{\rm measured}$ is the energy of the jet from the cone algorithm, and $E_{\rm jet}$ is the energy used for physics analysis. The other terms are described below:

- O is the offset energy. This is energy picked up in the jet not due to the initial collision, but to secondary $p\overline{p}$ interactions, pile up from previous collisions, and radioactive decays in the uranium in the calorimeter.

- F_η is the η-dependent correction for variations in calorimeter response. It is measured by comparing photon and jet p_Ts in events with back-to-back in ϕ photon-jet pairs.

- R is an absolute energy response calibration. It is derived from photon-jet balancing after the η-dependent variations have been accounted for.

- S is the shower shape correction. Based on simulations, S tries to account for the portion of energy from particles within the jet core that shower outside the cone, and vice versa.

Note that separate JES corrections are applied to data and MC jets.

In addition to the basic jet ID, the following jet quality criteria are used at the analysis level.

- Coarse Hadronic Fraction of the energy: the fraction of the jet p_T in the coarse hadronic calorimeter layers compared to the total p_T. Cutting out events with a high CHF helps remove jets reconstructed from noise.

- EM Fraction of the energy: the fraction of the jet p_T in the EM layers of the calorimeter compared to the total. This helps reject electromagnetic particles which may have left some energy in the hadronic layers.

- L1Conf: Ratio of energies from level 1 jet trigger readout and the jet cone algorithm.
- To help reduce noise from electronics or pile up, a jet vertex confirmation is required to ensure that jets originated from the primary vertex in a collision. Jets are required to match to at least two tracks with a p_T above 0.5 GeV, a DCA below 0.5 mm in the transverse plane, a DCA above 1.0 mm along the z axis, and a distance from the primary vertex of less than 2 cm. Studies in the $\mu\tau jj$ analysis have shown that loosening this requirement provides a large increase in good jets without a large increase background. Further studies are being done to see how non-vertex confirmed jets can be included.

2.3.11 Object Identification: Muon Selection

Muons are reconstructed using information from the central tracker and the muon detector. All layers of the muon detector are required to register a hit for an object to be identified as a muon. Muons with scintillator hit times of more than 10 ns different from that expected from collisions are rejected as cosmic rays. The central tracker has higher spatial resolution than the muon detector and so it is used to improve the position and momentum measurements of muons. There is also a requirement that there be a track match between the central tracker and the muon system.

2.3.12 Object Identification: MET Algorithm

In order to "measure" the energy carried by neutrinos (whose interaction cross section with matter is too low for us to detect) we use the fact that the transverse energy of an event should have a vector sum equal to zero. Any "missing" transverse energy ($\not\!\!E_T$) can be attributed to neutrinos. At DØ the $\not\!\!E_T$ is calculated by adding the transverse energy of all EM and fine hadronic calorimeter cells. The coarse hadronic cells are not included because of their higher noise levels. In order to include the energy corrections for physics objects (especially jets), the cells used in identified physics objects in an event are removed from the sum and replaced with the object energy:

$$\not\!\!E_{x,y} = -(\sum_{\text{all cells}} E_{x,y} - \sum_{\text{phys cells}} E_{x,y}^{\text{phys cells}} + \sum_{\text{phys obj}} E_{x,y}^{\text{phys obj}}) \tag{2.6}$$

$$\not\!\!E_T = \not\!\!E_x \oplus \not\!\!E_y \tag{2.7}$$

Chapter 3

Search for the Higgs Boson in the Final State with Two τ's and Two Jets

3.1 Motivation

This chapter will describe the details of the Standard Model Higgs search in the final state with two τ's and two jets. The primary mass region in which Higgs searches are conducted at the Tevatron is between 100 and 200 GeV. Figure 3.1 shows the production mechanisms for a Higgs in this mass region at the Tevatron. Relative Higgs decay rates are illustrated in Fig. 3.2. A low mass Higgs (m_H below 135 GeV) should primarily decay into a b and a $\overline{b}$ quark; the next most probable decay is to two τ's. A high mass Higgs (above 135 GeV) should decay most often to two W's. DØ has analyses dedicated to looking for a high mass Higgs decaying to WW (via gluon fusion, vector boson fusion, and associated production in the final states ee, $\mu\mu$, $e\mu$, $l\nu$ jet jet, $\mu\tau_{hadronicdecay}$+ 0 or 1 jet) and separately for the low mass Higgs to $b\bar{b}$ (via associated production in the final states with $b\bar{b}\nu\nu$, $b\bar{b}ll$, $b\bar{b}l\nu$). These represent the highest sensitivity searches, but there are further searches such as H to ZZ at the high mass, H to two photons at the low mass, and this $\tau\tau$ jet jet search that add additional sensitivity and coverage in mass. The search in the final state 2 τ + 2 jet covers the full 100 to 200 GeV Higgs mass range because it is sensitive to both $H \to \tau\tau$ and $H \to WW \to \tau\tau$. This is beneficial to the coordinated DØ Higgs search especially in the middle mass region around 135 GeV because the dedicated low and high mass Higgs searches lose sensitivity there.

The production processes to which the 2 τ + 2 jet final state is sensitive are:

$$q\overline{q} \to H(\to b\bar{b})Z(\to \tau^+\tau^-) \quad \text{(denoted HZ)} \tag{3.1}$$

$$q\bar{q} \rightarrow Z(\rightarrow q\bar{q})H \quad (\mathrm{ZH}_{\tau\tau} \text{ or } \mathrm{ZH}_{\mathrm{WW}}) \tag{3.2}$$

$$q\bar{q} \rightarrow W(\rightarrow q\bar{q}')H \quad (\mathrm{WH}_{\tau\tau} \text{ or } \mathrm{WH}_{\mathrm{WW}}) \tag{3.3}$$

$$gg \rightarrow H + (\geq)2 \text{ jets} \quad (\text{gluon gluon fusion, } \mathrm{GGF}_{\tau\tau} \text{ or } \mathrm{GGF}_{\mathrm{WW}}) \tag{3.4}$$

$$q\overline{q'} \rightarrow q\overline{q'}H \quad (\text{vector boson fusion, } \mathrm{VBF}_{\tau\tau} \text{ or } \mathrm{VBF}_{\mathrm{WW}}) \tag{3.5}$$

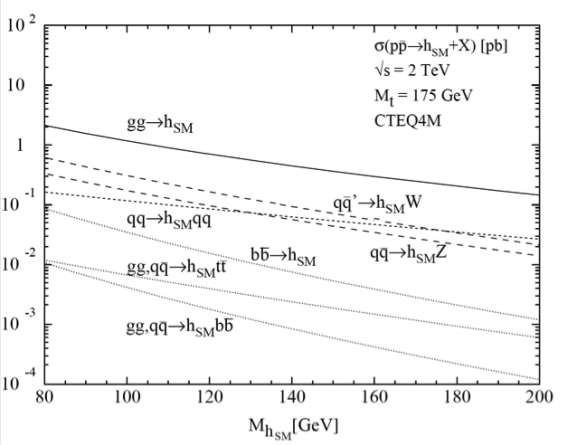

Figure 3.1: Higgs production at the Tevatron.

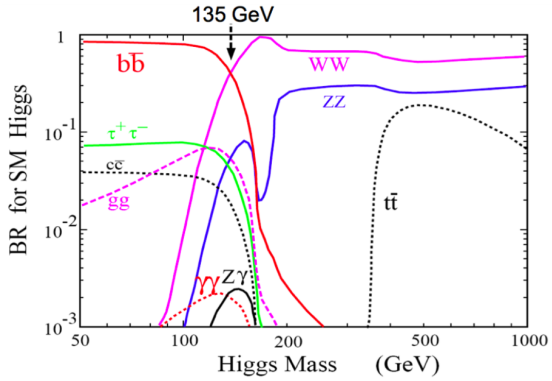

Figure 3.2: Higgs decay channels: branching ratio versus Higgs mass.

The Feynman diagrams for these processes are shown in Figure 3.3. This thesis describes the search for 2 τ + 2 jet events where one τ has decayed to an electron and one τ has decayed to jets. This is complementary to the existing DØ analysis requiring one τ decay a μ.

The major backgrounds to the signals are $Z + jets$ ($Z \rightarrow ee$ where one e fakes a τ or $Z \rightarrow \tau\tau$ where one τ decays to an e), multijet (where jet fragments fake a τ and an e, $W + jets$ (where W decays to e or τ and jet fragments fake a τ or e), $t\bar{t}$ (to two leptons and two jets), and diboson events (which decay similarly to associated H production). The legend in Figure 3.4 shows the colors used for backgrounds in the stack histogram plots throughout this thesis.

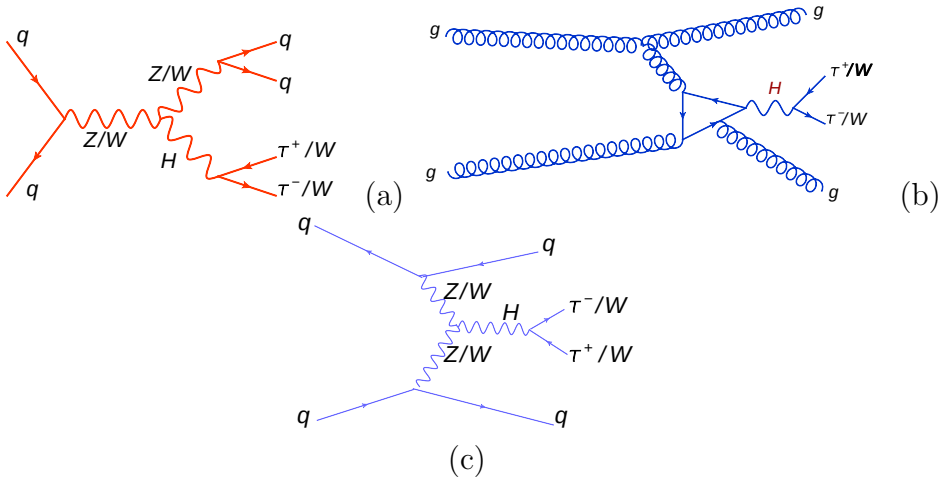

Figure 3.3: Leading order Feynman diagrams for Higgs production processes: (a) VH associated production; (b) gluon gluon fusion; (c) vector boson fusion. The analysis includes cases where the Higgs decays to two τs and to two W's.

3.2 Data

As described in section 2.3, the DØ detector began the "Run 2" period of data taking after a hardware upgrade which finished in 2002. There was additional maintenance work and upgrade (LØ, trigger) done during a shut-down period in 2006. This analysis uses Run 2 data taken between 2006 and 2009.

Data is checked for quality in each DØ subdetector, and all runs marked as bad by the CFT, SMT, CAL or MUON quality groups have been removed

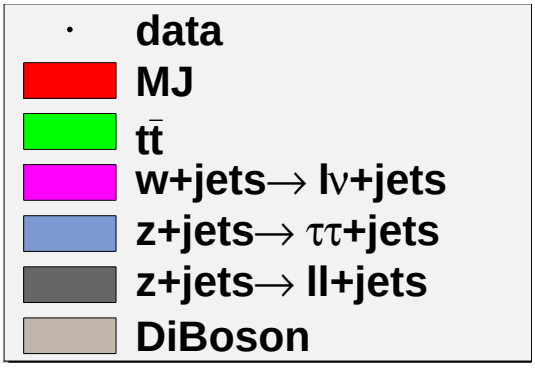

Figure 3.4: Legend for all histograms.

for this analysis.

Events were triggered with the singleEM trigger OR, which includes all the primary electron triggers, utilizing the calorimeter and the tracking system. We apply the standard DØ trigger efficiencies (from the *vjets cafe* package), which were derived using a tag-and-probe method with a $Z \rightarrow e^+e^-$ sample. The tag-and-probe method selects two electrons with an invariant mass consistent with the Z; one electron is required to pass very stringent selection cuts, while the other satisfies the cuts for which one tests the efficiency. In this way one can test a selection on a sample of quite pure electrons. These efficiencies are weighted by the luminosity and applied to the monte carlo simulated events. The luminosity is calculated using a trigger which remained unprescaled throughout the dataset used. The total luminosity analyzed is 4.3 fb^{-1}.

3.3 Monte Carlo Simulations

Monte Carlo simulations are made for the processes which should be present in our data sample according to the Standard Model. This includes both the signals we search for and also the background processes which pass our selection cuts. Signal processes are generated with PYTHIA (version 6.3) [10] [11] for each of the nine signal processes at twenty Higgs mass points each (between 105 and 200 GeV in intervals of 5 GeV). The generated signals are normalized to the appropriate cross sections using the CTEQ61 [16] parton distribution functions at next-to-next-to-leading order, except in the case of VBF, where the calculation is next-to-leading order. The Higgs branching fractions are calculated with the HDECAY program [14]. Tables 3.1 through

3.4 show the signal monte carlo samples generated and list the cross sections for each.

The background processes $t\bar{t}$ and W/Z+jets were generated at the parton level with ALPGEN [17] and then put through simulated showering and hadronization with PYTHIA. These processes are scaled by so-called K factors to correct for differences between leading order and next-to-leading order calculated cross sections and the kinematic differences between LO and NLO or data. The diboson processes are generated with PYTHIA 6.319 and normalized using NLO MCFM [18].

All the monte carlo signals and backgrounds are put through the simulated DØ detector created with GEANT 3 [15].

The MC simulation does not exactly match the data, and so a number of correction factors are applied to MC to bring the two into agreement. The MC is already normalized to the appropriate luminosity but this does not take into account specifics like underlying events or pile-up energy that is specific to a luminosity block. This is corrected for using a using a zero bias sample with a luminosity profile that is matched to the data. Then a correction is made to account for the change in beam position, which affects the longitudinal position of the primary vertices of events. In the simulation the positions of the primary vertices form a gaussian distribution around $z = 0$, but in reality this distribution is not perfectly Gaussian and must be corrected for (see Figure 3.5). The W and Z bosons have known p_T distribution shapes measured by CDF and DØ, but these distributions are not perfectly described by our monte carlo. Factors are applied to the MC to correct the shapes. In the case of the Z, the factors are dependent on the number of jets in each event.

Sample	σ_{NLO} (pb)	MC req-id	N_{events}
$HZ \to b\bar{b}\tau^+\tau^-$, m_H=105 GeV	3.81×10^{-3}	97877	100K
$HZ \to b\bar{b}\tau^+\tau^-$, m_H=110 GeV	3.17×10^{-3}	94732	107K
$HZ \to b\bar{b}\tau^+\tau^-$, m_H=115 GeV	2.64×10^{-3}	97878	100K
$HZ \to b\bar{b}\tau^+\tau^-$, m_H=120 GeV	2.10×10^{-3}	94733	104K
$HZ \to b\bar{b}\tau^+\tau^-$, m_H=125 GeV	1.64×10^{-3}	97879	100K
$HZ \to b\bar{b}\tau^+\tau^-$, m_H=130 GeV	1.24×10^{-3}	97880	100K
$HZ \to b\bar{b}\tau^+\tau^-$, m_H=135 GeV	0.90×10^{-3}	97881	100K
$HZ \to b\bar{b}\tau^+\tau^-$, m_H=140 GeV	0.61×10^{-3}	94734	100K
$HZ \to b\bar{b}\tau^+\tau^-$, m_H=145 GeV	0.40×10^{-3}	97822	100K
$HZ \to b\bar{b}\tau^+\tau^-$, m_H=150 GeV	0.24×10^{-3}	94735	102K
$ZH \to q\bar{q}\tau^+\tau^-$, m_H=105 GeV	7.87×10^{-3}	102175, 89797	104K
$ZH \to q\bar{q}\tau^+\tau^-$, m_H=110 GeV	6.62×10^{-3}	94612,	103K
$ZH \to q\bar{q}\tau^+\tau^-$, m_H=115 GeV	5.55×10^{-3}	102176, 89798	102K
$ZH \to q\bar{q}\tau^+\tau^-$, m_H=120 GeV	4.46×10^{-3}	94613	107K
$ZH \to q\bar{q}\tau^+\tau^-$, m_H=125 GeV	3.51×10^{-3}	102177, 89799	103K
$ZH \to q\bar{q}\tau^+\tau^-$, m_H=130 GeV	2.67×10^{-3}	94614	100K
$ZH \to q\bar{q}\tau^+\tau^-$, m_H=135 GeV	1.94×10^{-3}	102178, 89800	102K
$ZH \to q\bar{q}\tau^+\tau^-$, m_H=140 GeV	1.34×10^{-3}	94615	100K
$ZH \to q\bar{q}\tau^+\tau^-$, m_H=145 GeV	0.89×10^{-3}	102179, 89801	102K
$ZH \to q\bar{q}\tau^+\tau^-$, m_H=150 GeV	0.53×10^{-3}	94616	103K
$WH \to q\bar{q}'\tau^+\tau^-$, m_H=105 GeV	12.92×10^{-3}	89892, 97857	153K
$WH \to q\bar{q}'\tau^+\tau^-$, m_H=110 GeV	10.77×10^{-3}	94592,	102K
$WH \to q\bar{q}'\tau^+\tau^-$, m_H=115 GeV	8.97×10^{-3}	89893, 97858	102K
$WH \to q\bar{q}'\tau^+\tau^-$, m_H=120 GeV	7.16×10^{-3}	94593,	100K
$WH \to q\bar{q}'\tau^+\tau^-$, m_H=125 GeV	5.59×10^{-3}	89894, 97859	104K
$WH \to q\bar{q}'\tau^+\tau^-$, m_H=130 GeV	4.20×10^{-3}	94594,	100K
$WH \to q\bar{q}'\tau^+\tau^-$, m_H=135 GeV	3.03×10^{-3}	89895, 97860	104K
$WH \to q\bar{q}'\tau^+\tau^-$, m_H=140 GeV	2.07×10^{-3}	94595,	100K
$WH \to q\bar{q}'\tau^+\tau^-$, m_H=145 GeV	1.34×10^{-3}	89896, 97861	104K
$WH \to q\bar{q}'\tau^+\tau^-$, m_H=150 GeV	0.81×10^{-3}	94596	102K

Table 3.1: The PYTHIA MC samples for signal processes, their cross-sections times branching ratio, internal DØ MC request ID's, and number of events generated.

Sample	σ_{NLO} (pb)	MC req-id	N_{events}
$qq' \to qq'H(\to \tau^+\tau^-)$, m_H=105 GeV	7.30×10^{-3}	94238, 97086, 110873	302K
$qq' \to qq'H(\to \tau^+\tau^-)$, m_H=110 GeV	6.64×10^{-3}	97093, 110874	260K
$qq' \to qq'H(\to \tau^+\tau^-)$, m_H=115 GeV	5.76×10^{-3}	94239, 97087, 110875	302K
$qq' \to qq'H(\to \tau^+\tau^-)$, m_H=120 GeV	4.86×10^{-3}	97094, 110876	250K
$qq' \to qq'H(\to \tau^+\tau^-)$, m_H=125 GeV	4.12×10^{-3}	94240, 97085, 110877	382K
$qq' \to qq'H(\to \tau^+\tau^-)$, m_H=130 GeV	3.31×10^{-3}	97095, 110878	253K
$qq' \to qq'H(\to \tau^+\tau^-)$, m_H=135 GeV	2.54×10^{-3}	94241, 97088, 110879	305K
$qq' \to qq'H(\to \tau^+\tau^-)$, m_H=140 GeV	1.83×10^{-3}	97096, 110880	252K
$qq' \to qq'H(\to \tau^+\tau^-)$, m_H=145 GeV	1.27×10^{-3}	94242, 97089, 110881	309K
$qq' \to qq'H(\to \tau^+\tau^-)$, m_H=150 GeV	0.81×10^{-3}	97097, 110882	251K
$WH \to H(\to WW)$ incl., m_H=105 GeV	5.61×10^{-3}	110725	203K
$WH \to H(\to WW)$ incl., m_H=110 GeV	9.54×10^{-3}	110723	202K
$WH \to H(\to WW)$ incl., m_H=115 GeV	14.79×10^{-3}	110726	203K
$WH \to H(\to WW)$ incl., m_H=120 GeV	21.06×10^{-3}	103313	200K
$WH \to H(\to WW)$ incl., m_H=125 GeV	27.78×10^{-3}	110727	203K
$WH \to H(\to WW)$ incl., m_H=130 GeV	34.22×10^{-3}	110724	202K
$WH \to H(\to WW)$ incl., m_H=135 GeV	39.63×10^{-3}	110728	202K
$WH \to H(\to WW)$ incl., m_H=140 GeV	43.61×10^{-3}	103314	200K
$WH \to H(\to WW)$ incl., m_H=145 GeV	45.95×10^{-3}	110729	203K
$WH \to H(\to WW)$ incl., m_H=150 GeV	46.97×10^{-3}	103315	200K
$WH \to H(\to WW)$ incl., m_H=155 GeV	47.30×10^{-3}	110730	204K
$WH \to H(\to WW)$ incl., m_H=160 GeV	46.90×10^{-3}	100512	207K
$WH \to H(\to WW)$ incl., m_H=165 GeV	45.04×10^{-3}	110731	200K
$WH \to H(\to WW)$ incl., m_H=170 GeV	39.92×10^{-3}	100513	200K
$WH \to H(\to WW)$ incl., m_H=175 GeV	35.12×10^{-3}	110732	201K
$WH \to H(\to WW)$ incl., m_H=180 GeV	30.30×10^{-3}	100514	200K
$WH \to H(\to WW)$ incl., m_H=185 GeV	24.11×10^{-3}	110733	200K
$WH \to H(\to WW)$ incl., m_H=190 GeV	19.84×10^{-3}	103317	200K
$WH \to H(\to WW)$ incl., m_H=195 GeV	17.07×10^{-3}	110734	200K
$WH \to H(\to WW)$ incl., m_H=200 GeV	14.91×10^{-3}	103318	200K
$qq' \to qq'H(\to WW)$, m_H=105 GeV	0.226×10^{-3}	91832, 92335	206K
$qq' \to qq'H(\to WW)$, m_H=110 GeV	0.419×10^{-3}	89832, 92336	204K
$qq' \to qq'H(\to WW)$, m_H=115 GeV	0.686×10^{-3}	89833, 92337	205K
$qq' \to qq'H(\to WW)$, m_H=120 GeV	1.026×10^{-3}	89834, 92338	205K
$qq' \to qq'H(\to WW)$, m_H=125 GeV	1.470×10^{-3}	89835, 92339	208K
$qq' \to qq'H(\to WW)$, m_H=130 GeV	1.931×10^{-3}	89836, 92340	204K

Table 3.2: The PYTHIA MC samples for signal processes, their cross-sections times branching ratio, internal DØ MC request ID's, and number of events generated.

Sample	σ_{NNLLO} (pb)	MC req-id	N_{events}
$qq' \to qq'H(\to WW)$, m_H=135 GeV	2.366×10^{-3}	89837, 92341	212K
$qq' \to qq'H(\to WW)$, m_H=140 GeV	2.714×10^{-3}	89838, 92342	206K
$qq' \to qq'H(\to WW)$, m_H=145 GeV	3.052×10^{-3}	89839, 92343	207K
$qq' \to qq'H(\to WW)$, m_H=150 GeV	3.304×10^{-3}	89840, 92344	201K
$qq' \to qq'H(\to WW)$, m_H=155 GeV	3.495×10^{-3}	89841, 92345	222 K
$qq' \to qq'H(\to WW)$, m_H=160 GeV	3.665×10^{-3}	89842, 92346	204 K
$qq' \to qq'H(\to WW)$, m_H=165 GeV	3.634×10^{-3}	89843, 92347	201 K
$qq' \to qq'H(\to WW)$, m_H=170 GeV	3.398×10^{-3}	89844, 92348	206 K
$qq' \to qq'H(\to WW)$, m_H=175 GeV	3.129×10^{-3}	89845, 92349	206 K
$qq' \to qq'H(\to WW)$, m_H=180 GeV	2.797×10^{-3}	89846, 92350	204 K
$qq' \to qq'H(\to WW)$, m_H=185 GeV	2.378×10^{-3}	89847, 92351	205 K
$qq' \to qq'H(\to WW)$, m_H=190 GeV	2.055×10^{-3}	89848, 92352	202 K
$qq' \to qq'H(\to WW)$, m_H=195 GeV	1.832×10^{-3}	89849, 92353	207 K
$qq' \to qq'H(\to WW)$, m_H=200 GeV	1.652×10^{-3}	89850, 92354	204 K
$ZH \to H(\to WW)$ incl., m_H=105 GeV	3.32×10^{-3}	113553	200.5K
$ZH \to H(\to WW)$ incl., m_H=110 GeV	5.699×10^{-3}	113554	203.5K
$ZH \to H(\to WW)$ incl., m_H=115 GeV	9.012×10^{-3}	113555	200.75K
$ZH \to H(\to WW)$ incl., m_H=120 GeV	12.822×10^{-3}	113556	203.75K
$ZH \to H(\to WW)$ incl., m_H=125 GeV	17.04×10^{-3}	113557	202.5K
$ZH \to H(\to WW)$ incl., m_H=130 GeV	21.19×10^{-3}	113558	203K
$ZH \to H(\to WW)$ incl., m_H=135 GeV	24.633×10^{-3}	113559	203.5K
$ZH \to H(\to WW)$ incl., m_H=140 GeV	27.038×10^{-3}	113560	201.2K
$ZH \to H(\to WW)$ incl., m_H=145 GeV	28.98×10^{-3}	111252	200K
$ZH \to H(\to WW)$ incl., m_H=150 GeV	29.631×10^{-3}	113561	200K
$ZH \to H(\to WW)$ incl., m_H=155 GeV	29.99×10^{-3}	117998	200K
$ZH \to H(\to WW)$ incl., m_H=160 GeV	29.86×10^{-3}	117999	200K
$ZH \to H(\to WW)$ incl., m_H=165 GeV	28.77×10^{-3}	118000	200K
$ZH \to H(\to WW)$ incl., m_H=170 GeV	26.025×10^{-3}	118001	200K
$ZH \to H(\to WW)$ incl., m_H=175 GeV	22.994×10^{-3}	118002	200K
$ZH \to H(\to WW)$ incl., m_H=180 GeV	19.582×10^{-3}	118003	200K
$ZH \to H(\to WW)$ incl., m_H=185 GeV	16.055×10^{-3}	118004	200K
$ZH \to H(\to WW)$ incl., m_H=190 GeV	13.379×10^{-3}	118005	200K
$ZH \to H(\to WW)$ incl., m_H=195 GeV	11.382×10^{-3}	118006	200K
$ZH \to H(\to WW)$ incl., m_H=200 GeV	10.396×10^{-3}	118007	200K

Table 3.3: The PYTHIA MC samples for signal processes, their cross-sections times branching ratio, MC request ID's, and number of events generated.

Sample	σ_{NNLLO} (pb)	MC req-id	N_{events}
$gg \to H(\to \tau^+\tau^-)$ incl., m_H=105 GeV	126.5 $\times 10^{-3}$	94232	103K
$gg \to H(\to \tau^+\tau^-)$ incl., m_H=110 GeV	107.1 $\times 10^{-3}$	88854	530K
$gg \to H(\to \tau^+\tau^-)$ incl., m_H=115 GeV	90.4 $\times 10^{-3}$	94233	105K
$gg \to H(\to \tau^+\tau^-)$ incl., m_H=120 GeV	74.2 $\times 10^{-3}$	88855	517K
$gg \to H(\to \tau^+\tau^-)$ incl., m_H=125 GeV	59.2 $\times 10^{-3}$	94234	103K
$gg \to H(\to \tau^+\tau^-)$ incl., m_H=130 GeV	45.5 $\times 10^{-3}$	88856	510K
$gg \to H(\to \tau^+\tau^-)$ incl., m_H=135 GeV	33.6 $\times 10^{-3}$	94235	101K
$gg \to H(\to \tau^+\tau^-)$ incl., m_H=140 GeV	23.7 $\times 10^{-3}$	88857	506K
$gg \to H(\to \tau^+\tau^-)$ incl., m_H=145 GeV	15.79 $\times 10^{-3}$	94236	100K
$gg \to H(\to \tau^+\tau^-)$ incl., m_H=150 GeV	9.74 $\times 10^{-3}$	88858	535K
$gg \to H(\to WW)$ lept., m_H=105 GeV	14.73 $\times 10^{-3}$	92314, 93494, 93495	720K
$gg \to H(\to WW)$ lept., m_H=110 GeV	12.65 $\times 10^{-3}$	90383, 92315, 93496, 93497	700K
$gg \to H(\to WW)$ lept., m_H=115 GeV	10.76 $\times 10^{-3}$	90384, 92316, 93498, 93499	70K
$gg \to H(\to WW)$ lept., m_H=120 GeV	15.65 $\times 10^{-3}$	93500, 93501, 92317	608K
$gg \to H(\to WW)$ lept., m_H=125 GeV	21.09 $\times 10^{-3}$	90385, 92318, 93502, 93503	920K
$gg \to H(\to WW)$ lept., m_H=130 GeV	26.51 $\times 10^{-3}$	89357, 92319, 93504, 93505	701K
$gg \to H(\to WW)$ lept., m_H=135 GeV	31.36 $\times 10^{-3}$	90386, 92320, 93506, 93507	708K
$gg \to H(\to WW)$ lept., m_H=140 GeV	35.19 $\times 10^{-3}$	92321, 93508, 93509	604K
$gg \to H(\to WW)$ lept., m_H=145 GeV	37.94$\times 10^{-3}$	90387, 92322, 93510, 93511	709K
$gg \to H(\to WW)$ lept., m_H=150 GeV	39.64$\times 10^{-3}$	89353, 92323, 93512, 93513	712K
$gg \to H(\to WW)$ lept., m_H=155 GeV	40.76$\times 10^{-3}$	89355, 92324, 93514, 93515	699K
$gg \to H(\to WW)$ lept., m_H=160 GeV	41.69$\times 10^{-3}$	92325, 93516, 93517	613K
$gg \to H(\to WW)$ lept., m_H=165 GeV	39.17$\times 10^{-3}$	89356, 92326, 93518, 93519	720K
$gg \to H(\to WW)$ lept., m_H=170 GeV	35.31$\times 10^{-3}$	89354, 92327, 93520, 93521	719K
$gg \to H(\to WW)$ lept., m_H=175 GeV	31.58$\times 10^{-3}$	90388, 92328, 93522, 93523	706K
$gg \to H(\to WW)$ lept., m_H=180 GeV	27.7$\times 10^{-3}$	92329, 93524, 93525	616K
$gg \to H(\to WW)$ lept., m_H=185 GeV	22.62$\times 10^{-3}$	90389, 92330, 93526, 93527	714K
$gg \to H(\to WW)$ lept., m_H=190 GeV	19.08$\times 10^{-3}$	90390, 92331, 93528, 93529	708K
$gg \to H(\to WW)$ lept., m_H=195 GeV	17.728$\times 10^{-3}$	90391, 92332, 93530, 93531	726K
$gg \to H(\to WW)$ lept., m_H=200 GeV	14.96$\times 10^{-3}$	92333, 93532, 93533	605K

Table 3.4: The PYTHIA MC samples for signal processes, their cross-sections times branching ratio, MC request ID's, and number of events generated. The abbreviation "lept." means that the W bosons are decayed to any lepton (e, μ, or τ)

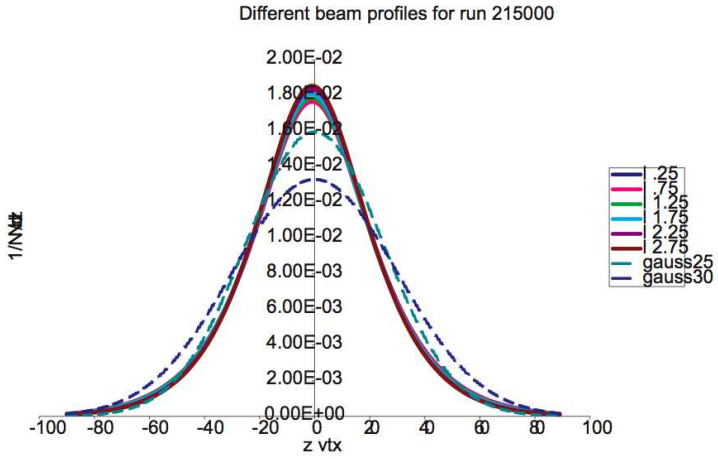

Figure 3.5: The beam shape distributions for different luminosity bins in data (solid lines), and for two gaussians of width 25 and 30 cm (dashed lines). Simulations use a gaussian representation plus a correction.

3.4 Signal Selection

Data events are selected for the analysis according to the criteria below. An overview of the selection is given and details about electron, tau, and jet identification follow. The leading jet (with the highest p_T) is referred to as "jet 1" and the next leading jet is referred to as "jet 2".

- Require an electron candidate with $p_T > 15$ GeV and $|\eta_{\rm det}| < 1.1$ or $1.5 < |\eta_{\rm det}| < 2.5$; electron selection criteria is described in detail below.
- Require a hadronic τ candidate with the opposite charge to the electron; τ selection is described fully below.
- Require at least two good jets with $p_{T\rm jet1} > 20$ GeV, $p_{T\rm jet2} > 15$ GeV, and $|\eta| < 3.4$, which are separated from the e and τ candidates by $\Delta R(e, jet) > 0.5$ and $\Delta R(\tau, jet) > 0.5$.
- $\Delta z_{\rm vtx}$ between electron and tau less than 1.5 cm, to ensure the electron and tau are from the same collision.
- No events with an additional "top-tight electron" (see below, Section 3.4.1) with $p_T > 15$ GeV are allowed, so as to be orthogonal to the $Z(ee) + H$ and $ee + \not\!\!E_T$ analyses;
- No events with a muon of $p_T > 12$ GeV and $|\eta| < 2.0$ are allowed.

3.4.1 Electron Selection

Electrons are reconstructed using the information listed below gathered from the calorimeter and the central fiber tracker. The set of cuts is called TopTight at DØ. The variables used here are described in Section 2.3.8.

- Isolation is required to be less than 0.15. The isolation is defined as $(E_{tot}(R = 0.4)$ - $E_{EM}(R = 0.2))$ / $(E_{EM}(R = 0.2))$, where $(E_{tot}(R = 0.4)$ is the total energy in a cone of radius 0.4 and $E_{EM}(R = 0.2)$ is the EM energy in a cone of radius 0.2. This cut helps separate primary-interaction electrons from electrons radiated by jets.
- The EMFraction is greater than 0.9.
- The calorimeter cluster is matched spatially to a track (a χ^2 of the matching is created and required to be greater than 0).

- For electrons in the end cap: the ratio of calorimeter energy to momentum calculated in the tracker is less than 2.5.
- The H-matrix, HMx7, is less than 50.0.
- The transverse momentum calculated from the track is greater than 5.0 GeV.
- The LogLikelihood is greater than 0.85.

3.4.2 Tau Selection

General τ identification is described in Section 2.3.9. Using these standard criteria it was found that a large background of $Z \rightarrow ee$ events was present in the selection. (See Figure 3.6.) A collection of cuts beyond the standard τ selection is used to combat this background from $Z \rightarrow ee$.

Type 2 τs are defined in a similar way to electrons (requiring both a track and an EM calorimeter subcluster) and so DØ has developed a neural net (NNel) to especially distinguish Type 2 τs from electrons. In this analysis we require that the type 2 NNel value be above 0.95.

Beyond this, electrons tend to fake τs in areas where there is limited EM calorimeter information: the ICR region and the regions at the edges of the calorimeter modules. We require that Type 1 and 3 τs be outside the ICR region, and that Type 2 τs are away from calorimeter module boundaries.

In the case of Type 3 τs, the EM fraction distribution was found to be especially helpful in distinguishing $Z \rightarrow ee$ background.

In summary, we make the following requirements to remove the cases in which an electron from $Z \rightarrow ee$ fakes a τ ("anti-electron cuts"):

- Require Type 1 τs to be outside the intercryostat region (ICR): $1.05 < \eta_\tau < 1.5$;
- Require Type 2 τ's, to have $\mathrm{NN}_e > 0.95$ and to be far from CCEM boundaries ($0.1 < \phi^\tau_{\mathrm{CPS}} < 0.9$), where ϕ^τ_{CPS} is the ϕ coordinate taken from the Central Preshower Detector.
- Require Type 3 τ's, to have EMF < 0.95 and to be outside the ICR region, $1.1 < \eta_\tau < 1.5$.

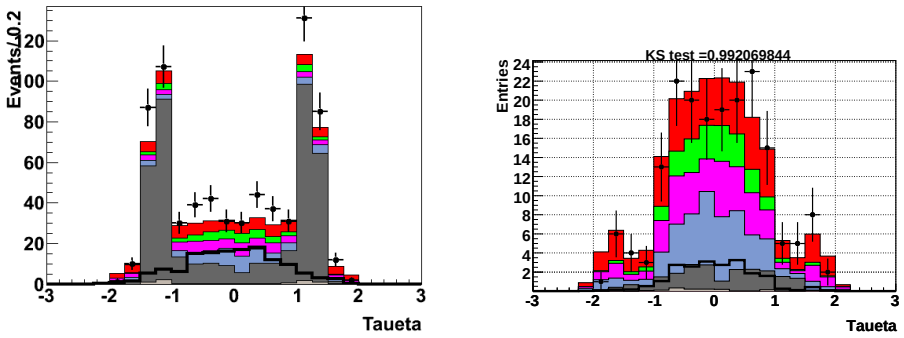

Figure 3.6: Tau η including the NNel cut but without any of the other "anti-electron" cuts (left) and with all cuts (right).

3.4.3 Jet Selection

Jets are reconstructed using a cone algorithm with R = 0.5. This is described in more detail in the detector section 2.3.8.

For this analysis we require events to have two or more jets that satisfy the following criteria:

- Jet $|\eta| < 3.4$
- Leading jet $p_T > 20.0$ GeV; additional jets $p_T > 15.0$ GeV
- Jets must be separated from the τ and e with ΔR > 0.5
- Jets must be vertex confirmed (see Section 2.3.8)

3.4.4 Missing Transverse Energy

Although the signals in this analysis contain neutrinos in the final states, we do not make a specific cut requiring that there be missing transverse energy ($\not\!\!E_T$) in selected events. But the calculated $\not\!\!E_T$ enters in to many of the variables used in BDT training, and it is discussed in section 2.3.12.

3.4.5 Further removing multijet events

An additional cut is made to specifically remove multijet background and background from Z decays. These are the most significant backgrounds in the analysis, and they are large compared to, for example, the same backgrounds

in the $\tau(\mu)\tau$jetjet analysis because jets and jet fragments in the multijet background can easily fake electrons, and an electron from $Z \rightarrow ee$ can fake a τ.

A cut on the variable $\not\!\!E_T$ Significance was found to be helpful in reducing multijet and Z background. This variable aims to quantify how likely it is that calculated $\not\!\!E_T$ is from neutrinos rather than from mismeasurement of energy in the event. The $\not\!\!E_T$ significance algorithm creates a probability distribution ($p(\not\!\!E_T)$) of the $\not\!\!E_T$ based on the energy resolutions of objects in each event. The $\not\!\!E_T$ Significance is based on the number of standard deviations the $\not\!\!E_T$ probability is away from 0. (High $\not\!\!E_T$ significance means the $\not\!\!E_T$ is more likely due to neutrinos than mismeasurement.)

$$\not\!\!E_T\text{Sig} = S = 2\log\frac{\not\!\!E_T^2}{2\sigma} \tag{3.6}$$

where σ is the variance of the probability distribution $p(\not\!\!E_T)$ [13].

The distribution of the $\not\!\!E_T$sig before the cut is made is shown in Figure 3.7, and Figure 3.8 shows the same distributions after the cut. Placing a cut at 1.0 reduces the multijet background by about 60 percent and also reduces the $Z(ee)$ +jets background by about 60 percent. The signals involving $H \rightarrow \tau^+\tau^-$ are cut by about 15 percent, and the signals involving $H \rightarrow WW$ are cut by about 5 percent.

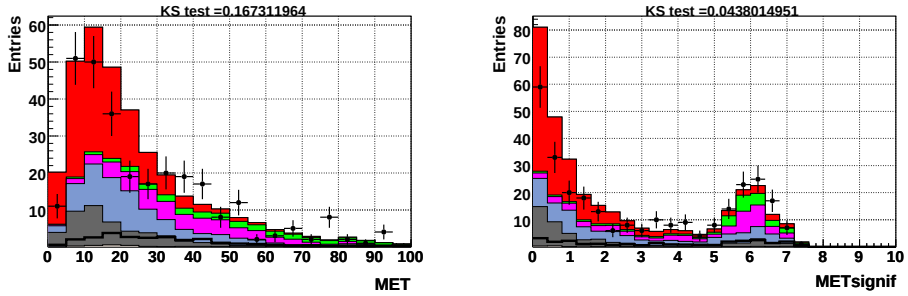

(a) (b)

Figure 3.7: (a) The $\not\!\!E_T$ without a cut on the $\not\!\!E_T$ significance. (b) The $\not\!\!E_T$ significance without a cut.

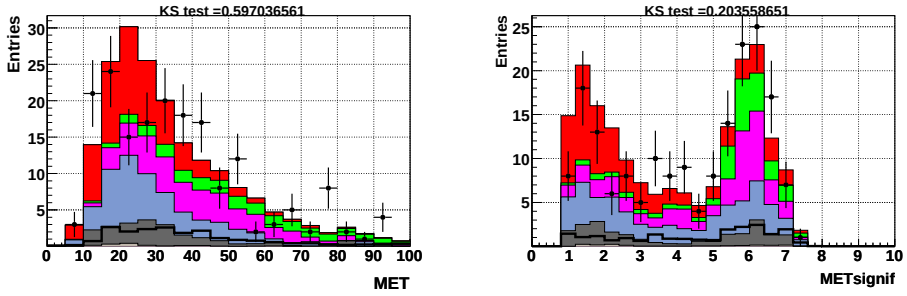

(a) (b)

Figure 3.8: (a) The $\not\!\!E_T$ with the cut on the $\not\!\!E_T$ significance at 1.0. (b) The $\not\!\!E_T$ significance with the cut at 1.0.

3.5 Multijet Background Estimation

The largest background to the $\tau(e)\tau$ jet jet search is from multijet (MJ) processes. The $p\overline{p}$ collisions at the Tevatron produce a huge number of events with low energy jets. This multijet background is poorly modeled by Monte Carlo simulations, so we estimate it using data. This is done by selecting a multijet-enriched data sample that is similar kinematically to our signal selection data but which fails specific anti-jet cuts:

- Choose events with an electron that passes the TopLoose requirement but fails the TopTight requirement. The difference between TopLoose and TopTight is the inclusion of the ElectronLhood8 requirement for the TopTight case. See section 3.4.1 the description of TopTight.
- Additionally, take only events with TauNN values between 0.3 and 0.9 (rather than TauNN > 0.9 as for signal selection).
- All other selection cuts are the same as for the signal selection, except that there is no requirement that the electron and τ have different signs.

This data sample is estimated to be 97% multijet and 3% other backgrounds. This is found by applying these cuts to the monte carlo samples of the other backgrounds.

The data is normalized using the ratio of opposite sign (OS) events and same sign (SS) events, which is assumed to be the same in the MJ-enriched sample and the signal sample. The normalization to the MJ-enriched sample is calculated as follows: Take ρ to be the ratio of the number of OS to SS events in the multijet-enriched sample,

$$\rho = M_{OS}/M_{SS}. \tag{3.7}$$

where M is the number of events (OS or SS) in the multijet enriched sample (after the 3 percent from other backgrounds passing MJ cuts has been removed). Then the number of OS multijet background events in the signal sample is

$$N_{OS} = \rho \cdot N_{SS} \tag{3.8}$$

where N_{SS} is the number of SS events in the signal sample, after the SS events from monte carlo estimated backgrounds has been removed. In summary, the multijet background is modeled by taking the MJ-enriched sample (for shape) and normalizing it to $\rho \cdot N_{SS}$.

The scale factor ρ was calculated separately for each τ type. The distribution of OS/SS ratio values was plotted versus the p_T of the τ, electron and leading jet, and fit to a constant. These distributions are plotted in Fig. 3.9 and the fit values are listed in Table 3.5. The scale factor was also checked for η and p_T dependancies, as shown in Figure 3.10, but none were observed.

	τ type 1	τ type 2	τ type 3
N_{events}	313	1692	3577
purity	0.97	0.95	0.96
ρ	1.10±0.16	1.00±0.06	0.98±0.04

Table 3.5: The number of events in the MJ-enriched sample, the purity (fraction of events estimated to be multijet as opposed to other background processes), and the scale factors, by τ type.

Some variation in τ types is seen as a function of Tau NN. As the τs become "less good" with lower TauNN values, there is more migration between τ types. For example the ratio of the number of type 2 τs to all taus is lower when low TauNN τs are included than when only "good" high NN τs are included. A study was done to see if these type variations should be accounted for in the multijet estimation, which uses low NN taus. Since the multijet normalization factors are applied according to τ type, the normalization could be affected by a variation in the designation of tau type. The number of τs of each type relative to the total number of τs was calculated for different cuts on the TauNN variable. In Figure 3.11 this is plotted over the relative number τs of each type compared to the total with standard TauNN cuts of 0.9, 0.9, and 0.95.

$$\zeta_x = \frac{(\frac{n_{typex}}{n_{Alltypes}})}{(\frac{h_{typex}}{h_{Alltypes}})} \tag{3.9}$$

where n is the number of events with the variable NN cut and h is the number of events with the standard high NN cut. Figure 3.11 show there is some migration between τ types when lower TauNN events are included in a sample. The ζ value was taken as an inverse scaling factor to the MJ-enriched sample to correct for this effect. Figure 3.12 compares the distribution of τ types with and without the scaling applied to the MJ. Though there is some change due to the scaling factors, the magnitude of the correction has a negligible effect on the final results, and the factors were not applied through the full analysis.

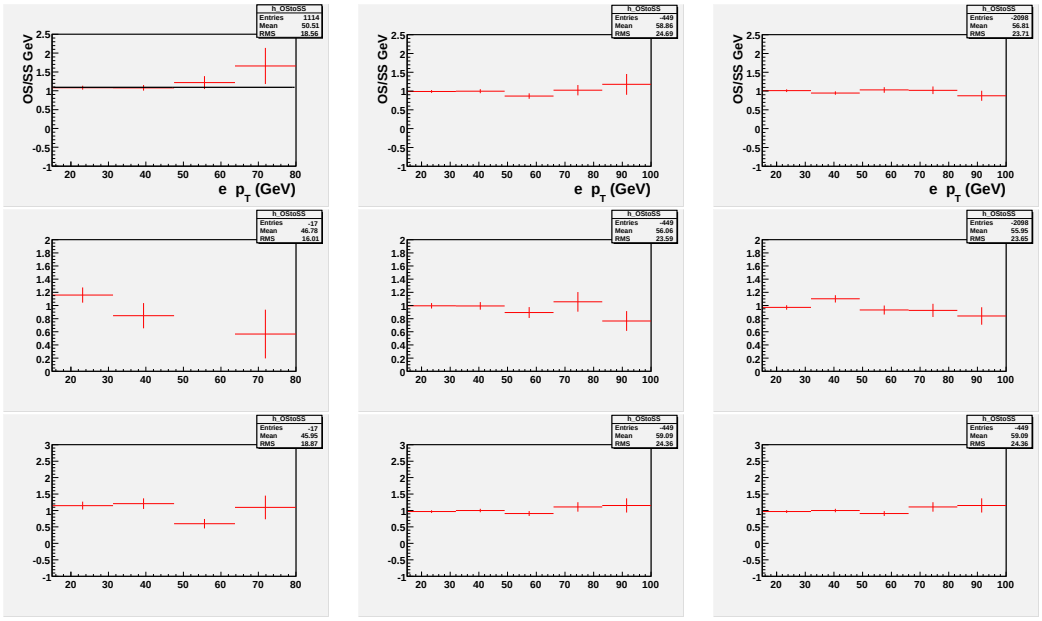

Type 1 τ Type 2 τ Type 3 τ

Figure 3.9: Distributions of the ratio of OS to SS events in the MJ enriched sample, as function of p_T^e (top), p_T^τ (middle) and p_T^{jet1} (bottom) for different τ types.

In order to test the estimation of the multijet background, another sample is made using the same MJ-enriching cuts, but requiring exactly 1 jet in the selection, rather than at least 2. The low statistics of the 2-jet sample could hide multijet mis-modeling under statistical error bars, so the data-background

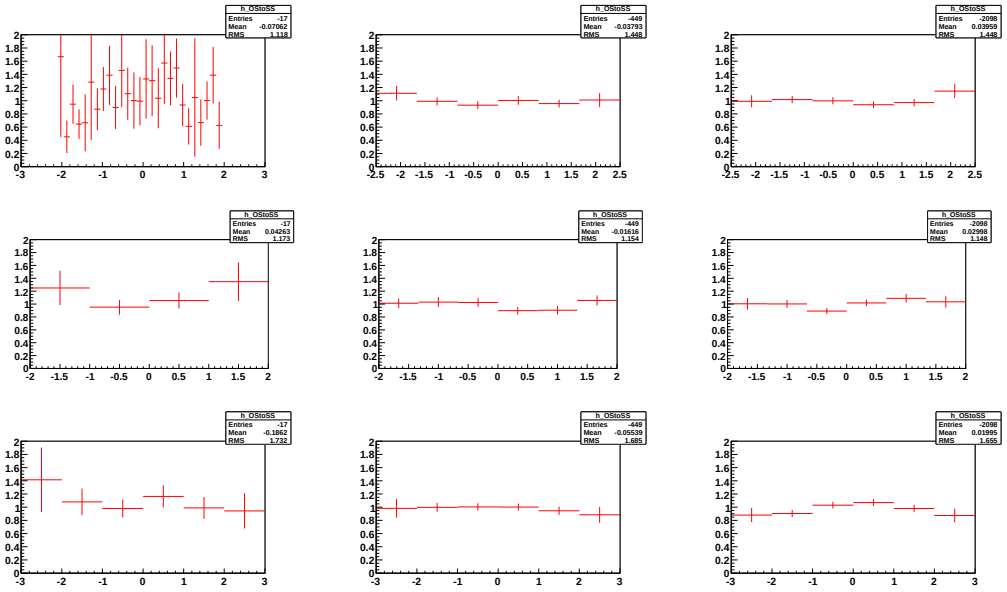

Type 1 τ Type 2 τ Type 3 τ

Figure 3.10: Distributions of the ratio of OS to SS events in the MJ enriched sample, as function of η_e (top), η_τ (middle) and η_{jet1} (bottom) for different τ types.

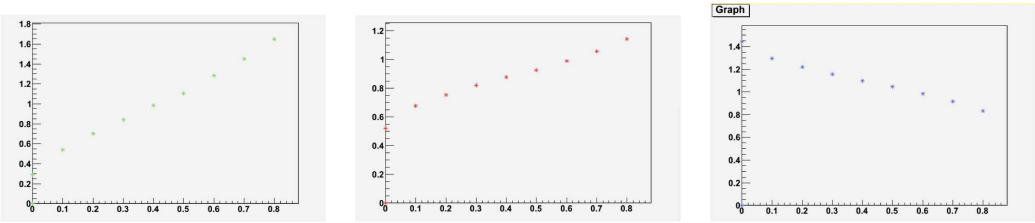

Figure 3.11: The variable ζ (Eq. 3.9) versus the lower bound on TauNN used to select the taus, for type 1(left), type 2 (middle) and type 3 (right). In all cases the upper bound is 0.9. The standard MJ-enriched sample uses events with TauNN between 0.3 and 0.9. The fact that ζ is not constant with TauNN means that a sample of taus will have a different proportion of each type of tau depending on the choice of TauNN used to select the sample.

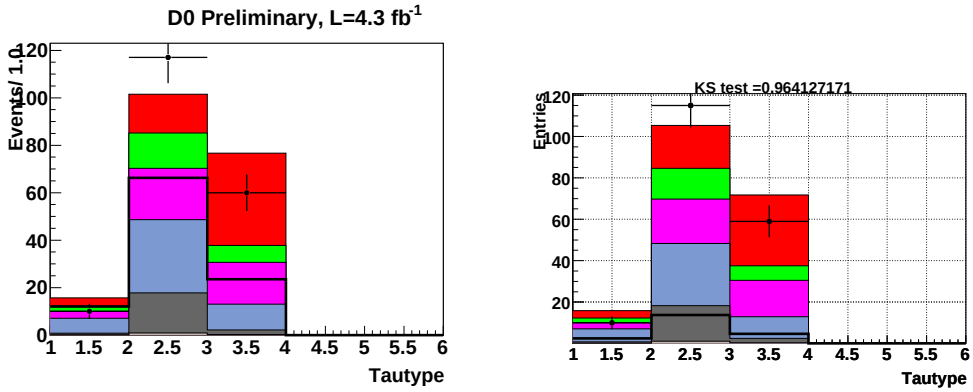

Figure 3.12: The distribution of τ types before (left) and after (right) the type migration factor, ζ (Fig. 3.11), has been applied to the multijet.

agreement is checked in the higher-statistics 1-jet sample. The degree to which the MJ-enriched sample successfully models the multijet background should not depend on the number of jets required. A few chosen variable distributions for the 1-jet sample are shown in Figure 3.13. The agreement between data and background estimation is acceptable.

To estimate systematics on the multijet estimation, the two special MJ criteria are taken one at a time:

- MJ-enriched variant 1. Require a TopLoose electron which fails the TopTop selection; all other selection as for the signal.
- MJ-enriched variant 2. Require a τ with $0.3 <$ TauNN < 0.9; all other selection as for the signal.

Calculation of systematics is discussed further in section 3.8.

3.6 Event Yields and Comparison between Data and Background Estimation

Table 3.6 shows the number of events in the 4.3 fb^{-1} data sample selected according to the criteria described in Section 3.4. Yields are also listed for the MC simulated backgrounds and the estimated MJ background, and good agreement is seen between these and the number of data events.

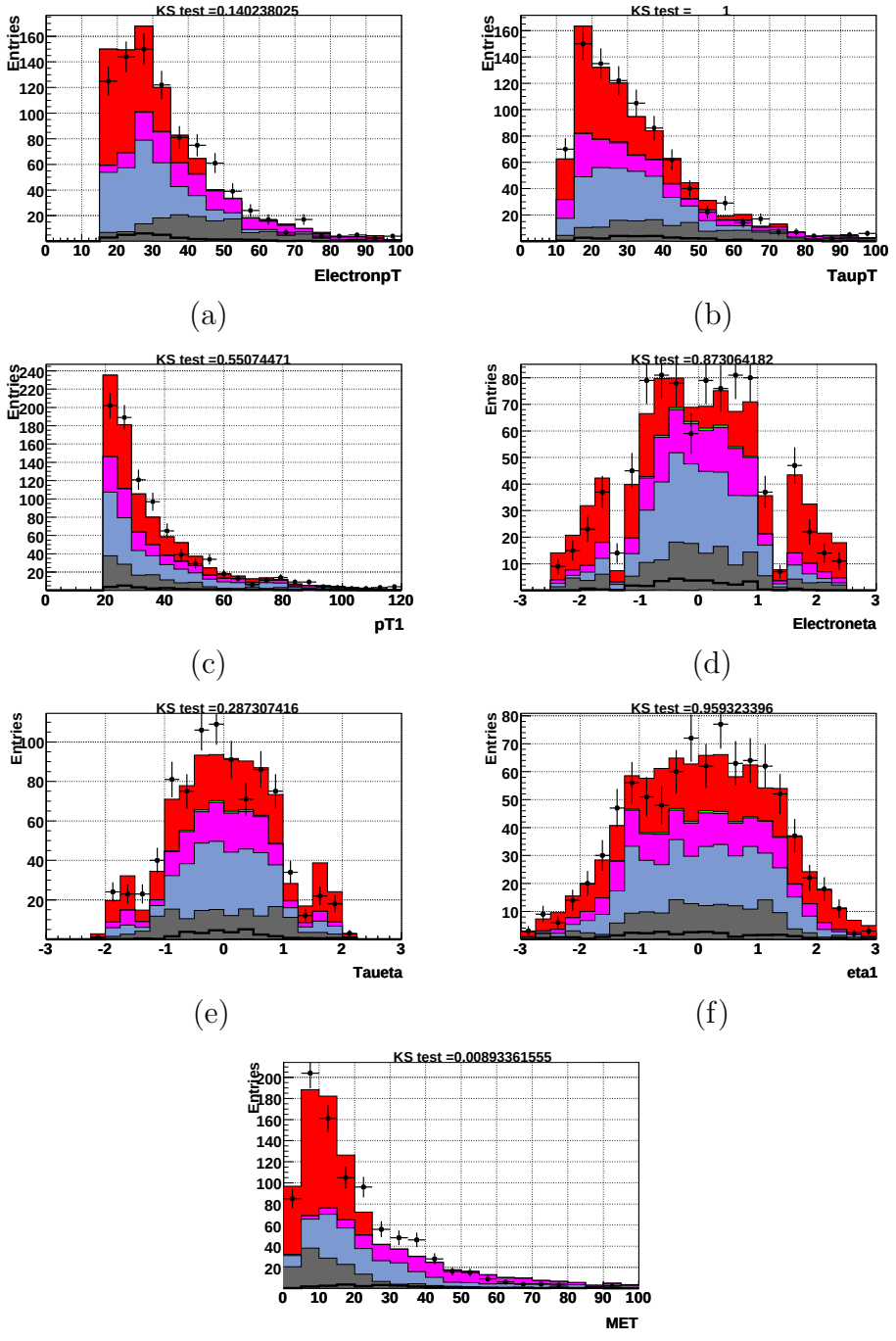

Figure 3.13: Data - MC comparisons for the $e\tau$ + 1 jet sample: (a) p_T^e; (b) p_T^τ; (c) p_T^{jet}; (d) η^e; (e) η^τ; (f) η^{jet} (g) $\not\!\!E_T$.

τ type	Data	Σbkgd	$t\bar{t}$	W+jets	Z_{ee}+jets	$Z_{\tau\tau}$+jets	DB	MJ
All	188	198.3	24.4	42.6	19.8	48.6	3.6	59.2
type 1	10	18.8	2.3	2.9	0.6	6.3	0.6	6.0
type 2	117	118.4	14.9	21.8	17.2	30.9	1.5	32.0
type 3	61	61.1	7.2	17.8	2.0	11.4	1.4	21.7

Table 3.6: After preselection, the number of data and the expected Standard Model and MJ backgrounds for both the total and individual τ types. "DB" stands for di-boson processes.

Distributions of kinematic variables are shown in Figures 3.14, 3.15, 3.16, and 3.17. Good agreement is seen between the background estimates and the data.

An additional modeling check is done using an inclusive sample of $e + \tau$ events. Without a jet requirement this sample has almost 40 times the statistics of our 2-jet signal sample. Event yields for the inclusive sample are listed in Table 3.7. Distributions are plotted by τ type in Figures 3.18 through 3.20. The data and MC agreement vary by τ type, but overall the modeling is considered to be adequate. The disagreement seen in the type 2 Tau-Electron invariant mass is in part due to the fact that one of the electrons from $Z \to e^+e^-$ background events passing our selection cuts receives τ energy scale corrections. This effect has been lessened by turning off the τ energy scale corrections for τs with EM fraction over 0.9 (i.e. those with most of their energy in the EM rather than hadronic layers of the calorimeter). There is disagreement between data and predicted background in the MET distributions. This discrepancy in MET is most severe in the inclusive sample, still somewhat present in the 1 jet sample (Fig. 3.13), but almost not visible at all in the 2 jet case. There is also an ongoing study by others in the DØ collaboration on the effect of low energy background events on the modeling of MET, which may prove relevant to the inclusive case. While this is not fully understood, the agreement in the 2 jets case is sufficient to believe that the MET is well modeled in that case.

3.7 Multivariate Analysis

Even with the multiple search signals combined in this analysis the ratio of signal to background is very low. A single set of cuts to separate the signals from background is not sufficient. Multivariate analysis is used to separate the

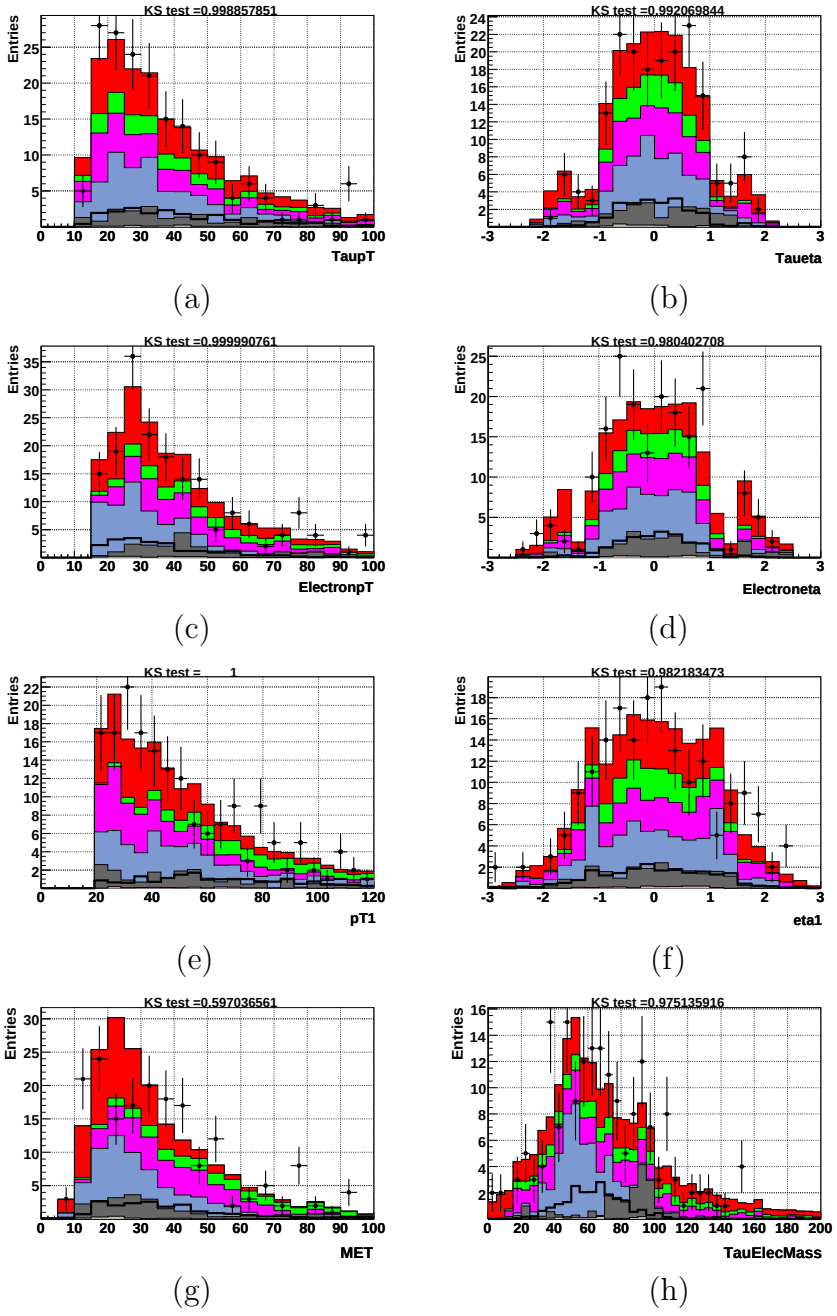

Figure 3.14: Data - MC comparison for BDT input variables: (a) p_T^τ; (b) η_τ (c) p_T^e (d) η_e (not used as BDT input); (e) p_{Tjet1} (f) η_{j1} (not used as BDT input); (g) $\not\!\!E_T$ (h) $M_{\tau\tau}$. Signal curves are for m_H=115 GeV and have been multiplied by a factor of 100.

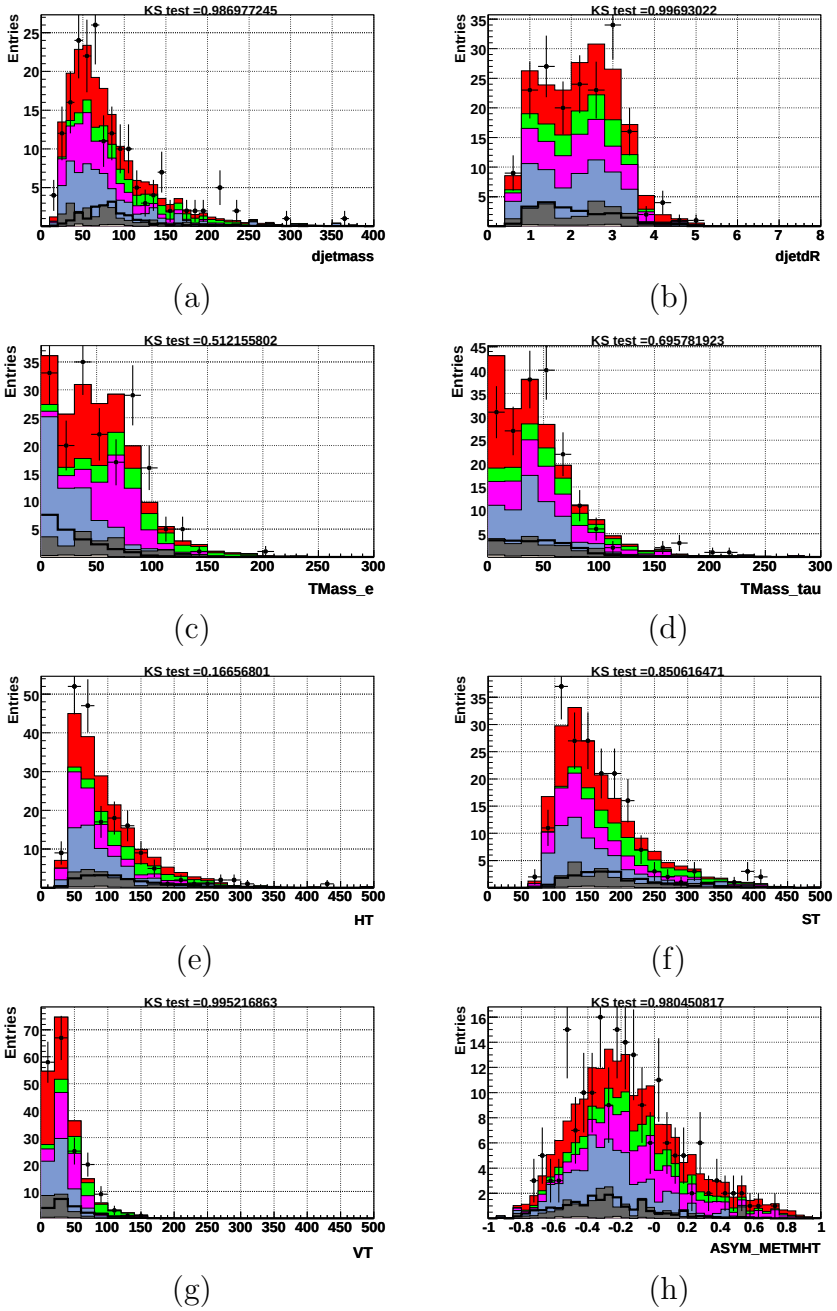

Figure 3.15: Data - MC comparison for BDT input variables: (a) $M_{\rm jj}$; (b) $\Delta R_{\rm jj}$; (c) $M_{\rm T}^{e}$; (d) $M_{\rm T}^{\tau}$; (e) H_T; (f) S_T; (g) V_T; (h) $A(\not\!\!E_T, \not\!\!H_T)$; Signal curves are for m_H=115 GeV and have been multiplied by a factor of 100.

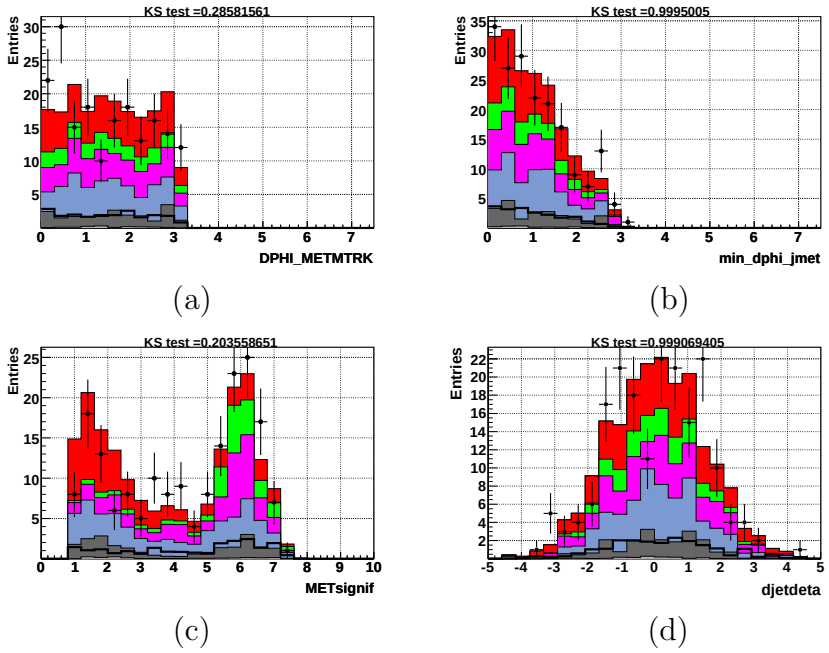

Figure 3.16: Data - MC comparison for BDT input variables: (a) $\Delta\phi(\not\!\!E_T, \not\!\!T_T)$; (b) $\min\Delta\phi(\not\!\!E_T, jets)$; (c) $\mathcal{S}$; (d) $\Delta\eta$(jj); Signal curves are for m_H=115 GeV and have been multiplied by a factor of 100.

τ type	Data	Σbkgd	$t\bar{t}$	W+jets	Z_{ee}+jets	$Z_{\tau\tau}$+jets	DB	MJ
All	7150	7086.3	33.7	1308.2	1211.2	2506.1	5.8	2021.4
type 1	641	718.5	3.2	139.0	26.3	324.2	0.4	225.4
type 2	4464	4374.0	21.0	677.9	1069.2	1554.0	4.3	1047.7
type 3	2054	1993.8	9.5	491.3	115.7	627.9	1.1	748.3

Table 3.7: After preselection in the inclusive analysis, the number of data and the expected Standard Model and MJ backgrounds for both the total and individual tau types. "DB" stands for di-boson processes.

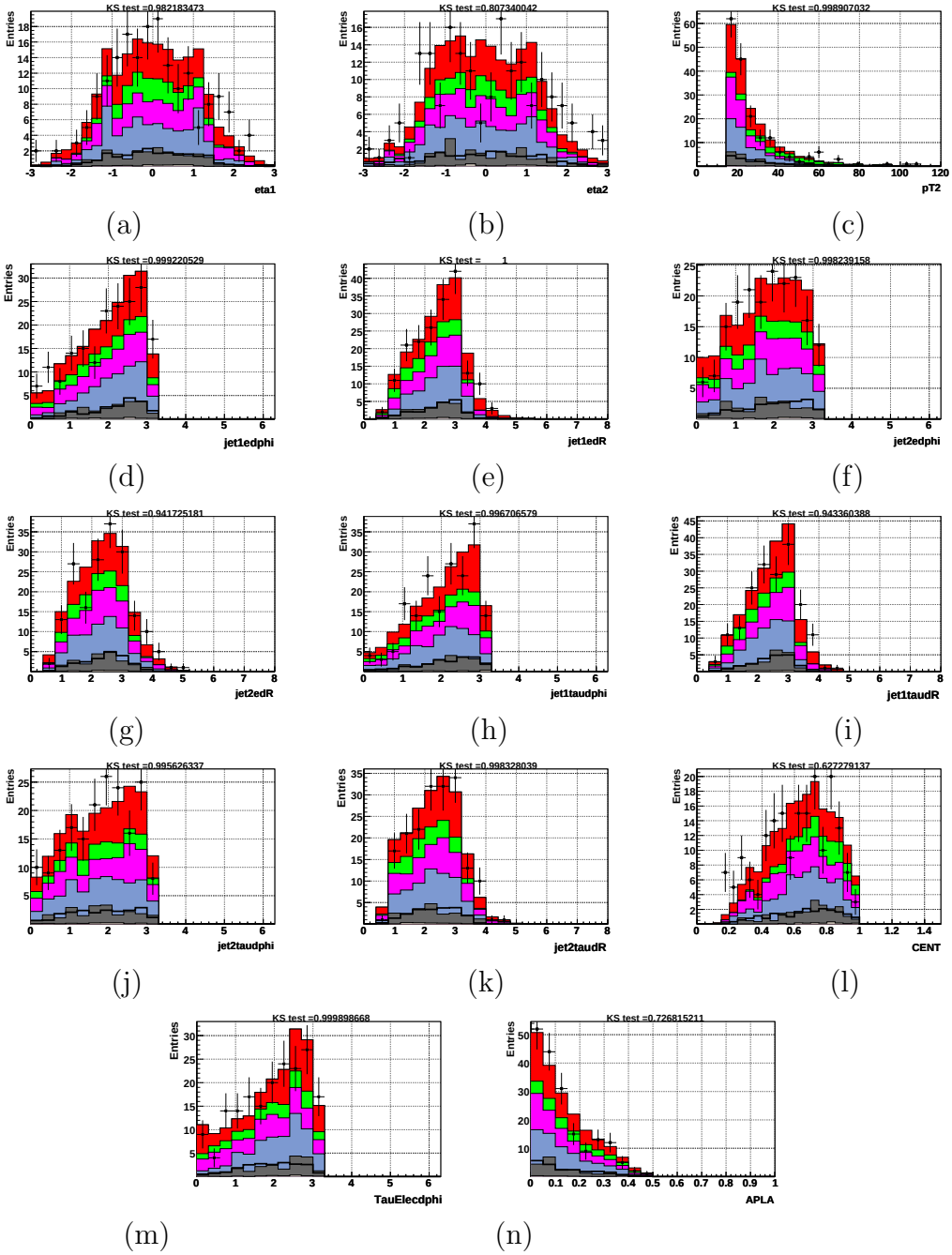

Figure 3.17: Data and MC distributions for non-BDT inputs: (a) jet1 η; (b) jet2 η; (c) p_T(jet2); (d) $\Delta\phi$(jet1,e); (e) ΔR(jet1,e); (f) $\Delta\phi$(jet2,e); (g) ΔR(jet2,e); (h) $\Delta\phi$(jet1,τ); (i) ΔR(jet1,τ); (j) $\Delta\phi$(jet2,τ); (k) ΔR(jet2,τ); (l) $\mathcal{C}$; (m) $\Delta\phi_{e\tau}$; and (n) $\mathcal{A}$. The signal curves are shown for m_H=115 GeV and have been multiplied by a factor of 100.

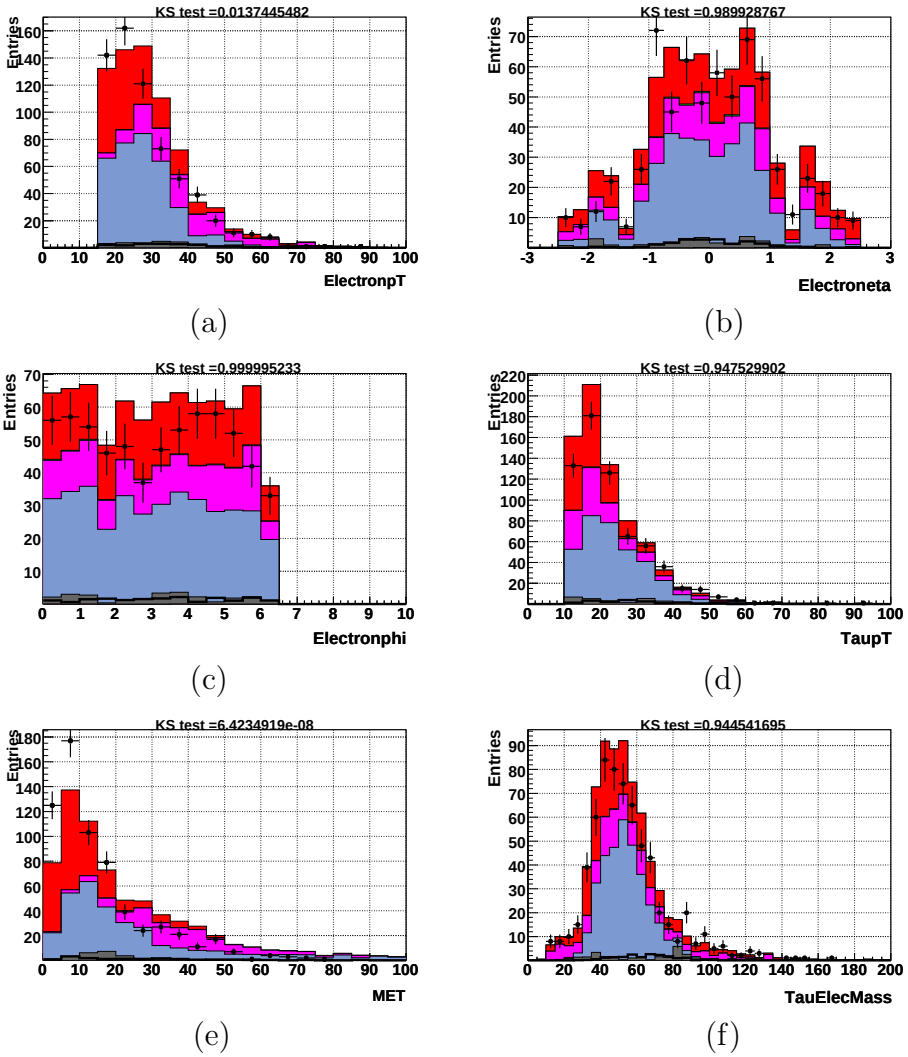

Figure 3.18: Comparison data and MC for the inclusive $e\tau$ selection with type 1 τ's: (a) p_T^e; (b) η_e; (c) ϕ^e; (d) p_T^τ; (e) $\not\!\!E_T$; (f) $m(e\tau)$.

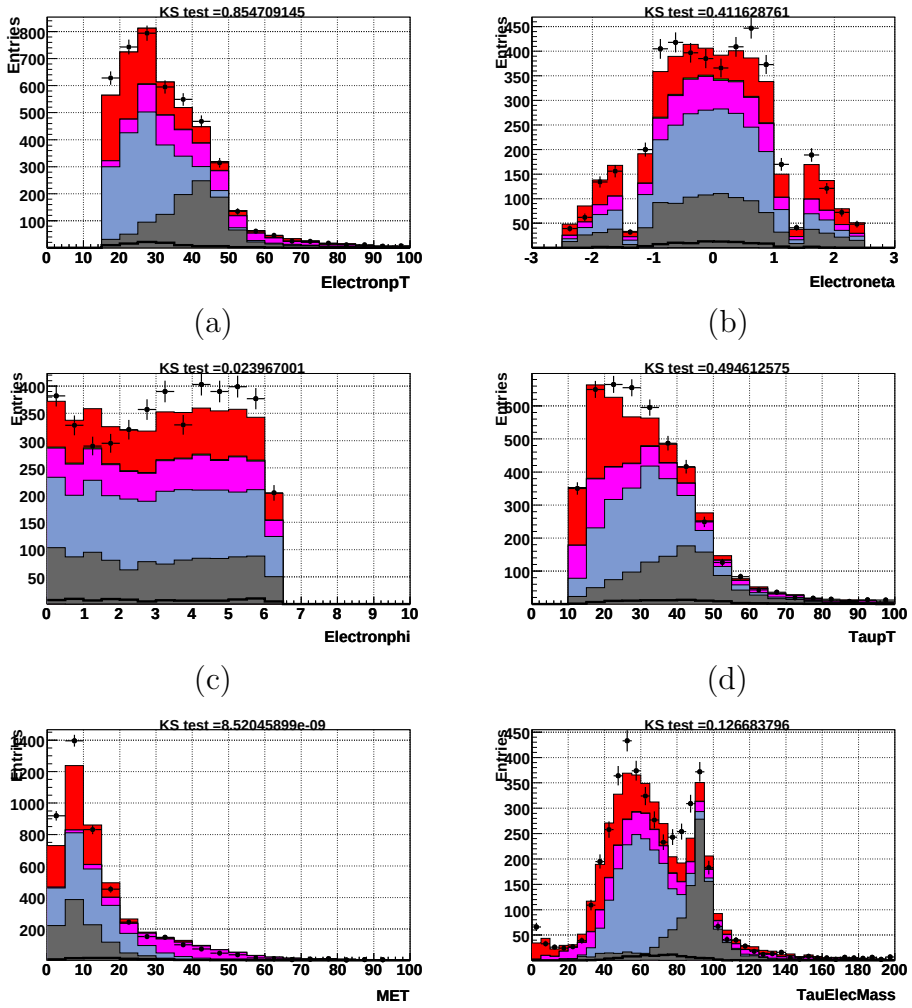

Figure 3.19: Comparison data and MC for the inclusive $e\tau$ selection with type 2 τ's: (a) p_T^e; (b) η_e; (c) ϕ^e; (d) p_T^τ; (e) $\not{E}_T$; (f) $m(e\tau)$.

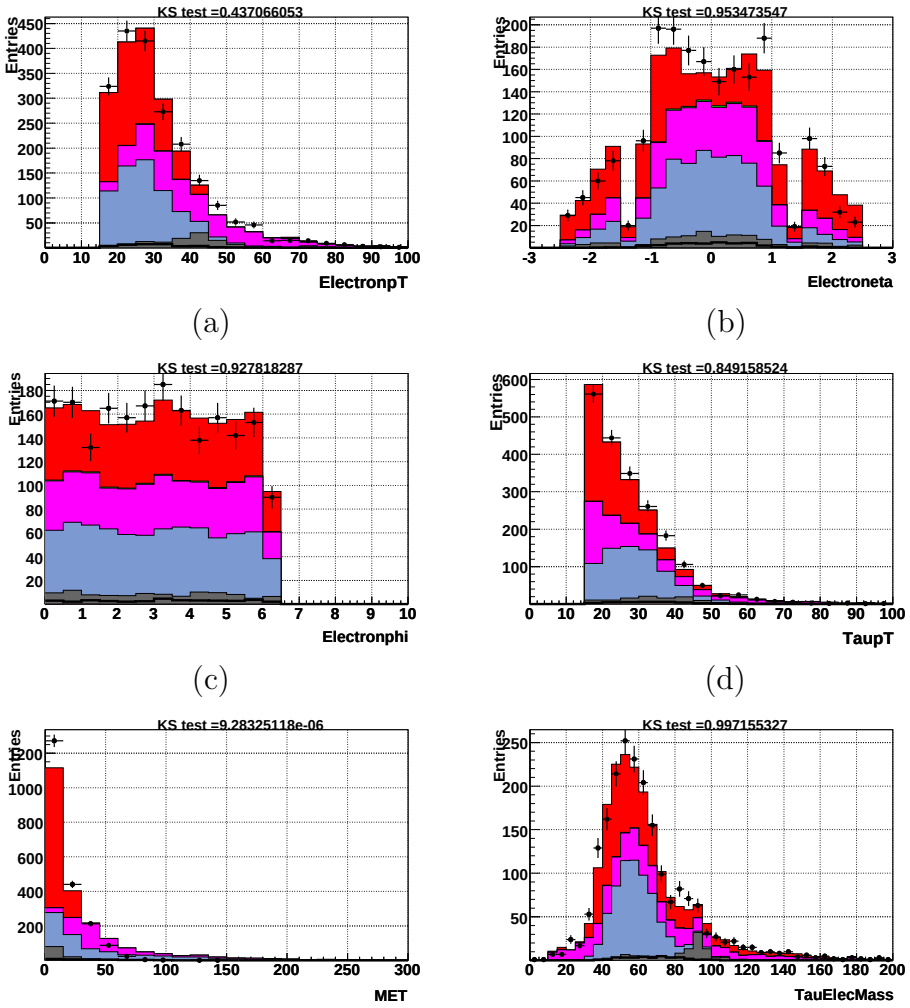

Figure 3.20: Comparison data and MC for the inclusive $e\tau$ selection with type 3 τ's: (a) p_T^e; (b) η_e; (c) ϕ^e; (d) p_T^τ; (e) $\not\!\!E_T$; (f) $mass(e\tau)$.

different signals from the different backgrounds.

We use Stochastic Gradient Boosted Decision Trees, which are implemented inside the ROOT TMVA package (version 4.0.3) [20]. A decision tree uses a training sample of known signal and background events to calculate the optimum set of kinematic cuts to separate the signal and background. The training sample is first split into two groups (nodes) consisting of the events that passed a cut on a particular kinematic variable and those that failed. The variable and the cut is decided based on optimizing the purity, p, equal to $s/(s+b)$, where s and b are the weighted sums of signal and background events, respectively, in the parent sample. A purity near 1 or near 0 is equally desirable, essentially representing the separation of background from signal, or signal from background. A purity of 0.5 means a cut is minimally discriminating. This measure of discrimination is classified using the Gini index, $p(1-p)$. The Gini index of the two daughter nodes after a cut are weighted by the number of events in the nodes and summed. The variable cut is chosen which maximally decreases this index sum compared to the Gini index of the parent node.

Then the procedure is repeated on the resulting nodes separating them further by signal and background. This continues iteratively until no improvement in signal-background separation is found or until a set number of nodes has been created ($MaxN_{nodes}$). (Choosing a small number of maximal nodes helps prevent overtraining, in which fluctuations in the sample are given too much import in the training.) The final nodes are called leaves. Each leaf represents a set of kinematic cuts. The leaf purity is calculated to give a final designation of how signal- or background-like events passing these cuts are.

The optimized cuts are applied to the data, and events are assigned a final discriminant value as either more signal-like (here given a value closer to 1.0) or more background-like (closer to -1.0).

When the MVA discriminating power is not overly strong, the addition of "boosting" can be used to increase performance. This technique creates many BDTs, and in each iteration the results are compared to the known signal-background separation, and events which were misclassified are given a higher weight when put into the next iteration. Then the weighted average of all the BDTs is taken for the final discriminant. The weighting in this average is optimized against the known signal-background relation. The figure of merit for this optimization is the loss function, which relates the final weighted-average discriminant to the known separation. The method of optimizing of the weighted average is a choice in TMVA. An earlier version of this analysis (in the $\mu\tau$ jetjet channel) used the method called AdaBoost, which takes an exponential loss function. This method can be affected by outliers in the

dataset. The current version of the analysis uses gradient boosting, which takes a binomial log-likelihood loss function and optimizes using the method of steepest descent. This was found to have a 10% improvement in signal discrimination over AdaBoost.

The parameters that can be adjusted for gradient BDT's in TMVA include the number of trees, the shrinkage, the bagging fraction, and the maximum number of nodes.

The shrinkage slows the learning rate of the BDTs by successively reweighting tree outputs to give slightly less strong discrimination so that more trees must be created to give a final result. This has the effect of diminishing fluctuations which might cause a false signal or background designation from overtraining due to statistical fluctuations. The shrinkage parameter is chosen to be 0.6.

Bagging refers to a resampling technique which retrains BDTs using different subsamples of training events. This helps to minimized statistical fluctuations. In stochastic gradient boosting, random subsamples of events are chosen for training each tree. The fraction of the training sample used for each tree is 60%.

These parameters were optimized in the $\mu\tau jetjet$ analysis. They were varied up and down, and the resulting BDTs were evaluated based on a figure of merit defined as the percentage of signal remaining when 75% of the background has been cut out. Quantities listed in Table 3.8 reflect the parameters which gave the highest figure of merit values.

BDT parameter settings	
$N_{trees} = 400$	shrinkage = 0.6
bagging fraction = 0.6	$MaxN_{nodes} = 15$

Table 3.8: Parameters used in Stochastic Gradient Boosted Decision Trees.

The following 17 variables were used as input into the BDTs. Their rank of discrimination for one example signal-background training is listed in Table 3.11 (different signal-background combinations give different discriminating ranks). Variables were chosen which had some difference in distribution between the signals and the backgrounds and had decent data-background modeling. BDTs are, in general, less degraded by inputs which do not have helpful signal-background discrimination, compared to Neural Net techniques.

1. p_T^e: p_T of the electron candidate
2. p_T^{j1}: p_T of the leading jet candidate

3. $\not\!\!E_T$: missing transverse energy

4. $M_{\tau\tau}$: invariant mass of the τ_e – τ_{had} system. The $\not\!\!E_T$ is apportioned to the e and τ as follows. The $\not\!\!E_T$ is projected on the axis, $\hat{A}$, taken as the direction $\vec{p}_T^{\,e} - \vec{p}_T^{\,\tau}$ to give projection MET_A. The $\not\!\!E_T$ associated with the e is $(1 + \mathrm{MET}_A)/2$ and that associated with the τ is $(1 - \mathrm{MET}_A)/2$. The neutrino p_z is estimated by assuming the p_z/p_T is the same for neutrino and the associated visible products of either tau.

5. M_{jj}: invariant mass of the two candidate jets

6. ΔR_{jj}: $\Delta R = \sqrt{(\Delta\phi)^2 + (\Delta\eta)^2}$ is the distance in azimuth ϕ and pseudo-rapidity η between the two leading jets

7. M_{T}^{e}: transverse mass calculated from the p_T^e and $\not\!\!E_T$

8. M_{T}^{τ}: transverse mass calculated from the p_T^τ and $\not\!\!E_T$

9. H_T: scalar sum of the p_T of all jets with $p_T > 15$ GeV and $|\eta| < 3.4$

10. S_T: the scalar sum of the p_T of the electron candidate, the tau candidate, the two candidate jets and of the event missing transverse energy, $S_T = p_T(e) + p_T(\tau) + p_T(jet1) + p_T(jet2) + \not\!\!E_T$

11. V_T: the magnitude of the vector sum of the p_Ts of the electron candidate, the tau candidate, the two candidate jets and the event missing transverse energy, $V_T = |\overrightarrow{p_T^e} + \overrightarrow{p_T^\tau} + \overrightarrow{p_T^{jet1}} + \overrightarrow{p_T^{jet2}} + \overrightarrow{\not\!\!E_T}$—

12. $A(\not\!\!E_T, \not\!\!H_T)$: Asymmetry between $\not\!\!E_T$ and $\not\!\!H_T$, $(\not\!\!E_T - \not\!\!H_T)/(\not\!\!E_T + \not\!\!H_T)$, where $\not\!\!H_T$ is the missing H_T, defined as the magnitude of the vector sum of all jet p_T's

13. $\Delta\phi(\not\!\!E_T, \not\!\!T_T)$: the azimuthal angle difference between $\not\!\!E_T$ and the missing transverse momentum, $\not\!\!T_T$, calculated as the negative of the vector sum of the p_T of all tracks with at least 8 CFT hits and a DCA to the primary vertex of less than 2 mm (DCA defined in section 2.3.8)

14. $\min\Delta\phi(\not\!\!E_T, jets)$: the minimum azimuthal angle difference between the $\not\!\!E_T$ and any good jet

15. $\mathcal{S}$: the $\not\!\!E_T$ 'signficance' [13]

16. $\Delta\eta$(jj): the absolute value of the pseudorapidity difference between the two leading jets

17. p_T^τ: the transverse momentum of the hadronic tau candidate

18. $M_{\tau\tau}$: This invariant mass is constructed in the modified collinear approximation for the neutrino 3-momenta. We assume that the neutrinos from a tau decay are collinear with the visible decay products ($\phi_{\nu_i} = \phi_{\text{vis}_1} \equiv \phi_i$) and ($\theta_{\nu_i} = \theta_{\text{vis}_1} \equiv \theta_i$) for tau's i=1, 2. We assume also that the $\not\!\!E_T$ in the event is solely due to neutrinos, so that the equations

$$\not\!\!E_{T_x} = p(\nu_1)\sin\phi_1\cos\phi_1 + p(\nu_2)\sin\phi_2\cos\phi_2 \tag{3.10}$$

$$\not\!\!E_{T_y} = p(\nu_1)\sin\phi_1\sin\phi_1 + p(\nu_2)\sin\phi_2\sin\phi_2 \tag{3.11}$$

relate the observable $\not\!\!E_T$ and visible decay product angles. The solution of these equations for $p(\nu_1)$ and $p(\nu_2)$ is well behaved so long as the determinant, $D = \cos\phi_2\sin\phi_1 - \cos\phi_1\sin\phi_2$, is non-zero. When the two taus are back to back ($\phi_1 = \phi_2 + \pi$) D=0. In the case that $D \leq 0.01$, we substitute for the collinear approximation solution by apportioning the $\not\!\!E_T$ as $p(\nu_1) = \not\!\!E_T E_1/(E_1 + E_2)$ and $p(\nu_2) = \not\!\!E_T E_2/(E_1 + E_2)$; we retain the assumption of collinearity of the neutrino and the visible tau decay products' momenta.

The nine signals that this analysis is sensitive to have different kinematic distributions. In order to keep from suppressing some signals, one would like to train a different BDT for each signal against each of the five backgrounds, separately for each of 20 signal mass points. This would give 5 x 9 x 20 = 900 BDT outputs. This is a very large number of BDTs to manage, and the number can be reduced if we take advantage of patterns in the signals and backgrounds. Figure 3.21 shows the fractional signal yield as a function of Higgs mass. Signals that contribute less than 10% of the total in a given mass region are not given their own training in the multivariate analysis. Also, the behavior of the signals from 105 to 120 and from 140 to 200 is fairly constant (H to $\tau\tau$ signals dominate in the low mass and H to WW in the high mass). Rather than taking the twenty mass points separately we group together a low mass region from 105 to 120 GeV, an intermediate mass region from 125 to 135 GeV, and a high mass region from 140 to 200 GeV. Additionally WH and ZH have similar kinematics, and training from each of these signals gives similar results, so the WH and ZH signals are combined into one BDT training ("VH"). The $t\bar{t}$ and $Wjets$ backgrounds also behave similarly in training and so these backgrounds are combined. The diboson background is very small and does not have its own training. So we train selected signals against three backgrounds (MJ, $t\bar{t}$ + $Wjets$, and $Zjets$). After these considerations we are

left with 9 BDTs in the low mass, 12 in the intermediate, and 9 BDTs in the high mass region. The signals trained in each mass region are listed in Table 3.9.

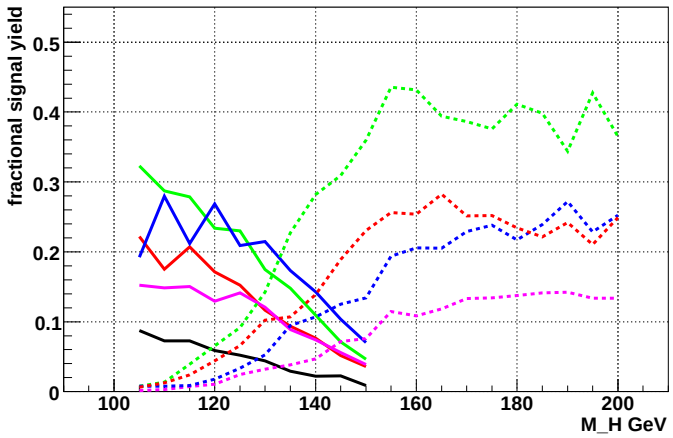

Figure 3.21: Fractional yields for signals as a function of Higgs boson mass. The H to $\tau\tau$ signals dominate in the low mass and the H to WW dominate in the high mass. In the intermediate region (130 GeV to 140 GeV) the GGF and WH processes (in either $\tau\tau$ or WW mode) dominate.

Higgs mass region	Signals			
low	$GGF_{\tau\tau}$	$VH_{\tau\tau}$	$VBF_{\tau\tau}$	
intermediate	$GGF_{\tau\tau}$	GGF_{WW}	$VH_{\tau\tau}$	VH_{WW}
high	GGF_{WW}	VH_{WW}	VBF_{WW}	

Table 3.9: Signals used for BDT training in the three Higgs boson mass ranges

.

BDT outputs from the training are shown in Figures 3.24 through 3.33. In these plots values near 1 are signal-like and values near -1 are background-like. The majority of the BDTs show good separation between signals and backgrounds being trained, but there is also a significant number of outputs in which some signals not being trained are pushed to the background side and vice versa. See especially WH and ZH trained against the $Z + jets$ background in the intermediate mass range (Figure 3.29 (a)(b)), or the outputs

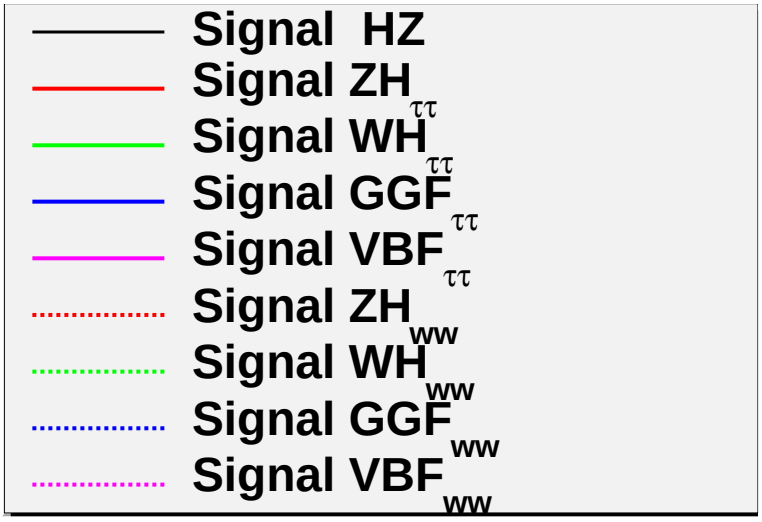

Figure 3.22: Key used in the data-MC comparison plots for signals.

from training against the $t\bar{t}$ and $Wjets$ background in the high mass (Figure 3.31).

In order to combine the information from the BDTs and combat this problem, we look for a way to further discriminate the signals and backgrounds using these BDT outputs. In the present analysis we choose to take the BDT outputs as input variables to a 2nd iteration of "combined" BDTs (cBDTs), separately for the low, intermediate, and high mass regions. The three combined BDTs were trained using the individual BDTs from each signal-background pair. The results of the cBDT training are shown in Figure 3.37 (a), (c), (e).

In the low mass combined BDT there is still some background in the signal region, and the data-background agreement is not optimal. To investigate this we selected events with cBDTs above 0.4 and plotted the individual BDTs for these events. Figures 3.34 and 3.35 show the individual BDTs with only the events above 0.4 in the original combined BDT. Here we can see that in the BDTs trained against the MJ background there is significant MJ background left in the signal region after the combined BDT cut at 0.4. Speculating that this was not helpful in the training of the combined BDT, we retrained without the input BDTs VH versus MJ and VBF versus MJ. The resulting combined BDT had less background in the signal region and the expected limits derived from the combined BDT were improved by 15%. Dropping the GGF vs MJ BDT did not improve the final combined BDT or limits.

The same procedure was applied to the transition and high mass regions. The individual BDTs with a cut at 0.4 on the combined BDTs are shown in Figure 3.36. In the transition region we trained the combined BDT without the MJ background trained BDTs (each separately and together), but no improvement was seen in the final combined BDT nor in the expected limits. In the high mass region improvement was seen when the combined BDT was trained without any of the input BDTs trained against MJ background.

Table 3.10 gives a summary of the inputs to the final combined BDTs.

The method for combining the BDT information has an optimization that is difficult to predict, and it is worth describing what was done in the previous version of the $\mu\tau jj$ analysis. In that case a cut was made on the individual BDT with the maximum signal discriminate value. Define

$BDT^B = Max[BDT(ZH, B), BDT(HZ, B), BDT(HW, B), BDT(VBF, B)]$

for the backgrounds (B) $t\bar{t}$, $Wjets$, and MJ. A cut was made at -0.2, -0.2 and 0 for BDT^{ttbar}, BDT^{Wjets}, BDT^{MJ}, respectively. Only events on the signal side of this cut were kept, thus a large portion of the background was removed. To make a final single discriminant, the weighted average of the BDTs trained against the $Zjets$ background was taken [21].

m_H region	Signals v. Backgrounds in cBDT training		
low	GGF$_{\tau\tau}$ - $t\bar{t}W$	VH$_{\tau\tau}$ - $t\bar{t}W$	VBF$_{\tau\tau}$ - $t\bar{t}W$
	GGF$_{\tau\tau}$ - $Zjets$	VH$_{\tau\tau}$ - $Zjets$	VBF$_{\tau\tau}$ - $Zjets$
	GGF$_{\tau\tau}$ - MJ		
trans.	GGF$_{\tau\tau}$- $t\bar{t}W$	GGF$_{WW}$- $t\bar{t}W$	
	VH$_{\tau\tau}$- $t\bar{t}W$	VH$_{WW}$- $t\bar{t}W$	
	GGF$_{\tau\tau}$ - $Zjets$	GGF$_{WW}$ - $Zjets$	
	VH$_{\tau\tau}$ - $Zjets$	VH$_{WW}$ - $Zjets$	
	GGF$_{\tau\tau}$ - MJ	GGF$_{WW}$ - MJ	
	VH$_{\tau\tau}$ - MJ	VH$_{WW}$ - MJ	
high	GGF$_{WW}$ - $t\bar{t}W$	VH$_{WW}$ - $t\bar{t}W$	VBF$_{WW}$ - $t\bar{t}W$
	GGF$_{WW}$ - $Zjets$	VH$_{ww}$ - $Zjets$	VBF$_{ww}$ - $Zjets$

Table 3.10: Signals and background BDTs used as input for the 2nd iteration combined BDT training in the three Higgs mass ranges. Better performance was seen after dropping VBF-MJ and VH-MJ BDTs from the low mass training, and dropping all the BDTs trained against multijet from the high mass training.

.

variable	VH vs. $t\bar{t}/W$jets (low mass)	GGF($\tau\tau$) vs. multijet (int. mass)	GGF(WW) vs. Z+ jets (high mass)
p_T^e	10	14	10
p_T^{j1}	8	15	14
$\not{E}_T$	15	13	13
$M_{\tau\tau}$	17	10	17
M_{jj}	5	17	16
ΔR_{jj}	13	9	6
M_{T}^e	1	3	1
M_{T}^τ	6	12	11
H_T	7	1	8
S_T	12	16	15
V_T	3	11	2
$A(\not{E}_T, \not{H}_T)$	4	7	5
$\Delta\phi(\not{E}_T, \not{E}_T^{trk})$	11	2	3
$\min\Delta\phi(\not{E}_T, jets)$	16	4	4
$\mathcal{S}$	2	8	7
$\Delta\eta(\mathrm{jj})$	14	6	9
p_T^τ	9	5	12

Table 3.11: Rank of each input BDT variable (1 is most discriminating) for representative BDTs

Figure 3.23: Legends for all histograms.

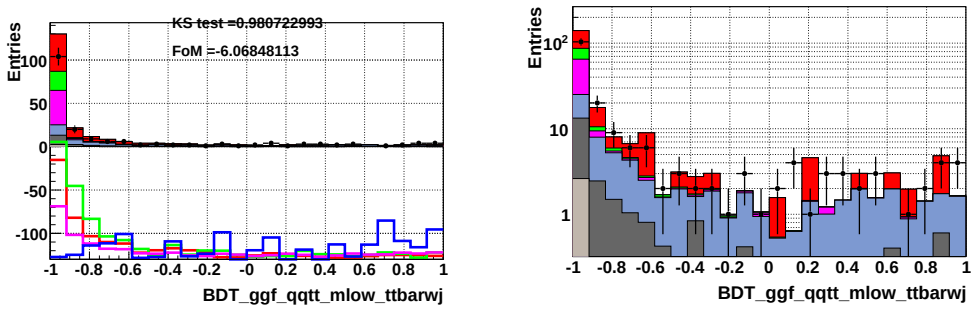

(a)

(b)

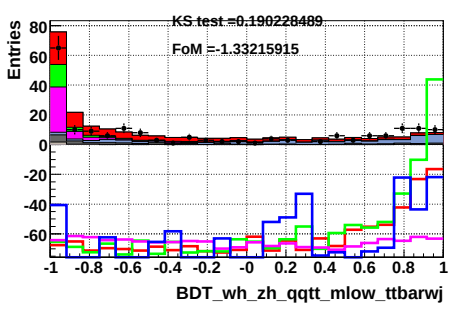

(c)

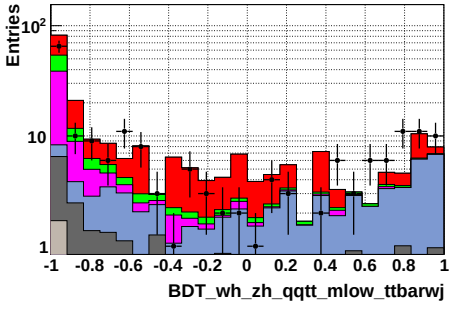

(d)

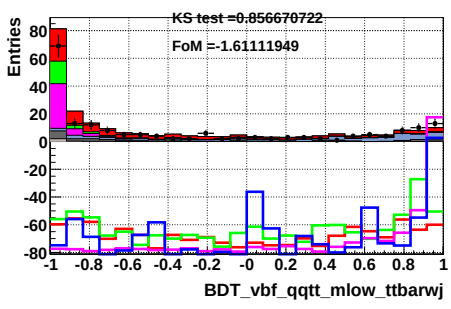

(e)

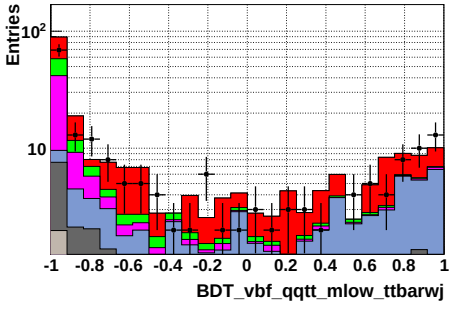

(f)

Figure 3.24: BDT outputs for low Higgs mass, trained between the $t\bar{t}$ and $W + jets$ backgrounds and the signals (a), (b) $GGF_{\tau\tau}$, (c), (d) $VH_{\tau\tau}$, and (e), (f) $VBF_{\tau\tau}$. The linear outputs are on the left and the log outputs are on the right. In the linear outputs the signals are plotted separately from the backgrounds so that the shapes can be more easily seen; the negative values on the y-axis for the signals should be ignored.

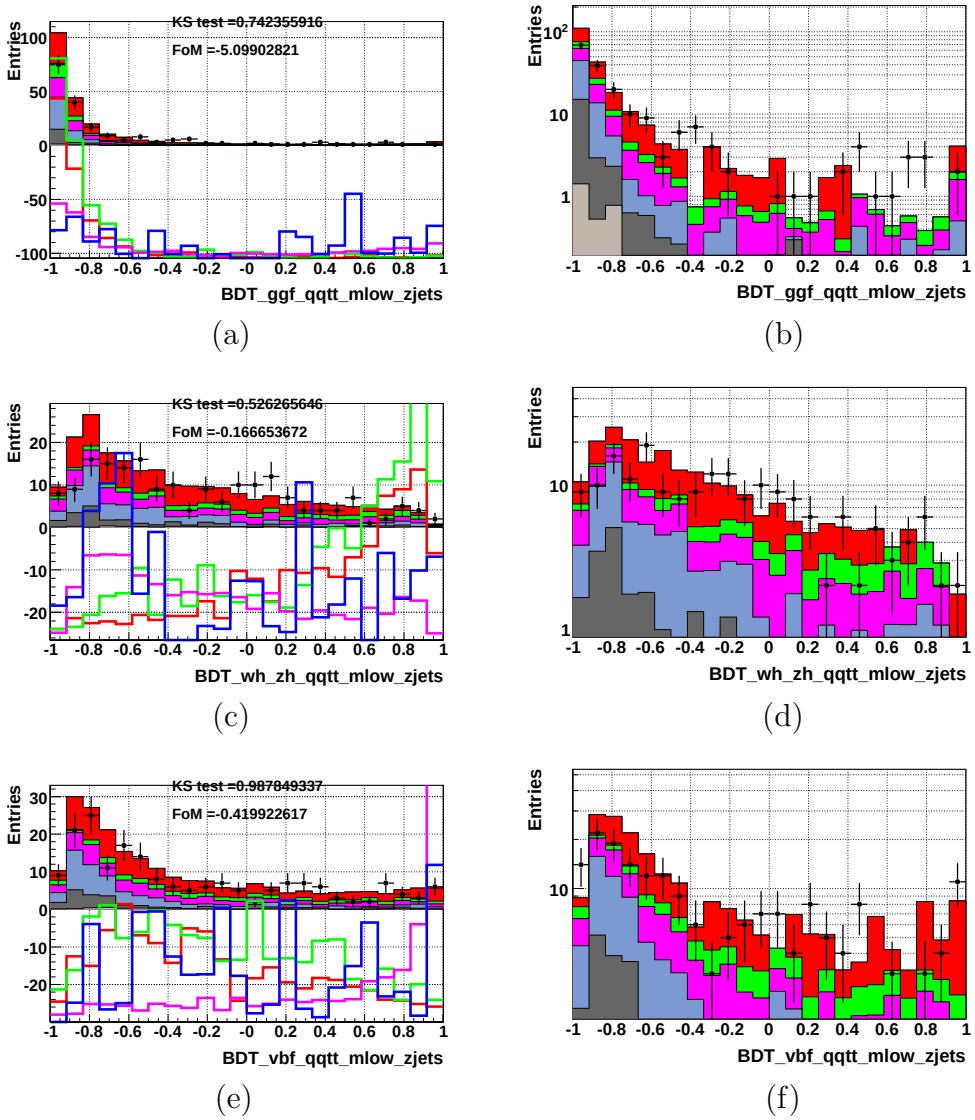

Figure 3.25: BDT outputs for low Higgs mass, trained between the $Z + jets$ background and the signals (a), (b) $GGF_{\tau\tau}$, (c), (d) $VH_{\tau\tau}$, and (e), (f) $VBF_{\tau\tau}$. The linear outputs are on the left and the log outputs are on the right.

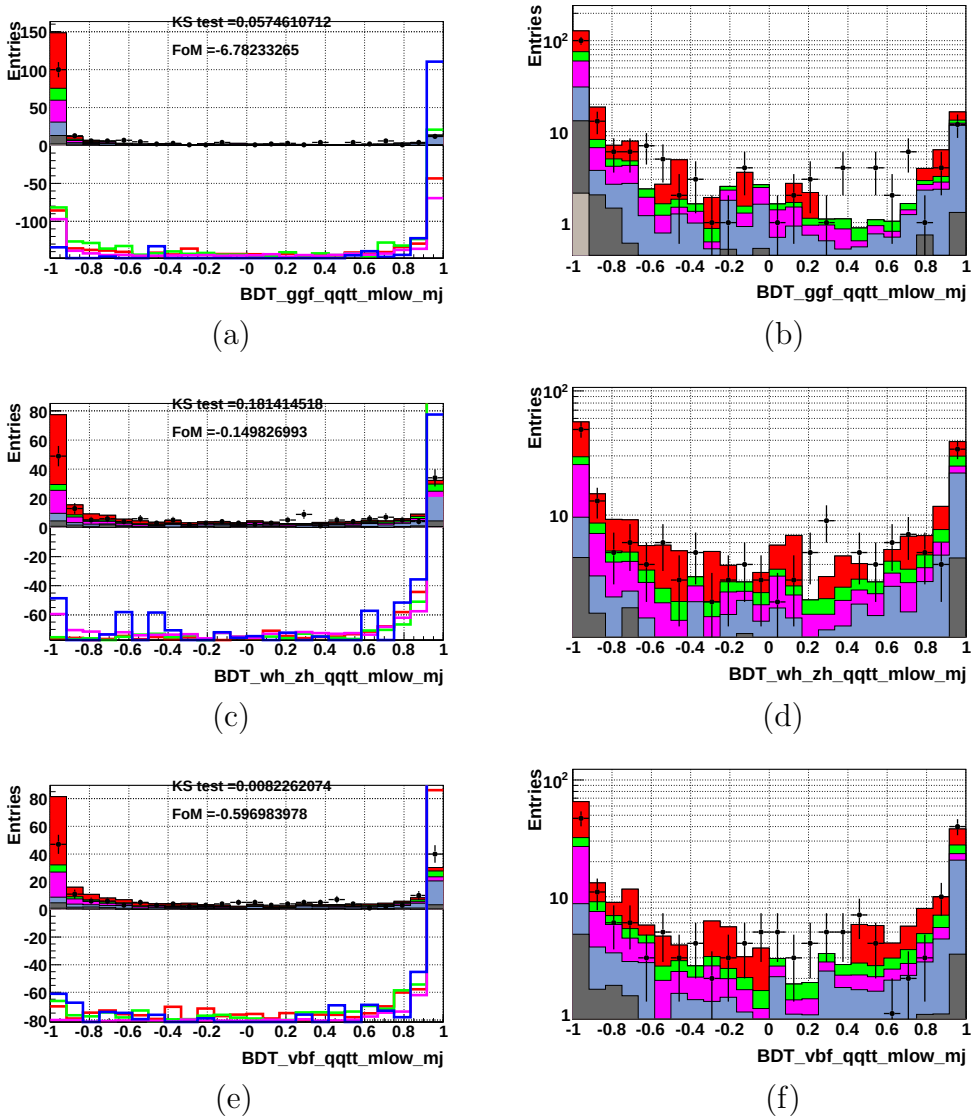

Figure 3.26: BDT outputs for low Higgs mass, trained between the multijet background and the signals (a), (b) $GGF_{\tau\tau}$, (c), (d) $VH_{\tau\tau}$, and (e), (f) $VBF_{\tau\tau}$. The linear outputs are on the left and the log outputs are on the right.

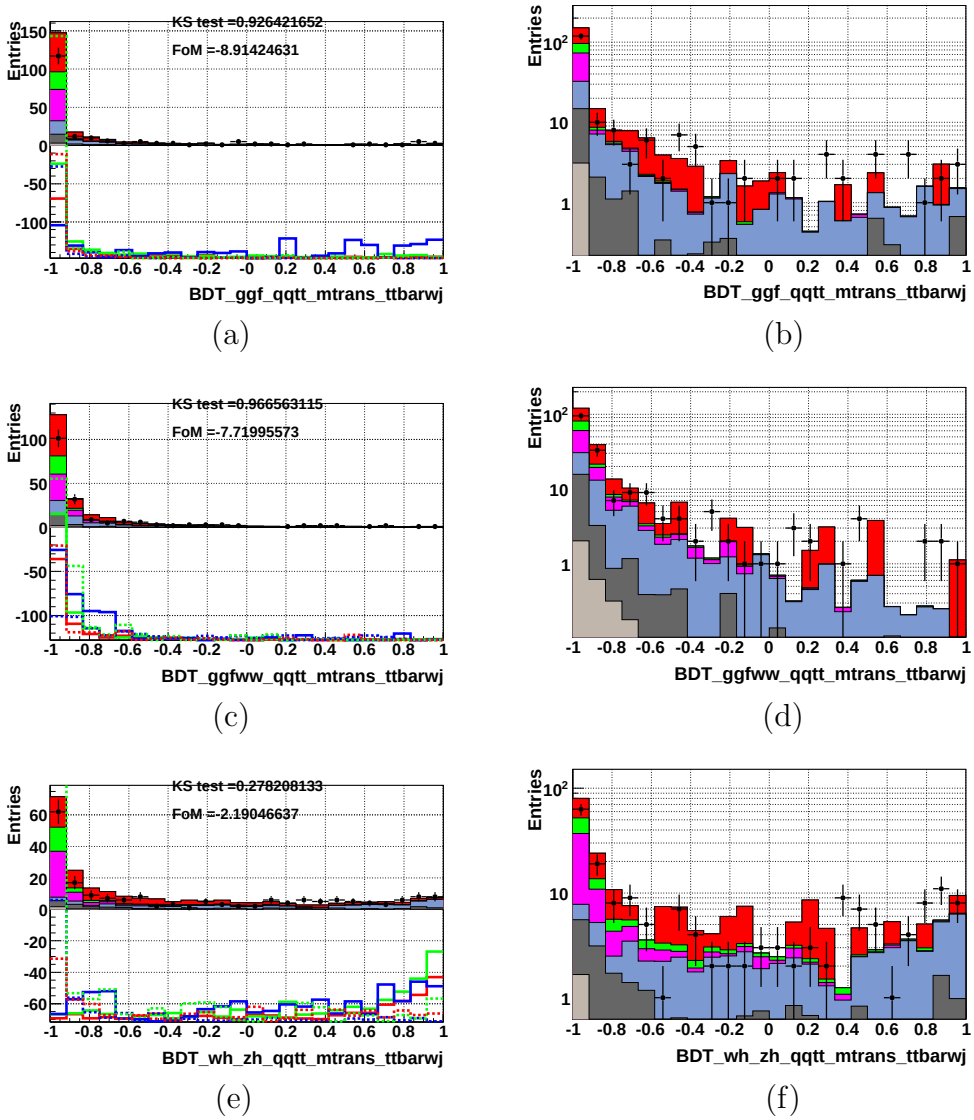

Figure 3.27: BDT outputs for intermediate Higgs mass, trained between the $t\bar{t}$ and $W + jets$ backgrounds and the signals (a), (b) $\mathrm{GGF}_{\tau\tau}$, (c), (d) GGF_{WW}, (e), (f) $\mathrm{VH}_{\tau\tau}$. The linear outputs are on the left and the log outputs are on the right.

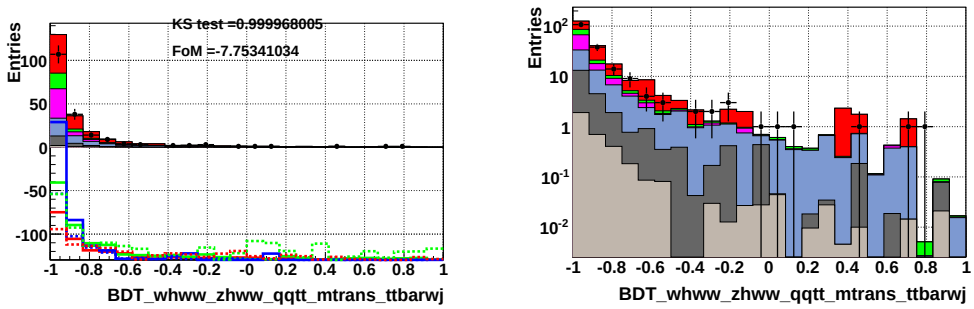

(a)

(b)

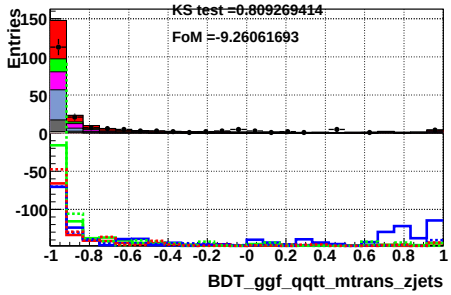

(c)

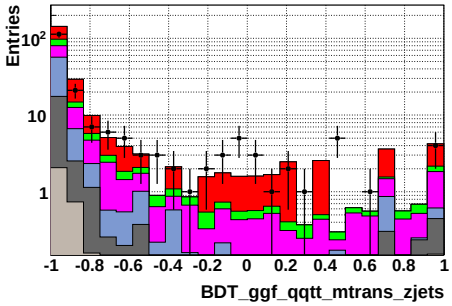

(d)

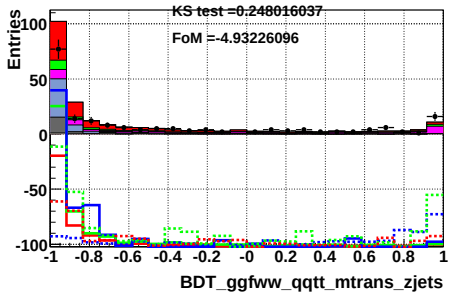

(e)

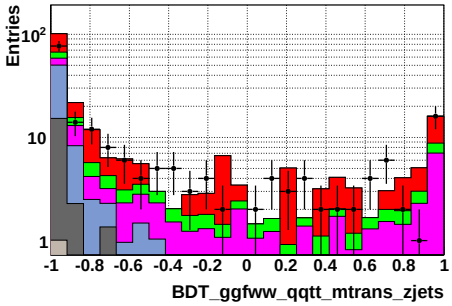

(f)

Figure 3.28: BDT outputs for intermediate Higgs mass, trained between the $t\bar{t}$ and $W + jets$ backgrounds and the signal (a), (b) VH_{WW}, and between the $Z + jets$ background and the signals (c), (d) $\mathrm{GGF}_{\tau\tau}$, and (e), (f) GGF_{WW}. The linear outputs are on the left and the log outputs are on the right.

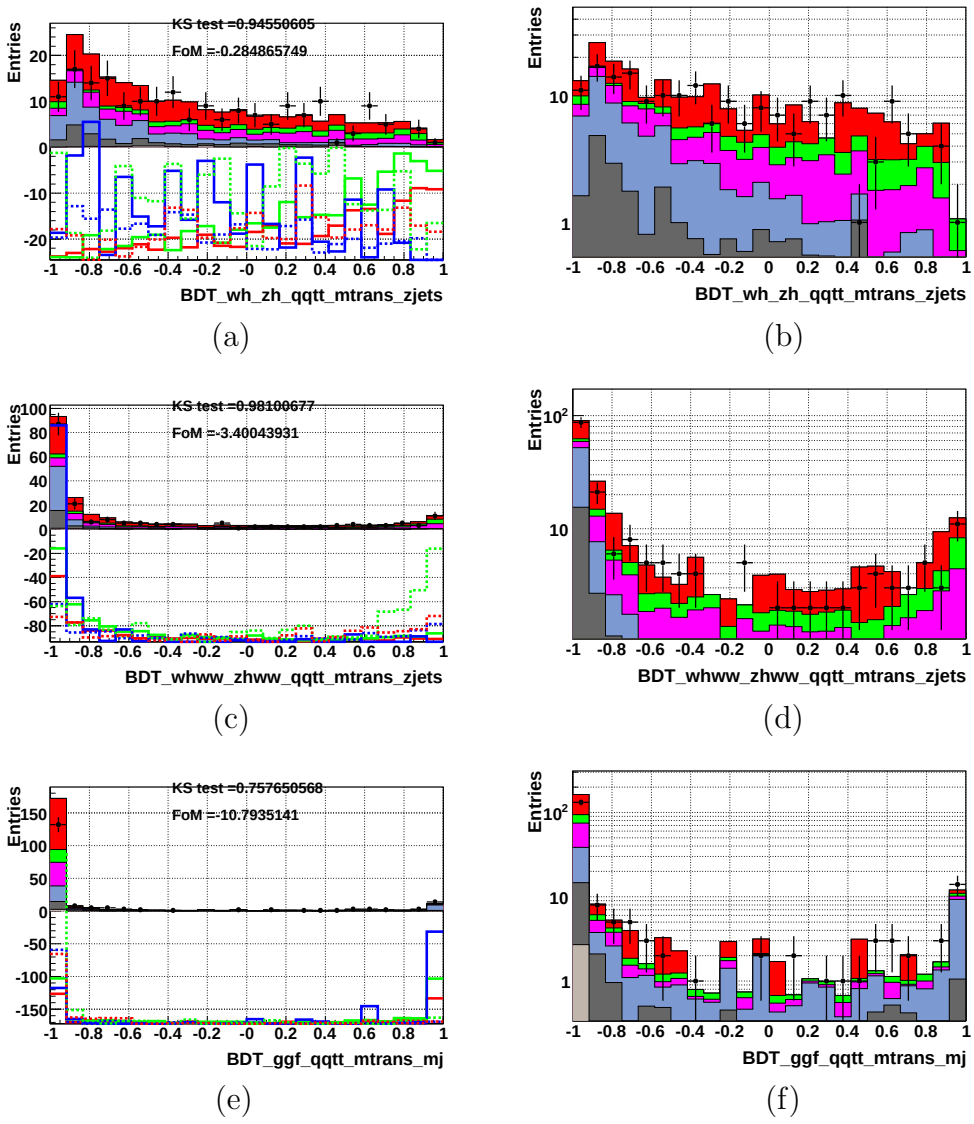

Figure 3.29: BDT outputs for intermediate Higgs mass, trained between the $Z + jets$ background and the signals (a), (b) $\mathrm{VH}_{\tau\tau}$ and (c), (d) VH_{WW}, and between the multijet background and the signal (e), (f) $\mathrm{GGF}_{\tau\tau}$. The linear outputs are on the left and the log outputs are on the right.

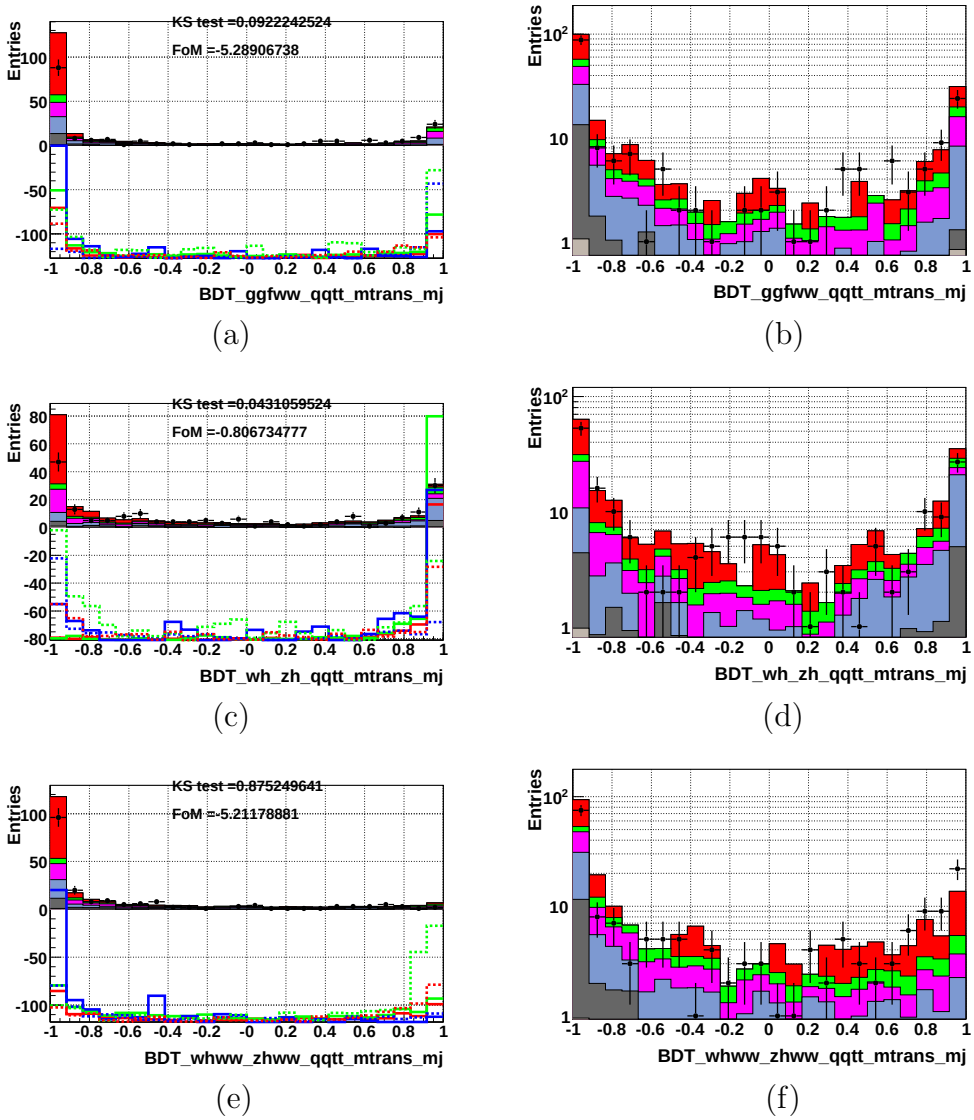

Figure 3.30: BDT outputs for intermediate Higgs mass, trained between the multi-jet background and the signals (a), (b) GGF_{WW}, (c), (d) $\mathrm{VH}_{\tau\tau}$, and (e), (f) VH_{WW}. The linear outputs are on the left and the log outputs are on the right.

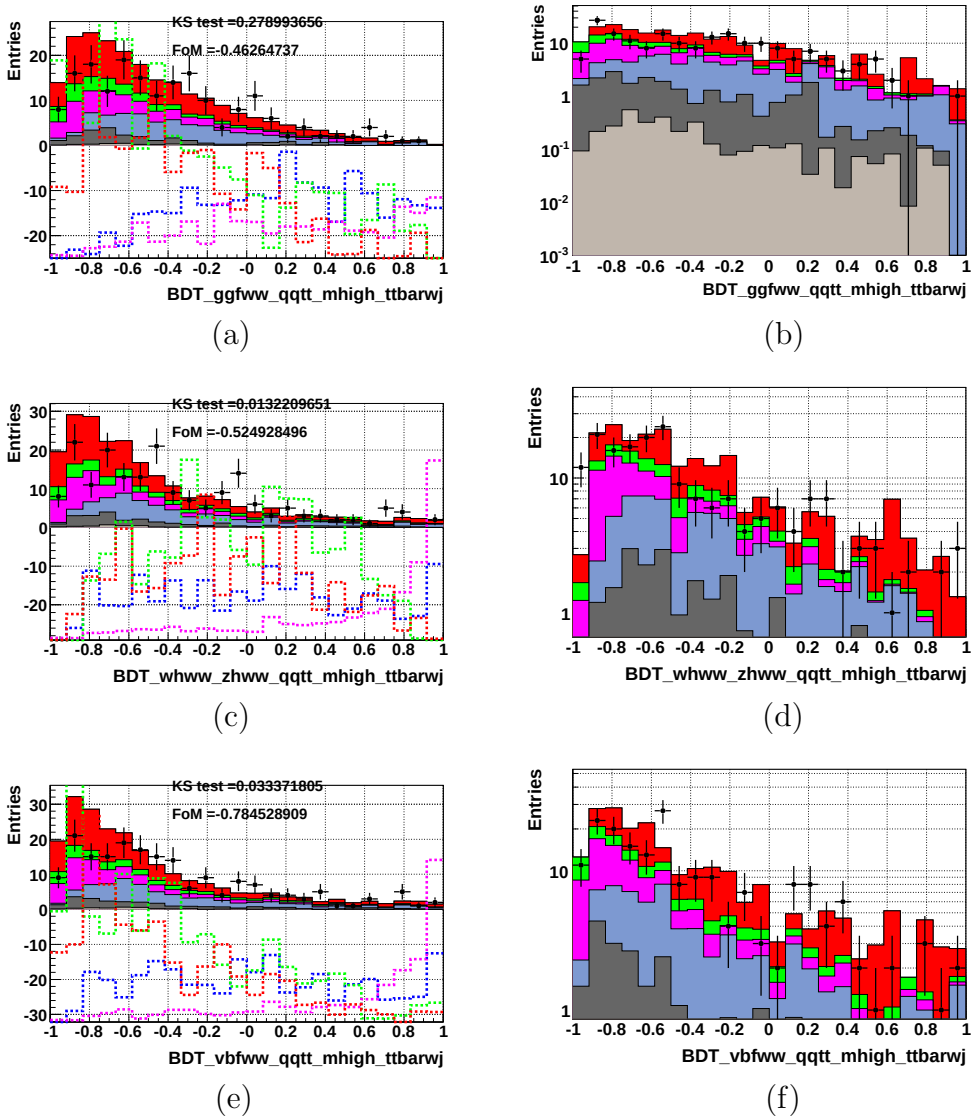

Figure 3.31: BDT outputs for high Higgs mass, trained between the $t\bar{t}$ and $W + jets$ backgrounds and the signals (a), (b) GGF_{WW}, (c), (d) VH_{WW}, and (e), (f) VBF_{WW}. The linear outputs are on the left and the log outputs are on the right.

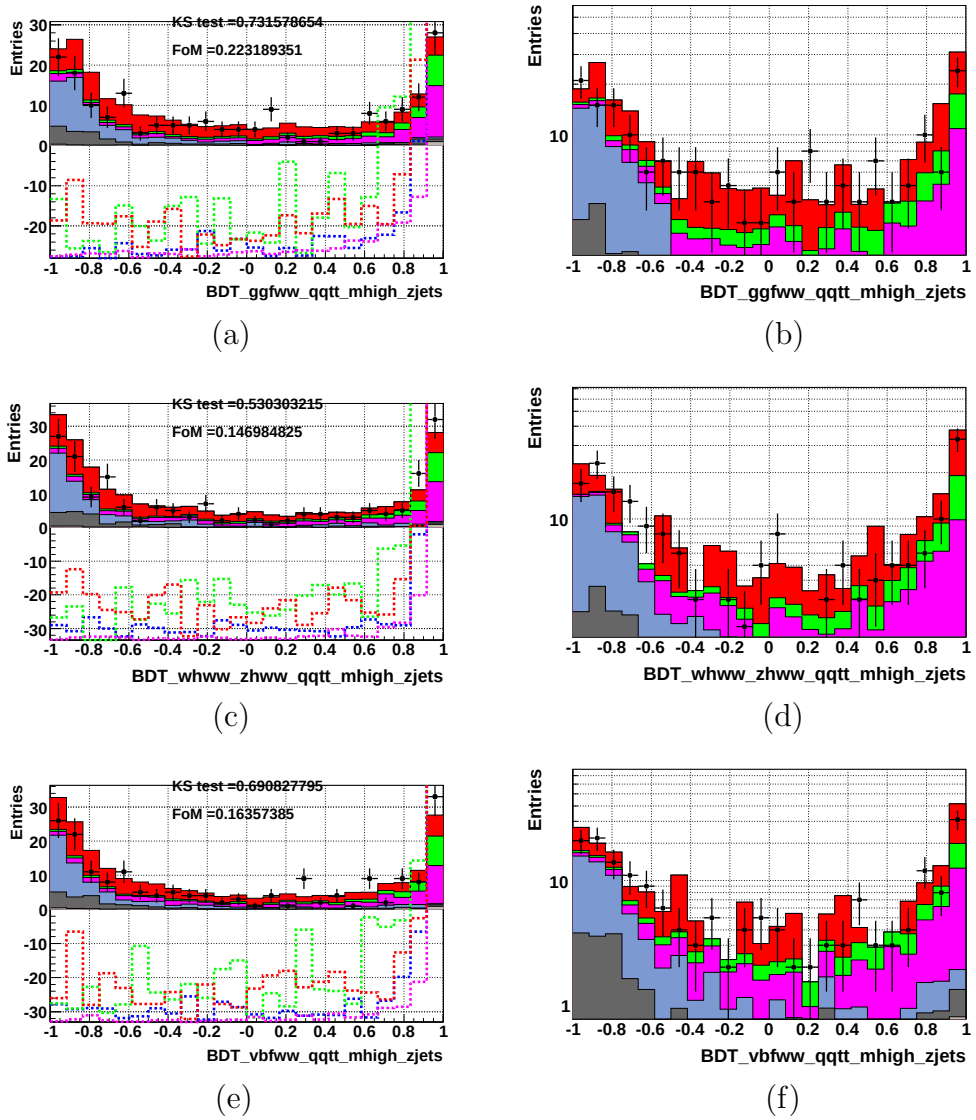

Figure 3.32: BDT outputs for high Higgs mass, trained between the $Z + jets$ background and the signals (a), (b) GGF_{WW}, (c), (d) VH_{WW}, and (e), (f) VBF_{WW}. The linear outputs are on the left and the log outputs are on the right.

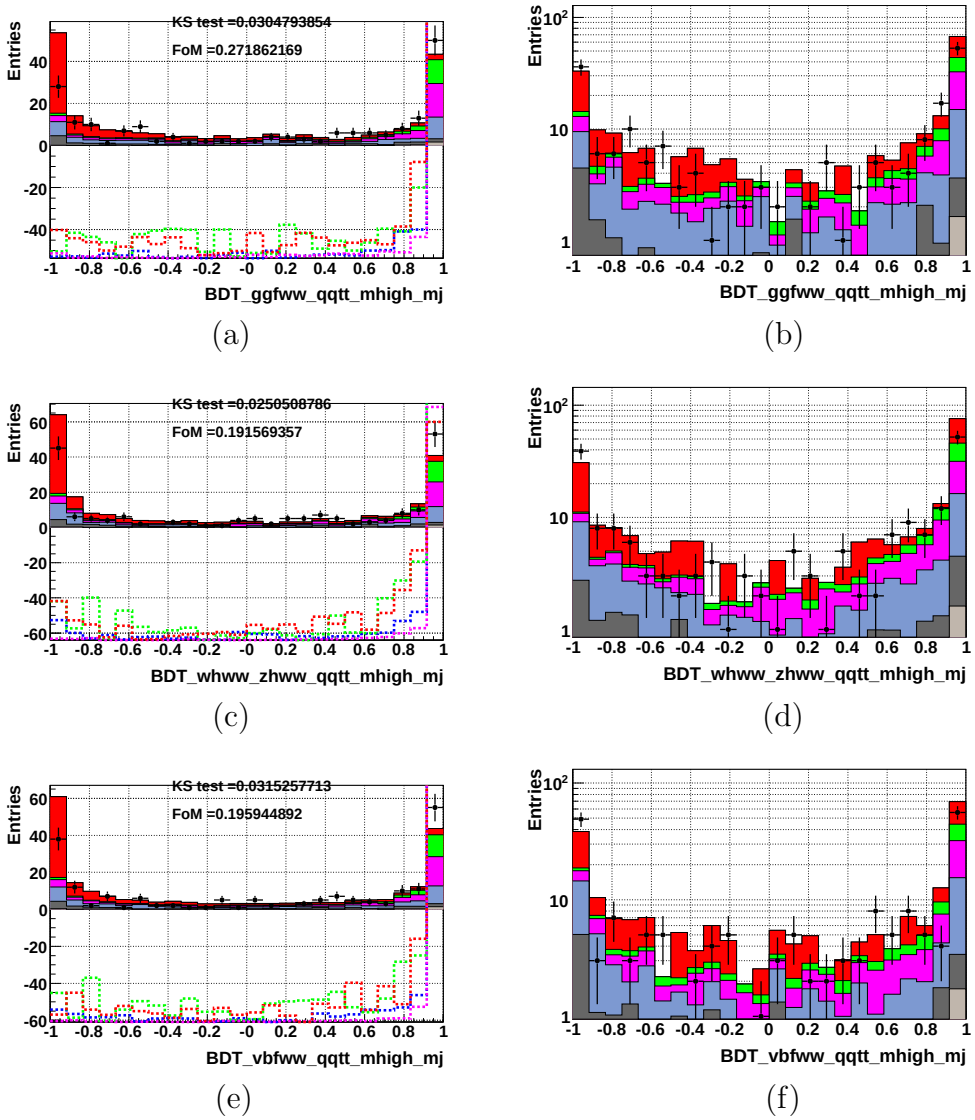

Figure 3.33: BDT outputs for high Higgs mass, trained between the multijet background and the signals (a), (b) GGF_{WW}, (c), (d) VH_{WW}, and (e), (f) VBF_{WW}. The linear outputs are on the left and the log outputs are on the right.

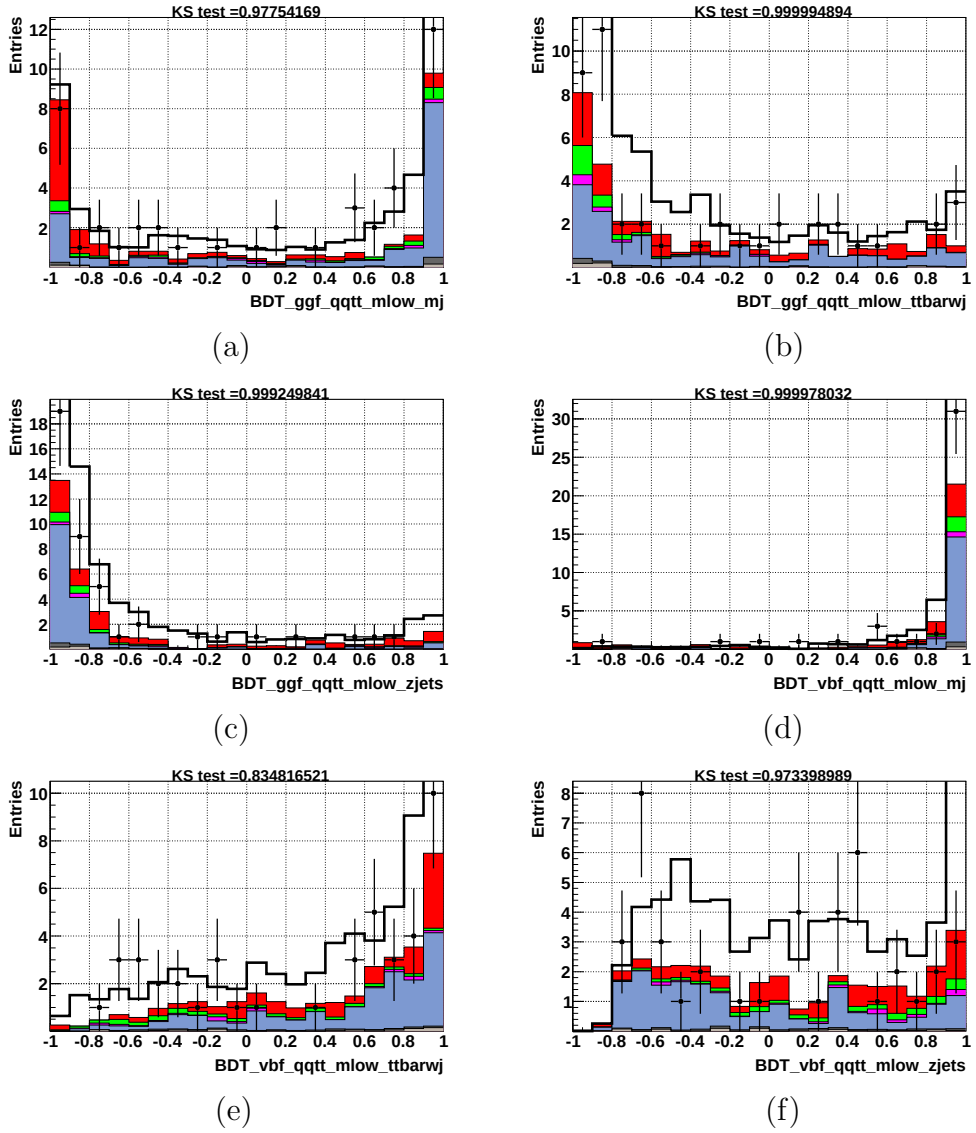

Figure 3.34: After a cut has been made requiring cBDT 0.4: BDT outputs for low Higgs mass, trained between the $\mathrm{GGF}_{\tau\tau}$ signal and (a) the MJ background, (b) $t\bar{t}$ and $W + jets$ backgrounds, (c) $Z + jets$ backgrounds, and between the $\mathrm{VBF}_{\tau\tau}$ signal and (d) the MJ background, (e) $t\bar{t}$ and $W + jets$ backgrounds, (f) $Z + jets$ backgrounds. Ideally the background trained against should not be in the signal region. The $\mathrm{VBF}_{\tau\tau}$ vs. MJ BDT is seen as especially unhelpful as an input to the cBDT. The black line is the sum of all signals, multiplied by 500.

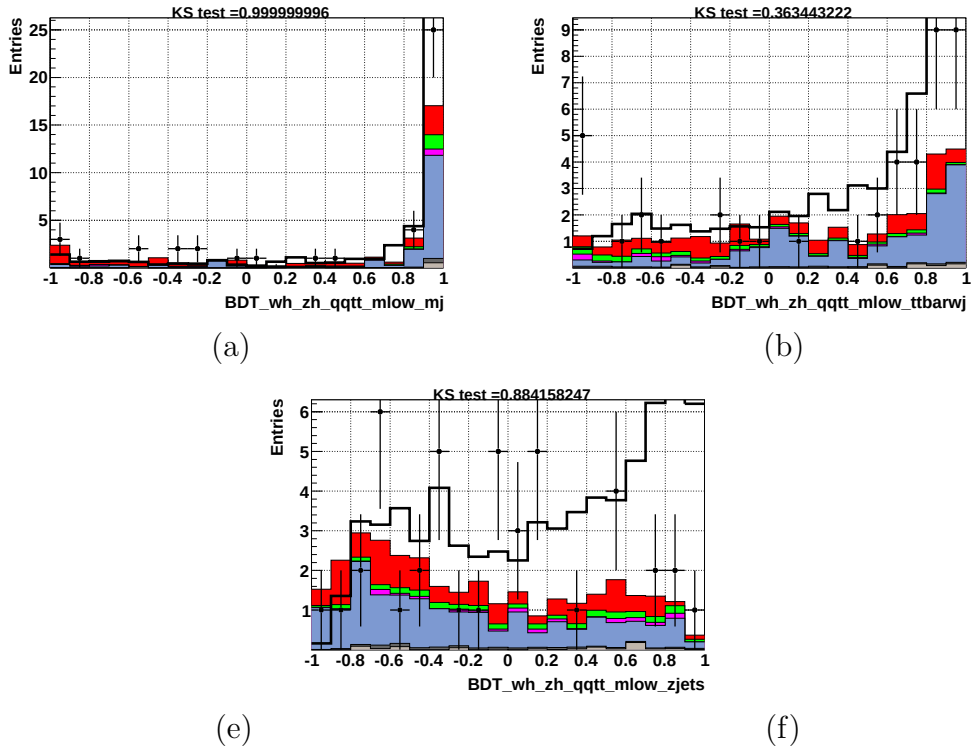

Figure 3.35: After a cut has been made requiring cBDT>0.4: BDT outputs for low Higgs mass, trained between the $VH_{\tau\tau}$ signal and (a) the MJ background, (b) $t\bar{t}$ and $W + jets$ backgrounds, (c) $Z + jets$ backgrounds. The $VH_{\tau\tau}$ vs. MJ BDT is seen as especially unhelpful as an input to the cBDT, since so much of the MJ is left at the signal side.

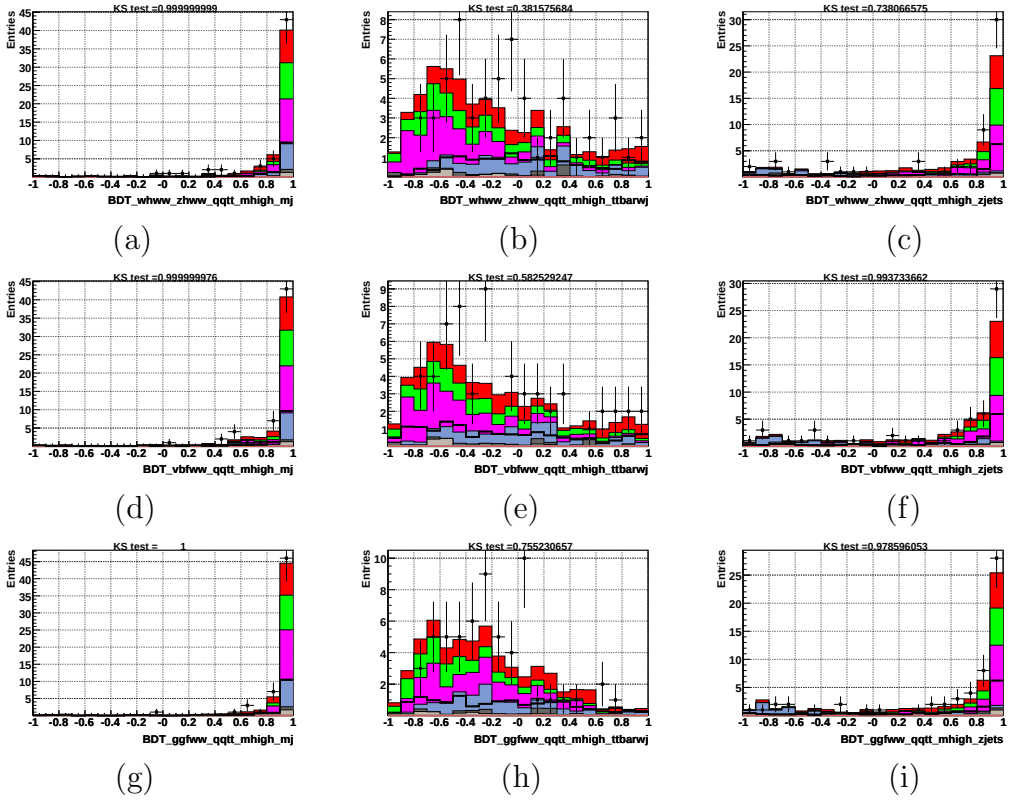

Figure 3.36: After a cut has been made requiring cBDT>0.4: BDT outputs for high Higgs mass, trained between the VH_{WW} signal and (a) the MJ background, (b) $t\bar{t}$ and $W + jets$ backgrounds, (c) $Z + jets$ backgrounds; between the VBF_{WW} signal and (d) the MJ background, (d) $t\bar{t}$ and $W + jets$ backgrounds, (f) $Z + jets$ backgrounds; between the GGF_{WW} signal and (g) the MJ background, (h) $t\bar{t}$ and $W + jets$ backgrounds, (i) $Z + jets$ backgrounds.

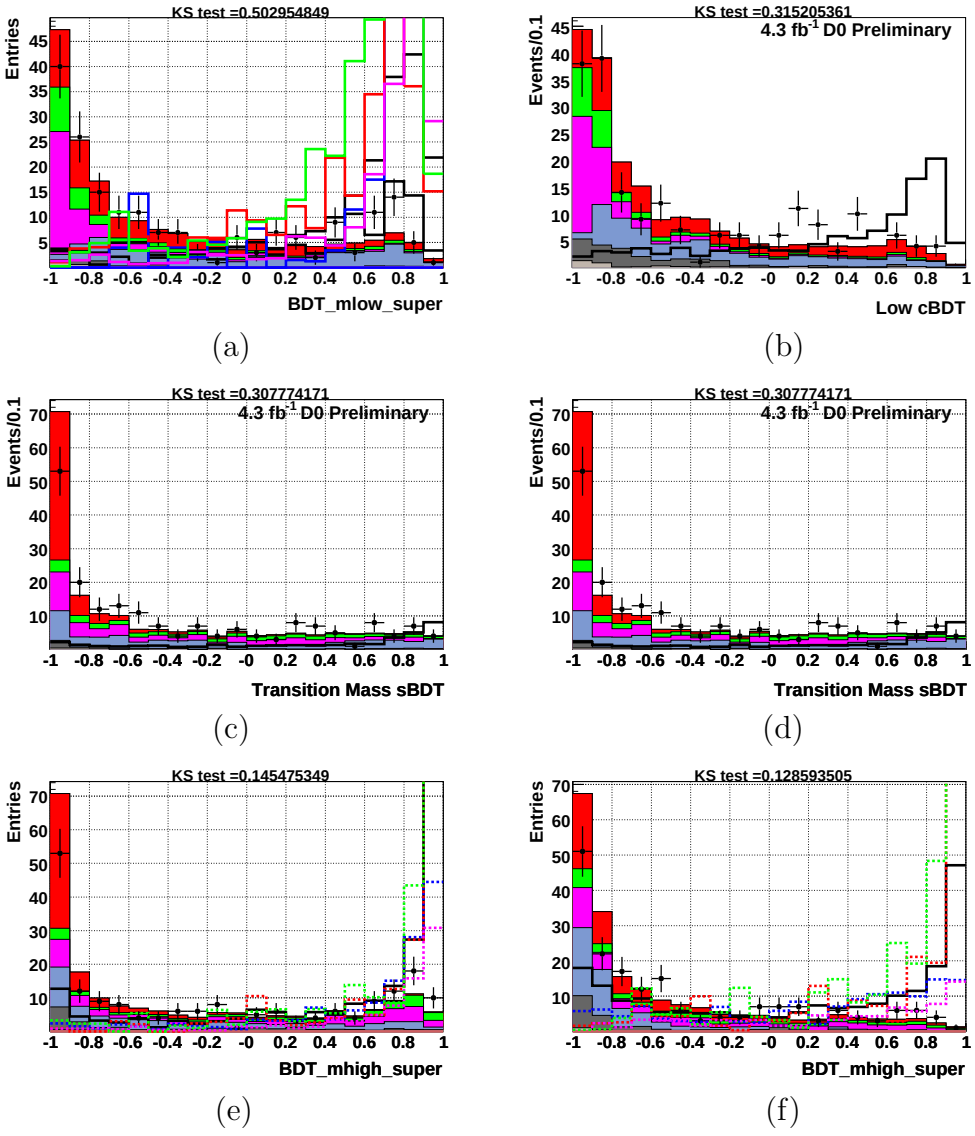

Figure 3.37: The combined BDTs made with all of the individual BDT inputs in the training on the left, and with the optimized inputs on the right.

3.8 Systematic Uncertainties

Experimental systematic uncertainties are evaluated for the sources listed in Table 3.12. In general each source of systematic uncertainty is varied by ± 1 standard deviation, propagated to the cBDT output, and compared to the central cBDT output. Some systematics are estimated with special control samples, and some are taken from standard DØ/Higgs Group determinations. All are described below. Sources which vary the shape of the cBDT distribution are noted in the table, and in these cases the shape variation is carried through to the limit setting. Those affecting only the normalization of the cBDT output are called "flat".

- The uncertainty on the integrated luminosity is considered to be flat with value of 6.1%. This uncertainty can be decomposed into a component of 4.1% that is unique to DØ and a 4.6% component owing to uncertainty in the luminosity cross section which is fully correlated with CDF.

- The uncertainty on the efficiencies of e ID, track match, and isolation is taken to be flat with value of 4% .

- The uncertainty on the electron trigger efficiency is taken to be flat with value of 2%.

- The cross section uncertainties are taken from the standard Tevatron TeVNPHWG and DØ Higgs group accords. A systematic uncertainty of 6% is used for the Higgs signal cross sections to account for possible differences among the several Higgs processes used in this analysis.

- The uncertainty associated with the vertex confirmation of jets is taken to be 4% on the final cBDT discriminant.

- The uncertainty due to the tau energy scale correction is considered to be flat and is taken as an average (weighted by our relative yields for different tau types) of the tau-type-specific uncertainties. The uncertainty is 9.8%.

- The uncertainty due to the tau track efficiency is taken to be flat with a value of 1.4%.

- The uncertainty for the tau selection, background subtraction and variations in efficiency with tau momentum is taken to be 6.5% taken from the weighted average over tau types, (21%, 3.5% and 8.5%) respectively for tau types (1, 2, 3).

- The uncertainty due to the PDFs is obtained from the CTEQ6L1 LHPDF eigenvector set, and is applied as a shape independent uncertainty. At present this uncertainty is taken at 2% for all signals and backgrounds except the $t\bar{t}$ background for which we take 6%.

In the case of the systematics listed below, statistical fluctuations in shape distributions led to problems when using the uncertainties in the final limit setting. To smooth the shapes we fit them to functions (a combination of exponentials and polynomials) and then filled them with higher statistics. This is done separately for the central value and $\pm\sigma$ variations, and for $Z + jets$, $t\bar{t}$, $W + jets$, MJ backgrounds, and combined signals. (The diboson background is a very small contribution and the shape systematics are not rederived on that sample.) An example of the fitting is shown in Figure 3.38. The other shape systematics are shown in the appendix.

- The uncertainty due to the jet-id and jet reconstruction efficiency is estimated by varying the jet-ID scale factors by $\pm 1\sigma$. The scale factors are varied in the same way for the uncertainty due to the jet energy resolution (JER) and the jet energy scale (JES). Figures A.1 through A.3 in Appendix X show the overlaid and fractional comparisons of the cBDT distributions between the nominal and shifted efficiencies for signal and $Z+$ jets, $W+$ jets and $t\bar{t}$ backgrounds.

- Two alternate MJ enriched samples were studied to calculate a MJ background uncertainty; these are described in Section 3.5 and generally involve alternately taking a low NN τ and a loosely selected e. We recalculate the cBDT for all three cases. For the case in which the low NN τ and tight electron is used, the shape variation from the normal MJ sample is tiny. We therefore decided to take the positive and negative difference between the normal and the high NN τ- loose e sample as the systematics on the MJ. The positive and negative differences from the nominal are shown in the appendix in Figure A.1 (d).

- The systematic uncertainty on the MJ normalizations is taken to be the uncertainty on the scale factors ρ obtained from the nominal baseline sample (Table 3.5), weighted by the tau type fractions.

3.9 Limits

We use a modified frequentist method to calculate confidence level limits with the program *Collie*, which is described in some detail in this reference:

Source	type	Uncertainty (%)
Luminosity (DØ specific)	flat	4.1
Luminosity (Tevatron common)	flat	4.6
e ID, track match, iso.	flat	4
e trigger	flat	2
τ energy correction	flat	9.8
τ track efficiency	flat	1.4
τ selection by type	flat	12, 4.2, 7
W/Z+light flavor XS	flat	6.0
$t\bar{t}$, single top XS	flat	10.0
jet vetex confirmation	flat	4.0
diboson XS	flat	7.0
VH signal XS	flat	6.2
VBF signal XS	flat	4.9
GGF signal XS PDF	flat	29
GGF signal XS normalization	flat	33
$GGF^{H}_{p_T}$	shape	1.0
Jet ID/reco eff.	shape	≈ 20
Jet E resolution.	shape	≈ 10
JES	shape	≈ 15
jet p_T	flat	5.5
PDF	shape	2 - 6
MJ normalization	flat	4.7
MJ shape	shape	15 - 20

Table 3.12: Systematic uncertainties (in percent) on the final cBDT.

[22]. This method creates pseudo experiments for a background-only scenario and a signal-plus-background scenario. The pseudo experiment results are then compared to the expected signal and background in a likelihood, derived from a hypothesis significance:

$$Q(\overrightarrow{s}, \overrightarrow{b}, \overrightarrow{d}) = \prod_{i=0}^{N_C} \prod_{j=0}^{N_{bins}} \frac{(s+b)_{ij}^{d_{ij}} e^{-(s+b)_{ij}}}{d_{ij}!} / \frac{b_{ij}^{d_{ij}} e^{-b_{ij}}}{d_{ij}!} \tag{3.12}$$

$$LLR(\overrightarrow{s}, \overrightarrow{b}, \overrightarrow{d}) = -2\log(Q) = \sum_{i=0}^{N_C} \sum_{j=0}^{N_{bins}} s_{ij} - d_{ij} \ln(1 + \frac{s_{ij}}{b_{ij}}) \tag{3.13}$$

where $\overrightarrow{s}$ is the set of signal estimations, $\overrightarrow{b}$ is the set of background estimations, $\overrightarrow{d}$ is the result of a particular pseudo experiment, N_C is the number of signal channels being added together, and N_{bins} is the number of bins in the final discriminant. The final discriminant used here is the cBDT. The $e\tau jj$ analysis combines the 9 signals before calculating the limit so N_C is one, but when combining the $e\tau jj$ and $\mu\tau jj$ analyses N_C is two. Systematics are included in the limit as follows: the hypothesis prediction is varied within the systematic uncertainties and a minimization is performed to give the best fit of the prediction to the data (the fit includes weight penalties which are a function of the deviation of the hypothesis from nominal). For example a 4.1%

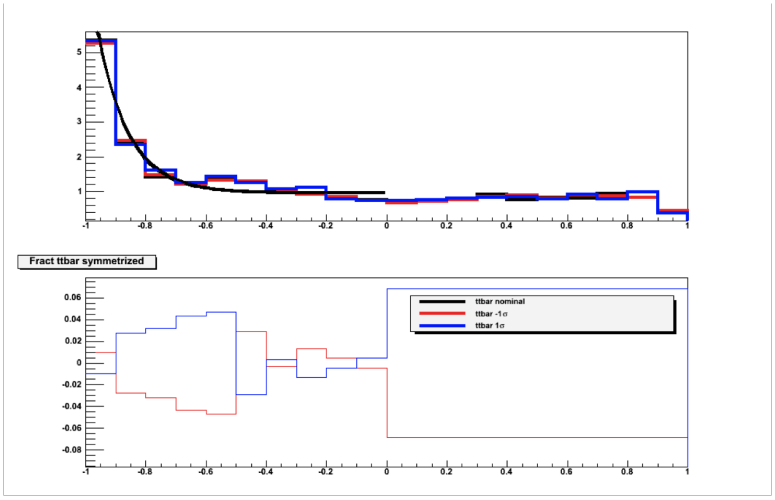

Figure 3.38: Fit to the variation in $t\bar{t}$ background due to varying the JES by ± one standard deviation.

systematic on Luminosity means the Luminosity according to a Gaussian with $\sigma = 4.1\%$ and the best fit value in that range is found.

Figure 3.39 shows an example of the LLR distribution for the signal + background and background-only pseudo experiments and for the data (this is only an example, not the tautaujj data). If the data (here the black vertical line) was in agreement with the background-only scenario it's LLR would fall in the middle of the background-only curve (green), and if the data agreed with the signal+background scenario it would fall at the peak of the (red) signal+background curve (assuming perfect modeling). We would like to plot the LLR versus the Higgs mass; an example of how the $\pm\sigma$ bands are carried into this plot is shown in Figure 3.40. The LLR plot versus Higgs mass for the $e\tau jj$ data and background estimation is shown in Fig. 3.41.

As the data LLR usually falls somewhere between the background-only and signal+background LLR curves (due to imperfect modeling), we would like a quantity to designate how signal-like and how background-like it is. We use Confidence Levels (CL), where, CL_{s+b} is defined as the fraction of signal+background pseudo experiments less signal-like than data, and CL_b, as the fraction of the background-only pseudo experiments less signal-like than data. A purely Frequentist approach to confidence levels would use CL_{s+b} as the figure of merit. In order to make the quantity more robust to possible background mismodeling, we use,

$$CL_s = \frac{CL_{s+b}}{CL_b} \tag{3.14}$$

Since we do not see evidence for the Higgs, we use (1 - CL_s), as the confidence level that the Higgs does not exist. If we were to see a value of (1-CL_s) greater than 95% we would say that the Higgs most likely does not exist. (There would be a 5% chance that, due to random fluctuations, the Higgs was not observed but does exist.) In the tautaujj channel the (1- CL_s) is less than 95%. We calculate how much the predicted signal would have to be inflated in order for us to say that our data rules out the signal at 95%. This is listed in Table 3.13. The CLfit2 limits include systematics, but the CLfast limits do not (they are done as a check before the CLfit2). At a Higgs mass of 115 GeV, if the Higgs cross section were 32.8 times higher, we could say our data ruled out the Higgs at 95% confidence level. The expected limit listed is from our prediction of signal+background. These values are plotted in Figure 3.42.

The results from the $e\tau jj$ analysis are combined with the results from the $\mu\tau jj$ analysis in Figures 3.44 and 3.43.

In preparation for the 2011 Winter physics conferences the results from the current Higgs searches at the Tevatron were combined to create one exclusion

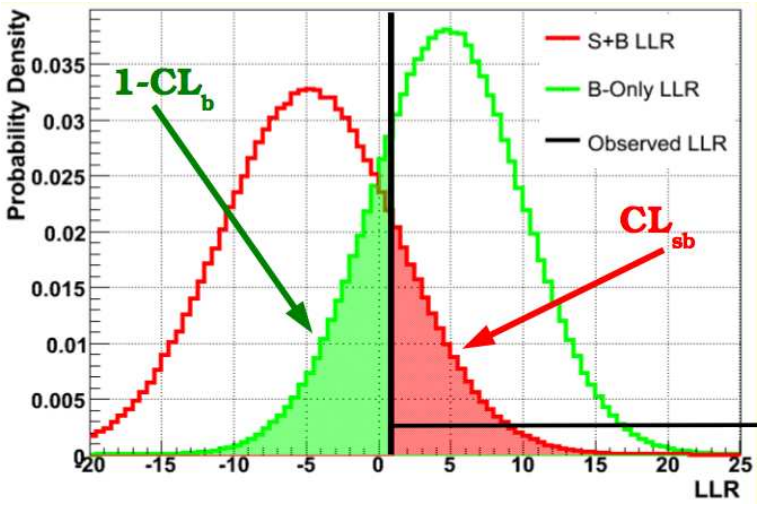

Figure 3.39: Sample distributions of the LogLikelihood for signal+ background (red) and background-only (green) scenario pseudo experiments. If data gives the LLR shown by the black horizontal line then CL_{s+b} and CL_b can be defined as the integrals under the curves take from the data line out to higher LLR.

limit. This combined limit is shown in Figure 3.45.

3.10 Conclusions

Results from the DØ Standard Model Higgs boson search in the final state $\tau\tau jetjet$ are presented. No evidence for the Higgs is yet seen so limits are placed on its existence as a function of Higgs mass. For a Higgs mass of 115 GeV (165 GeV) the ratio of the observed limit to the Standard Model expectation is 34.0 (55.2). When this search is combined with other Higgs searches at the Tevatron, the existence of a Higgs with mass between 158 and 173 GeV is ruled out at the 95% confidence level.

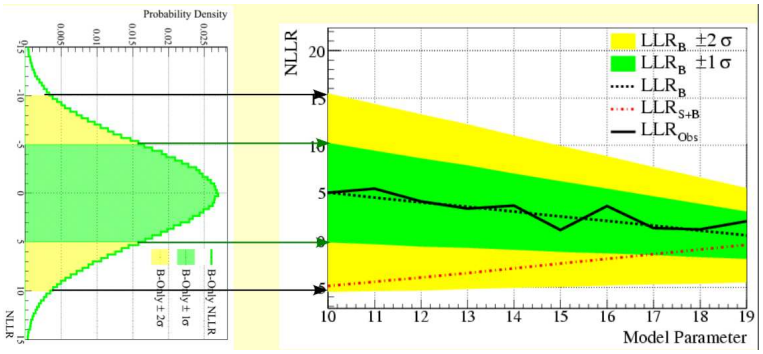

Figure 3.40: An example to show how the 1 and 2 σ error bands are translated from LLR distributions to LLR versus model parameter plots (our model parameter is the Higgs mass).

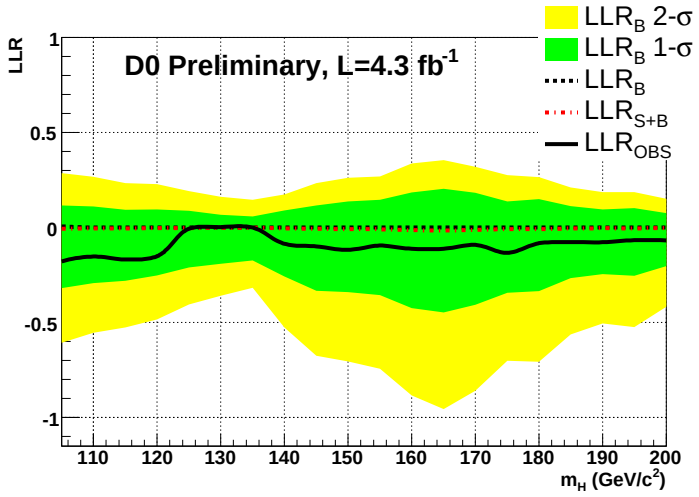

Figure 3.41: LLR as a function of Higgs mass, for expected background only (black dotted line), expected with signal + background (red dotted line) hypotheses, and the observed values (solid black line). The ± 1 and $\pm 2\sigma$ variations from the expected background only hypothesis are shown in green and yellow bands respectively.

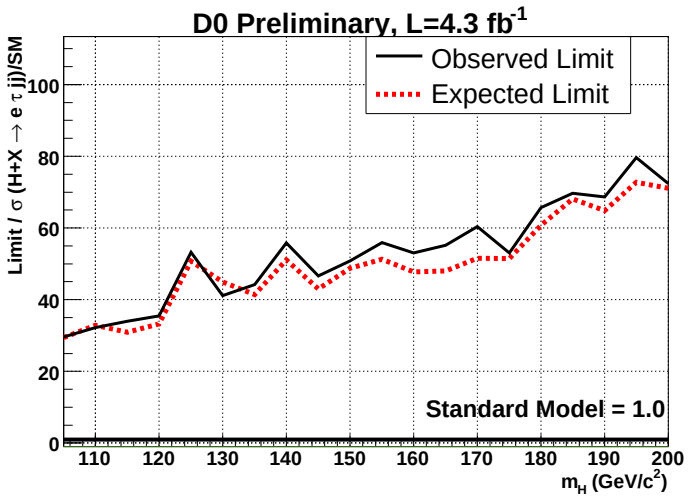

Figure 3.42: The inflated cross section of the Higgs which we would be able to rule out at the 95% confidence level divided by the Standard Model cross section. OR: Ratio of our 95% confidence level to the Standard Model. The $e\tau jj$ channel alone is sensitive to a Higgs cross section 32 times the Standard Model at $m_H = 115$ GeV.

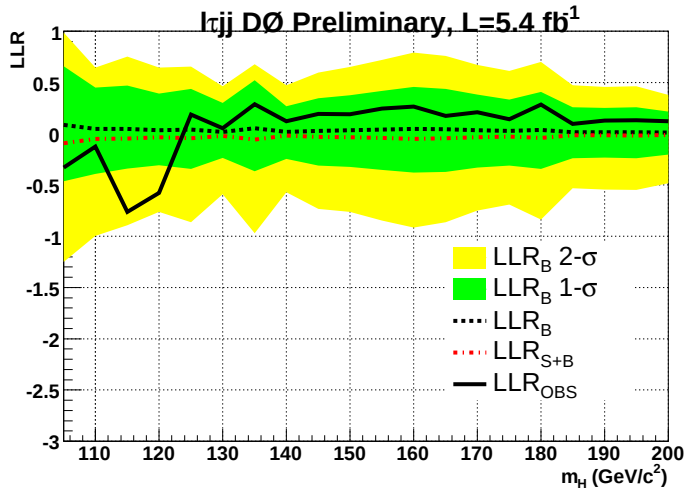

Figure 3.43: LogLikelihood ratio verse Higgs mass for the $e\tau jj$ and $\mu\tau jj$ searches combined.

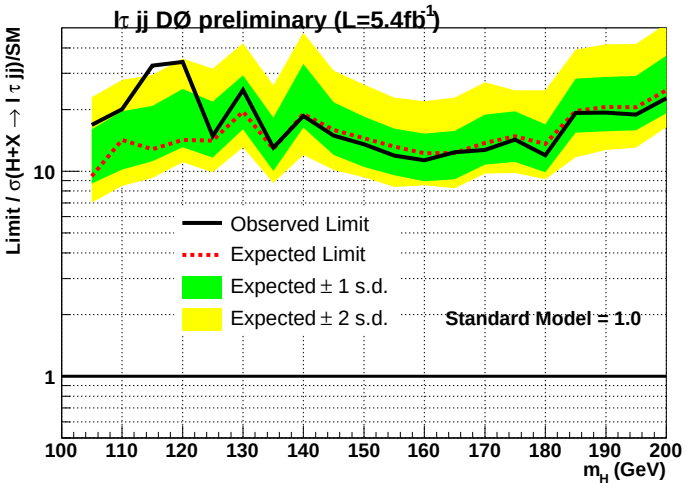

Figure 3.44: The ratio of the limits to the Standard Model Higgs cross section for the $e\tau jj$ and $\mu\tau jj$ searches combined.

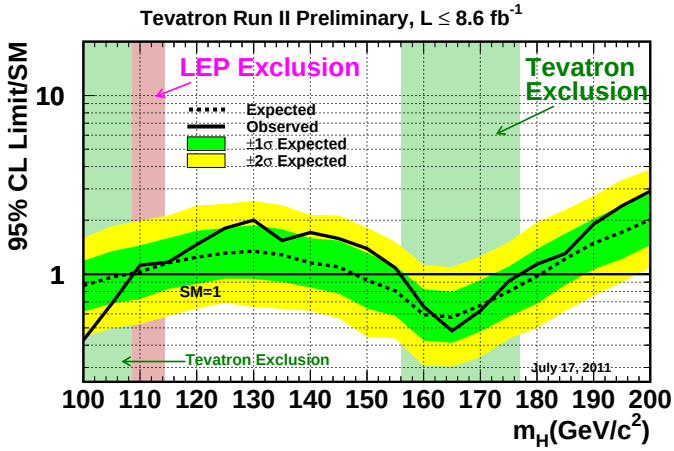

Figure 3.45: The ratio of the limits to the Standard Model Higgs cross section versus Higgs mass for all the Tevatron Higgs searches combined. The Standard Model Higgs boson is excluded at a 95% confidence level for a Higgs mass between 156 and 177 GeV.

	CLfast		CLfit2	
Higgs mass	exp.	obs.	exp.	obs.
105	27.2	36.4	29.4	29.6
110	29.7	38.5	32.2	32.2
115	31.3	43.9	34.0	34.0
120	34.3	47.8	35.4	35.4
125	39.7	54.4	53.2	53.2
130	42.2	58.4	41.1	41.1
135	44.0	62.7	44.2	44.2
140	39.1	50.0	55.8	55.8
145	31.9	40.0	46.7	46.7
150	29.6	41.2	50.8	50.8
155	29.3	39.7	56.0	56.0
160	24.7	32.2	43.0	53.1
165	22.4	30.9	48.8	55.2
170	25.9	33.3	51.5	60.4
175	30.2	42.8	51.5	53.1
180	31.3	40.6	60.7	65.7
185	39.2	52.7	68.1	69.6
190	43.1	60.2	64.9	68.7
195	42.4	57.9	72.7	79.6
200	52.6	74.2	71.0	72.4

Table 3.13: The ratio of the expected and observed 95% C.L. limits to the SM expectations.

Part III

Calorimeter Calibration at ATLAS

Chapter 4

Zee Calibration at ATLAS

This section gives a brief introduction and overview of the ATLAS Zee Calibration of the LAr electromagnetic calorimeter. Section 2 of the appendix has a copy of the note on Zee calibration published in 2008 here: [25]. The note gives the details of the calibration and how it was tested with monte carlo simulations.

Figure 4.2 shows a diagram of one section of the EM calorimeter. It is divided radially into three layers, increasing in width moving away from the beam line. The Zee calibration is designed to correct for long range variations in energy response in the EM calorimeter. In this case "long range" means variations over ranges of the order of $\Delta\eta$ x $\Delta\phi = 0.2$ x 0.4. (There are 400 regions of this size in the calorimeter.) The calibration uses electrons from Z decay to intercalibrate the regions. In general electrons from Z's will pass through two separate regions of the calorimeter, and it is easy to see that the sum of the energy of the two regions can be calibrated to the known Z mass. With enough statistics, the energy of each individual region can be calibrated. The details are described in the appendix.

The Zee calibration is now being applied at ATLAS with calibration factors derived from the 2010 data ($\sqrt{s} = 7$ TeV). The data taking periods called A through I were used, which makes up about 39 pb^{-1} of data. About 14,000 Zee events passed electron cuts used for the calibration. Some changes have been made since the plan outlined in the note. The statistics from the 2010 data set are not high enough to allow the calibration to be done in bins of $\Delta\eta$ x $\Delta\phi = 0.2$ x 0.4 because there are too few electrons in each region. The current calibration uses just 58 bins which are only a function of η. In the 2008 note we used Z line shape derived from a Breit-Wigner distribution, but the current calibration uses the full reconstructed monte carlo $Z \rightarrow ee$ peak, which takes into account both effects from theory (Breit-Wigner shape, γ contribution, $Z-\gamma$ interference, parton density function, final state radiation)

and experimental effects (detector resolution, effect of bremsstrahlung). Also, the note included the calorimeter barrel and end caps, but did not deal with the forward calorimeter. The forward calorimeter is now included out to $|\eta|$ <4.9.

Figure 4.3 shows the results from the calibration derived with 2010 data. Corrections are applied at the (0.025 x 0.0245) cell level in the calorimeter (see Fig. 4.2), according to

$$E_{calibrated} = E_{original}\frac{1}{(1+\alpha)}. \tag{4.1}$$

The binning in Fig. 4.3 was chosen to optimize the energy resolution after the correction factors are applied. In the barrel calorimeter ($|\eta| < 1.37$) the correction factors are on the order of $\approx \pm$ 1%; in the end caps ($1.52 < |\eta| < 2.47$) it is $\approx \pm$ 2%; in the forward calorimeter ($|\eta| > 2.4$) the corrections are larger, on the order of $\approx \pm$ 5%.

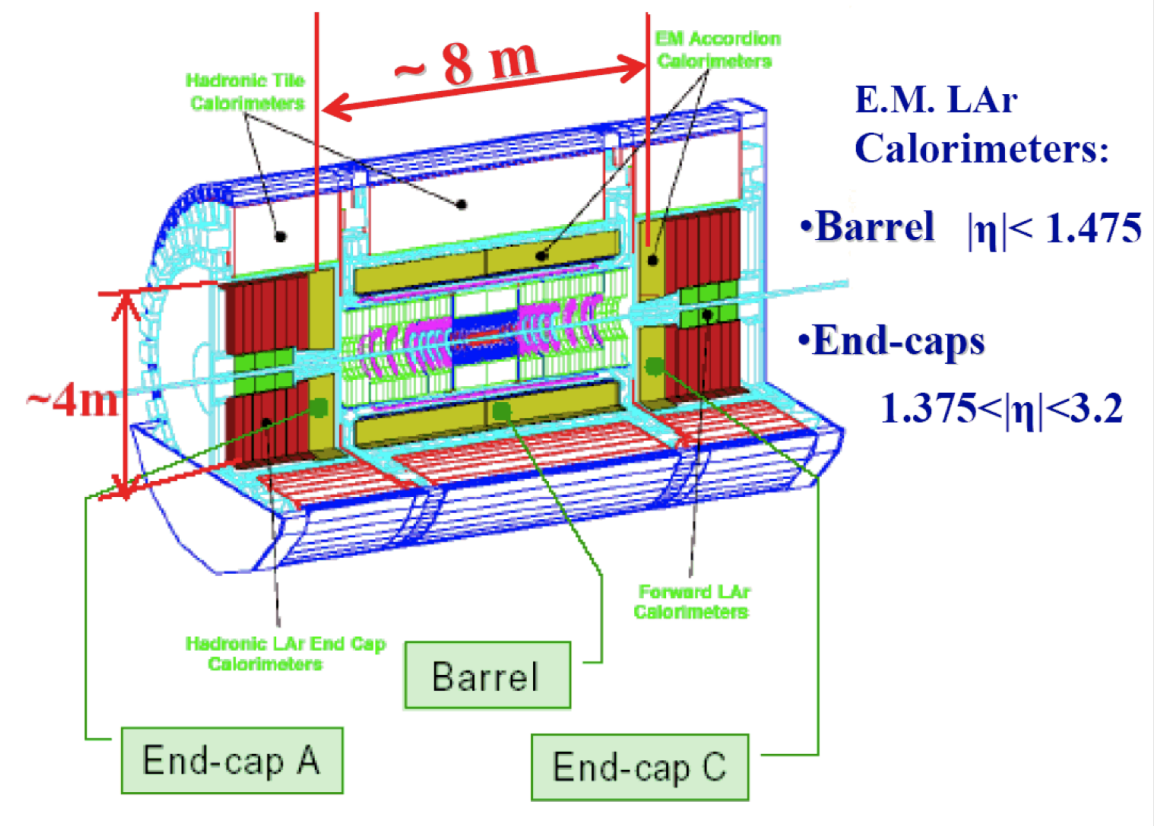

Figure 4.1: The a diagram of the ATLAS Calorimeter.

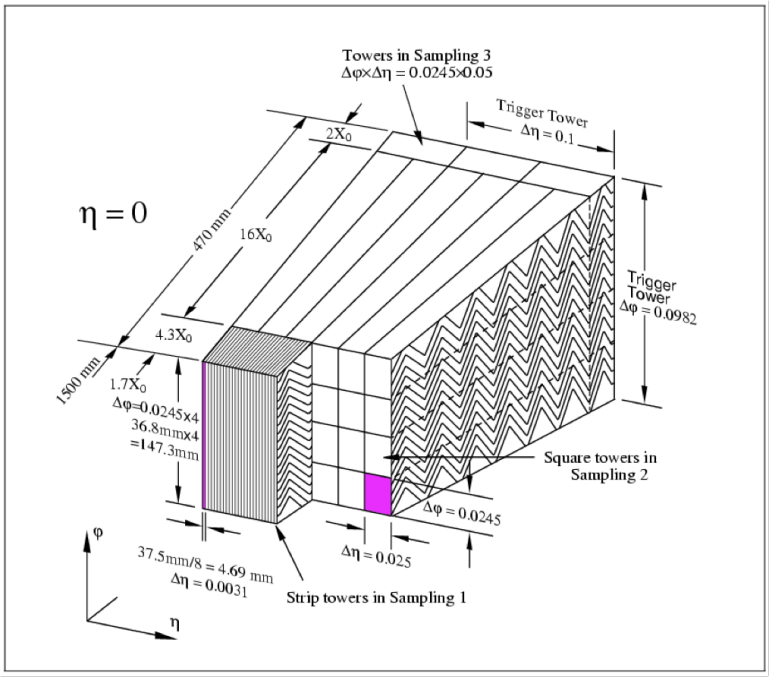

Figure 4.2: The a section of the ATLAS Calorimeter.

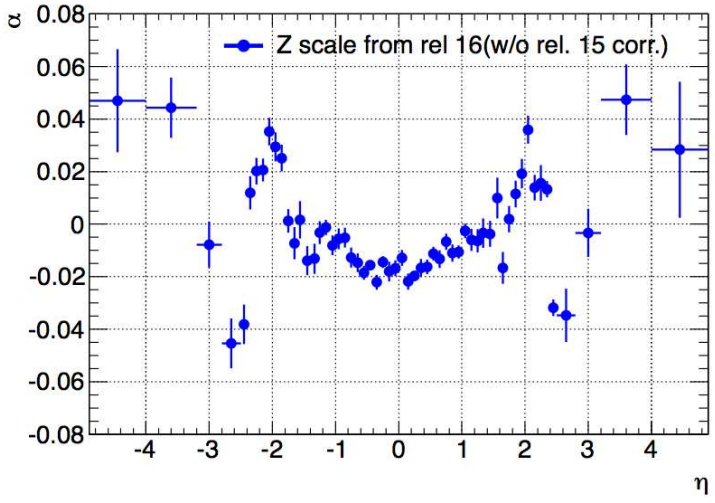

Figure 4.3: The calibration factors derived with the 2010 ATLAS data set, as a function of η. The correction factor is defined in Eq. 4.1.

Bibliography

[1] Description of the KS Test:
http://www.itl.nist.gov/div898/handbook/eda/section3/eda35g.htm

[2] D. Perkins. Introduction to High Energy Physics, 4th Edition. Cambridge University Press, 2000.

[3] S. Dawson. "Introduction to Electroweak Symmetry Breaking", arXiv:hep-ph/9901280v1. 12 Jan 1999

[4] S. Dawson. "Introduction to Electroweak Symmetry Breaking", arXiv:0812.2190v1 11 Dec 2008

[5] Particle Data Group. Particle Physics Booklet. July 2010.

[6] Elli Pomoni. Very helpful discussions. April- May, 2011.

[7] J. Thompson, "Introduction to Colliding Beams at Fermilab". FERMILAB-TM-1909.

[8] Leif Lönnblad, "Matching and Merging Matrix Elements with Parton Showers". Talk at MCnet/CTEQ Summer School, Debrecen, Hungary. Aug. 14, 2008.
http://conference.ippp.dur.ac.uk/conferenceDisplay.py?confId=156

[9] Mike Seymour, "Introduction to Monte Carlo Event Generators". Talk at MCnet/CTEQ Summer School, Debrecen, Hungary. Aug. 8-16, 2008.
http://conference.ippp.dur.ac.uk/conferenceDisplay.py?confId=156

[10] T. Sjostrand et al., Computer Phys. Commun. 135 (2001) 238;

[11] T. Sjostrand et al., arXiv: hep-ph/0108264. 1192

[12] The DØ Collaboration , V.M. Abazov et al., The Upgraded DØ Detector, Nucl. Inst. Meth. A 565 (2006) 463, arXiv:physics/0507191.

[13] A. Schwartzman, Fermilab-THESIS-2004-21 http://www-d0.fnal.gov/results/publications_talks/thesis/schwartzman/thesis.pdf

[14] A. Djouadi, J. Kalinowski, M. Spira, arXiv: (hep-ph) 9704448 (1997).

[15] R. Brun and F. Carminati, CERN Program Library Long Writeup W5013, 1993 (unpublished), version V3.21.

[16] J. Pumplin et al., J. High Energy Phys. 07 (2002) 12.

[17] MLM matching procedure, http://www-d0.fnal.gov/computing/MonteCarlo/generators/common alpgen.html

[18] J. Campbell and K. Ellis, "MCFM, Monte-Carlo for FeMtobarn processes, http://mcfm.fnal.gov/.

[19] Fabrice Couderc, April, 2011.

[20] TMVA Users Guide, CERN-OPEN-2007-007 and arXiv:physics/0703039.

[21] DØ note 5845-CONF "Search for the SM Higgs boson in that tautauqq final state". August 14, 2009.

[22] W. Fisher, Report No. FERMILAB-TM-2386-E, 2006.

[23] Begel, Schellman. "On averaging inelastic cross sections across experiments" (Information about the luminosity calculation) http://www-d0.fnal.gov/phys_id/luminosity/ notes/lm_notes/constant/inelastic_average/inelastic.ps

[24] Tevatron Operations Rookie Books. http://www-bdnew.fnal.gov/operations/rookie_books/rbooks.html

[25] ATLAS Collaboration, Expected Performance of the ATLAS Experiment - Detector, Trigger and Physics. CERN-OPEN-2008-020, Geneva.

[26] M. Aharrouche et al. Nucl. Inst. Meth. A582 (2007) 429-455.

[27] F. Berends et al., in Z physics at LEP 1, ed. G. Altarelli, R. Kleiss, and C. Verzegnassi, (CERN Report 89-08, 1989).

[28] F. Berends et al., in Z physics at LEP 1, ed. G. Altarelli, R. Kleiss, and C. Verzegnassi, (CERN Report 89-08, 1989).

[29] LEP Electroweak Working Group, Phys. Rep. 427 (2006) 257.

[30] Particle Data Group (S. Eidelman et al.), Phys. Lett. B592 (2004) 1.

[31] ATLAS Collaboration, Reconstruction and Identication of Electrons, CSC book: Expected Performance of the ATLAS Experiment - Detector, Trigger and Physics ATLAS Collaboration. CERN-OPEN-2008-020, Geneva.

Appendix A

Systematics

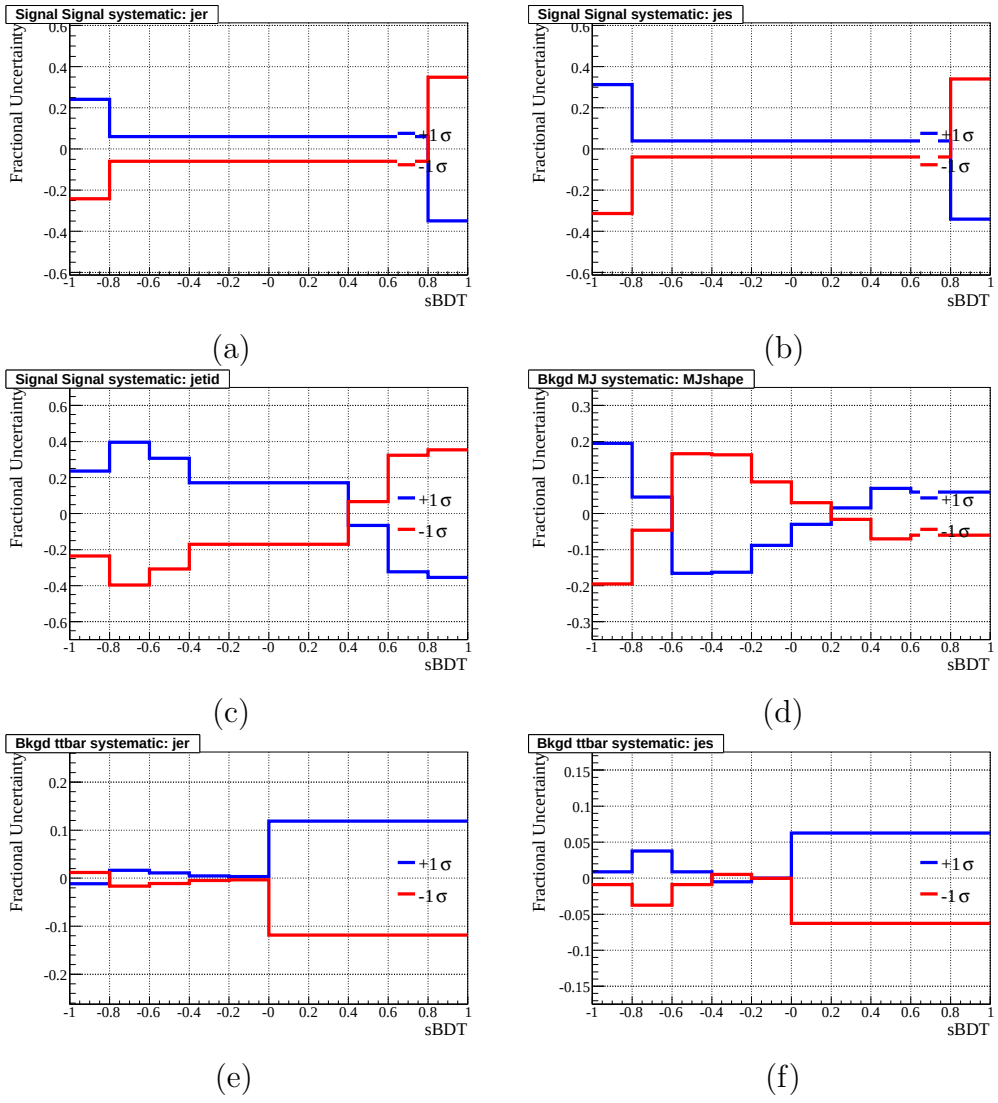

Figure A.1: Fractional systematic variations of the high mass cBDT for the signal due to (a) JER, (b) JES, (c) JetID, and for (d) the MJ background due to the MJ shape estimation, and for the $t\bar{t}$ background due to (b) JER and (d) JES.

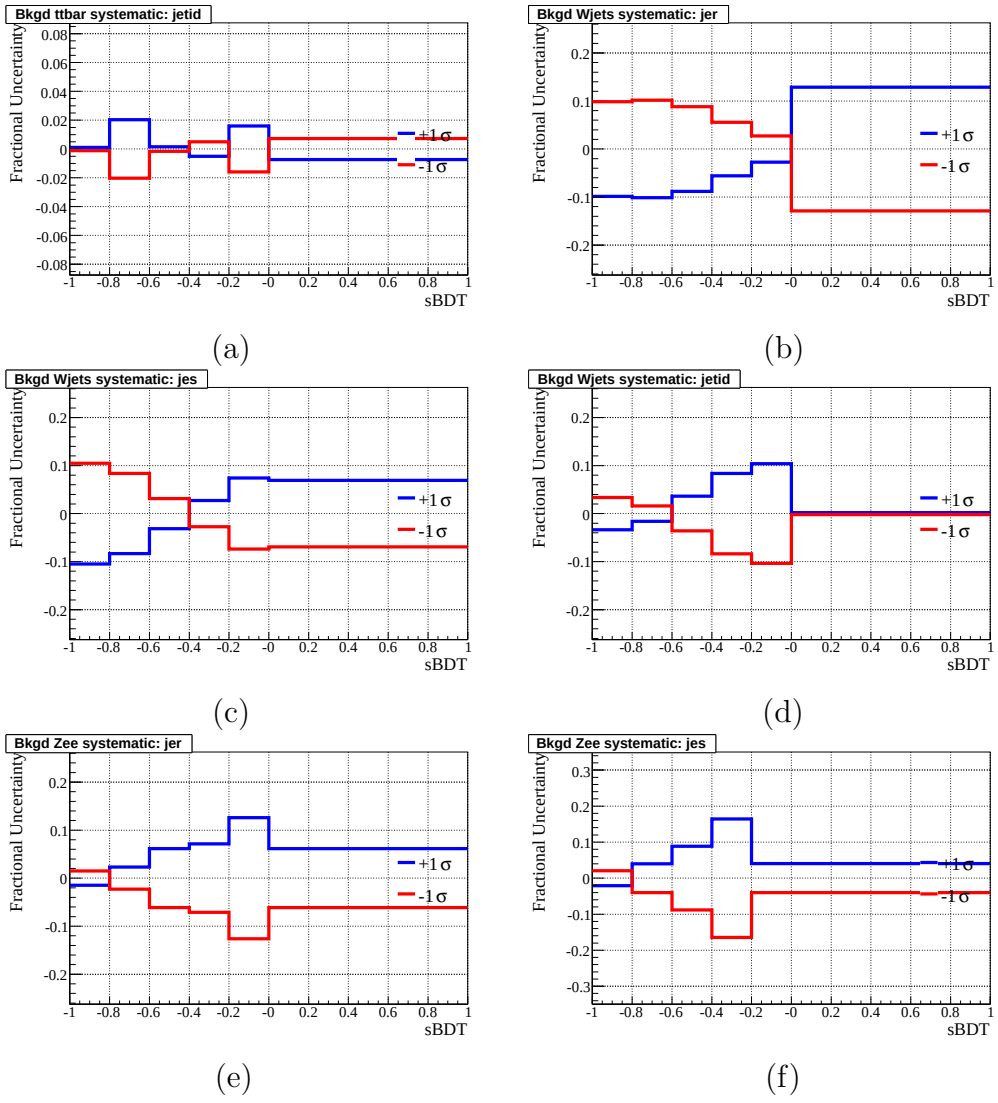

Figure A.2: Fractional systematic variations of the high mass cBDT for the (a) $t\bar{t}$ background due to JetID, for the $Wjets$ background due to (b) JER, (c) JES, and (d) JetID, and for the $Zjets$ background due to (e) JER, and (f) JES.

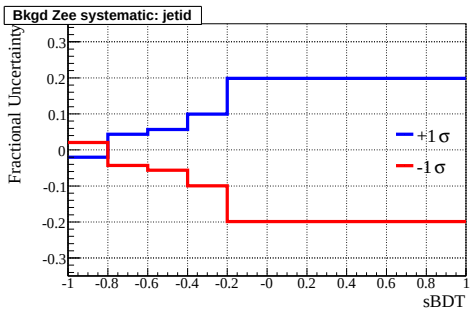

Figure A.3: Fractional systematic variations of the high mass cBDT for the (a) $Zjets$ background due to JetID.

Appendix B

Appendix: Zee Calibration at ATLAS

Presented here is the note describing the proposed calibration of the ATLAS LAr Calorimeter using Zee events written in 2008 using Monte Carlo simulation and published in: [25].

B.0.1 Motivation

The calorimeter resolution is given by

$$\frac{\sigma_E}{E} = \frac{A}{\sqrt{E}} \oplus \frac{B}{E} \oplus C. \tag{B.1}$$

The coefficient A is referred to as the sampling term, B, as the noise term, and C, as the constant term. In the EM calorimeter, the construction tolerances and the calibration system ensure that the response is locally uniform, with a constant term $< 0.5\%$ over regions of size $\Delta\eta \times \Delta\phi = 0.2 \times 0.4$. This has been shown with test beam data [26]. Electron pairs from Z boson decays can then be used to intercalibrate the 384 regions of such size within the acceptance of $|\eta|$ <2.4. These regions must be intercalibrated to within 0.5% in order to achieve a desired global constant term of $< 0.7\%$. The basic idea of this calibration method is to constrain the di-electron invariant mass distribution to the well-known Z boson lineshape. A second goal of the calibration is to provide the absolute calorimeter electromagnetic energy scale. This must be known to an accuracy of $< 0.1\%$ in order to achieve the ATLAS physics goals.

B.0.2 Description of the method

Long-range non-uniformities can arise for many reasons, including variations, impurities and temperature changes in the liquid argon, the amount of up-stream material, mechanical deformations, and changes in high voltage

(as localized calorimeter defects may necessitate operating a small number of channels below nominal voltage). For a given region, i, we parametrize the long-range non-uniformity modifying the measured electron energy as $E_i^{reco} = E_i^{true}(1 + \alpha_i)$. Neglecting second-order terms and supposing that the angle between the two electrons is perfectly known, the effect on the di-electron invariant mass is:

$$M_{ij}^{reco} \simeq M_{ij}^{true}(1 + \frac{\alpha_i + \alpha_j}{2} = M_{ij}^{true}(1 + \frac{\beta_{ij}}{2}), \tag{B.2}$$

where $\beta_{ij} \equiv \alpha_i + \alpha j$.

The method to extract the α's is fully described in [27] and is done in two steps. First, the β's are determined, then the α's. For a given pair of regions (i, j), the coefcient β_{ij} and its associated uncertainty are determined by minimizing the following log-likelihood:

$$-\ln L_{tot} = \sum_{k=1}^{N_{ij}} -\ln L(M_k/(1 + \frac{\beta_{ij}}{2}), \sigma_{M,k}) \tag{B.3}$$

where k counts all selected events populating the pair of regions (i, j), M_k is the di-electron invariant mass of event k, and $L(M, \sigma_M)$ quantifies the compatibility of an event with the Z boson line shape and is described below. Fits with only one event are removed. Once the β's are determined from the minimization, the α's can be found from the overdetermined linear system given by $\beta_{ij} \equiv \alpha_i + \alpha_j$. This is done using a generalized least squares method, and gives an analytic solution. The Z boson line shape is modeled with a relativistic Breit-Wigner distribution [28] [29]:

$$BW(M) \sim \frac{M^2}{(M^2 - M_Z^2)^2 + \Gamma_Z^2 M^4 / M_Z^2} \tag{B.4}$$

where M_Z and Γ_Z are the mass and the width of the Z boson. They were measured precisely at LEP; the values used are, respectively, 91.188 ± 0.002 GeV and 2.495 ± 0.002 GeV [30]. In proton-proton collisions, the mass spectrum of the Z boson differs from the Breit-Wigner shape of the partonic process cross section. The probability that a quark and antiquark in the interacting pp system produce an object of mass M falls with increasing mass. In order to take this into account, the Breit-Wigner is multiplied by the ad-hoc parametrization $\mathcal{L}(M) = 1/M^\beta$. The parton luminosity parameter β is assumed to be a constant and is determined by fitting the Z boson mass distribution obtained with events generated with PYTHIA version 6.403 [10]. Figure B.1 shows the Z boson mass distribution fitted with a Breit-Wigner with and without the

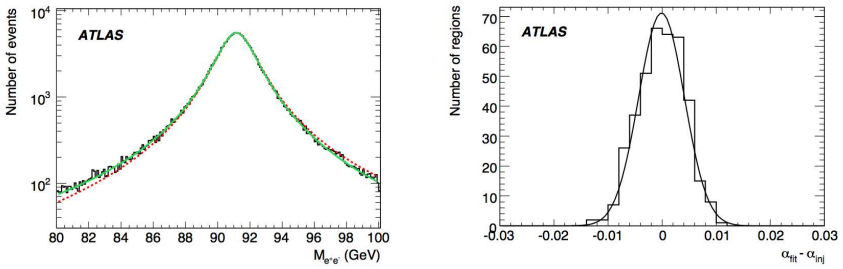

(a) (b)

Figure B.1: (a) The Z line shape, for PYTHIA events fitted with a Breit-Wigner distribution with (solid line) and without (dashed line) the parton luminosity factor. χ^2/N_{DOF} is 1.09 and 3.96, respectively. (b) Residual distribution fitted with a Gaussian.

parton luminosity factor. The fitted value of the parameter β is 1.59 $\pm$ 0.10; this will be used in the following. Since the photon propagator and the interference term between the photon and the Z boson were not taken into account in the previous parametrization, the parton luminosity term also accounts for the effects of these two terms. Finally, in order to take into account the finite resolution of the electromagnetic calorimeter, the Breit-Wigner multiplied by the parton luminosity term is convoluted with a Gaussian:

$$L(M, \sigma_M) = \int_{-\infty}^{+\infty} BW(M-u)\mathcal{L}(M-u)\frac{e^{-u^2/2\sigma_M^2}}{\sqrt{2\pi}\sigma_M}du \tag{B.5}$$

where σ_M is the resolution of the measured mass. It is related to the electron energy resolution via

$$\frac{\sigma_M}{M} = \frac{1}{2}\sqrt{(\frac{\sigma_{E_1}}{E_1})^2 + (\frac{\sigma_{E_2}}{E_2})^2} \tag{B.6}$$

At $|\eta| = 0.3$, the sampling term of the electron energy resolution is equal to 10.0% and increases with increasing $|\eta|$. Technically, the integral is converted to a discrete summation over the convolution parameter u which takes values between $-5\sigma_M$ and $+5\sigma_M$.

B.0.3 Generator-level tests

The method is first tested on generator-level $Z \to ee$ Monte Carlo events. These were generated using PYTHIA 6.403 with $M_Z = 91.19$ GeV and $\Gamma_Z =$

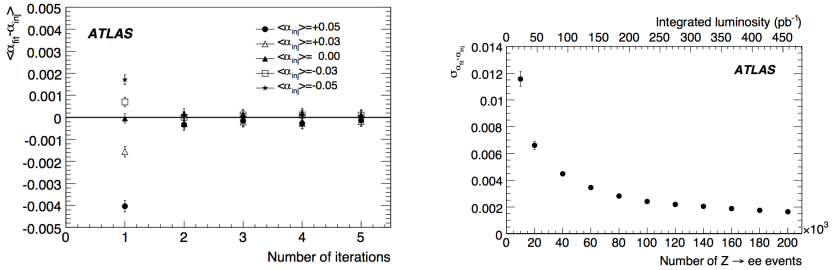

(a) (b)

Figure B.2: (a) Mean value of the Gaussian fitting the residual distribution as a function of the number of iterations for different mean values of the injected α's; (b) Constant term as a function of the number of events or as a function of the luminosity.

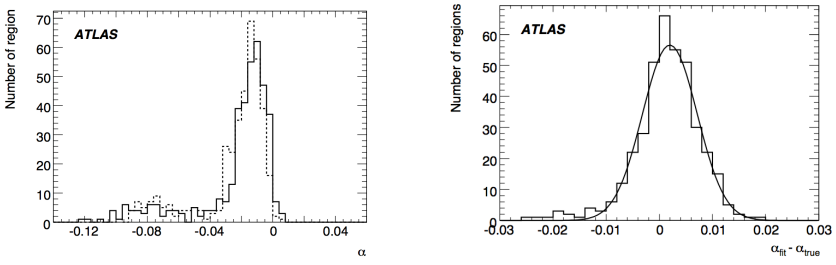

(a)α_{fit}(solid), α_{true}(dashed) (b)α_{fit}-α_{true}

Figure B.3: Fit results with distorted geometry and α_{inj} =0.

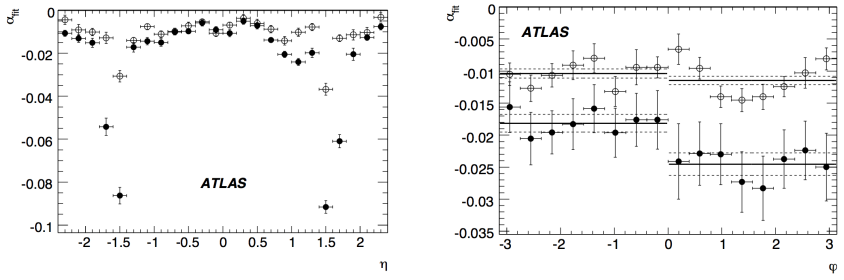

(a) (b)

Figure B.4: α_{fit} distributions with α_{inj}=0 and with distorted(ideal) geometry shown in full(open) circles. Figure (a) shows α_{fit} integrated over ϕ as a function of η. Figure (b) shows α_{fit} integrated over η as a function of ϕ, fitted in two separate regions.

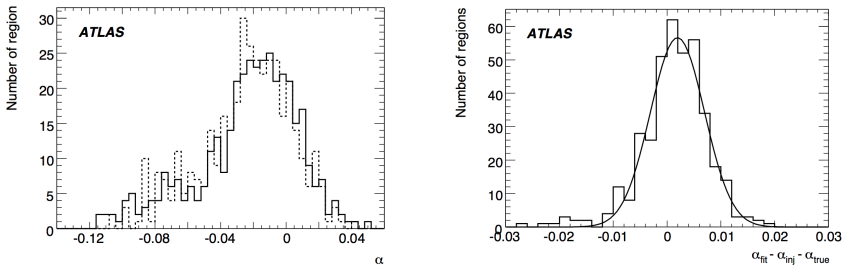

(a) α_{fit} and α_{true}+α_{inj} (dashed) (b)α_{fit} - (α_{true}+α_{inj})

Figure B.5: Fit results with distorted geometry and additional injected biases.

2.495 GeV. Events are required to have at least one electron with $p_T > 10$ GeV and $|\eta|$ <2.7 and a di-electron invariant mass $M_{ee} > 60$ GeV. To simulate the detector resolution, generated electron energies are smeared to obtain $\sigma_E/E = 10\%/\sqrt{E}$.

For each calorimeter region, i, a bias, α_i, is generated from a Gaussian distribution with a mean μ_{bias} and width σ_{bias}. These will be called the injected α's, α_{inj}. For the first tests, μ_{bias} is fixed to 0 and σ_{bias} to 2%. The calibration method explained above is applied to 50,000 events after selection. The residual distribution $(\alpha_{fit} - \alpha_{inj})$ is shown in Fig. B.1(b). The mean value of the residual distribution corresponds to the energy scale, and its width to the energy resolution. Thus it can be seen that the fitting method gives unbiased estimators of the injected αs.

In the case where μ_{bias} is different from zero, the mean value of the residual distribution will be different from zero. For example, for μ_{bias} = -3%, $\langle \alpha_{fit} - \alpha_{inj} \rangle = 0.1\%$. This is a consequence of neglecting the higher-order terms in the Taylor expansion of Eq. B.2. Iterating the procedure twice suffices to recover an unbiased estimate of the α's, as shown in Fig. B.2(a). Figure B.2(b) also shows the resulting uniformity. After the fit, the RMS of the distribution has been reduced from 2% to 0.4%. The RMS of the residual distribution is a measure of the expected long- range constant term. Figure B.2(b) shows the long-range constant term as a function of the number of reconstructed $Z \rightarrow ee$ decays or of the integrated luminosity assuming an event selection efciency of 25%. Therefore, by summing the local constant term of 0.5% with the long-range constant term of 0.4% obtained here, a total constant term of about 0.7% could be achieved with ≈100 pb^{-1}. These results assume perfect knowledge of the material in front of the electromagnetic calorimeter.

B.0.4 Results with distorted geometry

The previous section showed results based on generator-level Monte Carlo. The results in this section use PYTHIA events with full detector simulation and reconstruction, using a geometry with additional material in front of the electromagnetic calorimeter.

The number of events available is 349,450 corresponding to an integrated luminosity of ≈200 pb^{-1}. Events with at least two reconstructed electrons are kept. The two leading electrons are required to be of at least medium quality [31], to have $p_T > 20$ GeV and $|\eta| < 2.4$, and to be of opposite sign. Finally, the di-electron invariant mass is required to be within $80 < M_{ee} < 100$ GeV. The total selection efciency is 21.5%; the efficiency for finding two electron candidates within $|\eta| < 2.4$ is 50%. The calibration method is applied rst

without injecting any biases ($\alpha_{inj} = 0$ for all regions). However, the presence of the misalignments and extra material means that there will be some biases intrinsic to the simulation. These true biases can be estimated using generator information:

$$\alpha_{true,i} = \frac{1}{N_i} \sum_{k}^{N_i} \frac{p_T^{reco,k} - p_T^{gen,k}}{p_T^{gen,k}} \tag{B.7}$$

where k counts over the N_i electrons falling in region i, and $p_T^{reco,k}$ and $p_T^{gen,k}$ are the reconstructed and true transverse momenta of electron k. The distribution of α_{true} is shown in Fig. B.3(a), as is the results of the fit. The low-end tail corresponds to regions located in the gap between the barrel and end- cap cryostats (Fig. B.4(a)), where the density of material has been increased by a factor of 1.7. There is fair agreement between the α's extracted using the data-driven method and those estimated from generator information. Figure B.3(b) shows the difference between α_{fit} and α_{true}; a Gaussian fitted to this distribution has a mean of 0.1% and a width of 0.5%. The distribution of α_{fit} as a function of η and ϕ is shown in Fig. B.4 for the ideal and distorted geometries. The asymmetry between positive and negative ϕ is due to the effect of the extra material in the inner detector at positive ϕ. The difference between positive and negative ϕ values is about 0.6%.

The same exercise is also done by introducing, on top of the non-uniformities due to extra material, a bias α_{inj} generated from a Gaussian distribution with a mean $\mu_{bias} = 0$ and width $\sigma_{bias} = 2\%$. Results are shown in Fig. B.5. The Gaussian tted to this distribution also has a mean of 0.1% and a width of 0.5%.

One can conclude that, using ≈87, 000 reconstructed $Z \to ee$ events (which corresponds to about 200 pb^{-1}), and with an initial spread of 2% from region to region, the long-range constant term should not be greater than 0.5%. This should give an overall constant term ≈0.7%. The bias on the absolute energy should be small and of the order of 0.2%. If the exercise is repeated with only 100 pb^{-1} of data, the Gaussian fitted to the residual distribution also has a mean of 0.2%, but the width is larger, leading to a long-range constant term of 0.8%.

B.0.5 Estimation of the systematic uncertainty on the energy scale

The absolute energy scale has been obtained using electrons from $Z \to ee$ decays. It has been determined on events simulated with the misaligned

geometry while the longitudinal weights were found with the ideal geometry. On top of the non-uniformities due to extra material, a bias modeling the calorimeter non-uniformities is introduced and is generated from a Gaussian distribution with a mean $\mu_{bias} = 0$ and width $\sigma_{bias} = 2\%$. The resulting bias on the energy scale can be assessed by comparing the tted αs with those from generator information; the bias is equal to 0.2%. This bias is understood and is due to the fact that the model of the Z boson line shape does not take into account the effects of bremsstrahlung. Work is ongoing to improve this deficiency.

The background has been neglected but it has been checked that the contribution from QCD events where the two jets are misidentied as electrons is small. Thus, it should have a negligible effect on the determination on the energy scale.

Electrons from Z boson decays have a p_T spectrum with a maximum value around 45 GeV. Care will thus have to be taken to extrapolate the calibration obtained from $Z \rightarrow ee$ decays to electron energy regions not well populated by these events. Corrections determined with Z boson decays were applied to single electron samples with different generated transverse momenta (20, 40, 120, and 500 GeV) reconstructed with the misaligned geometry. Figure B.6 shows $\langle \alpha_{true} \rangle$ after correction as a function of p_T for four $|\eta|$ bins. In principle, $\langle \alpha_{true} \rangle$ should be equal to zero. This is true for the 40 GeV electron sample at a level of 0.2% excep$_T$ in the bin ($1.4 < |\eta| < 2.0$) containing the crack region. For central electrons ($|\eta| < 0.6$), the dependence versus p_T is smaller than 0.5%. The effect is worse for non-central electrons. For instance, at $p_T = 120$ GeV, α_{true} after corrections varies from 1 to 1.6 percent. This non-linearity is due to the presence of extra material in front of the calorimeter.

To conclude, at the Z boson energy scale, the estimate of the systematic uncertainty is around 0.2%. At other energy scales, the systematic uncertainty is dominated by effects of extra material. For central electrons, corrections can be extrapolated over the full p_T spectrum to a level of 0.5%. The linearity is degraded for non-central electrons at a level of 1 or 2 percent except in the crack region where it is worse. These numbers depend on the amount of extra material added to the misaligned geometry compared to the ideal geometry and will likely be different with real data.

The performance presented here corresponds to our current understanding of the determination of the absolute energy scale. Improvements are expected to achieve systematic uncertainties smaller than 0.5%. For instance, including information from the E / p ratio measured for isolated high-p_T electrons from $W \rightarrow e\nu$ decays will compliment the direct calibration of the absolute scale with $Z \rightarrow ee$ events. Photon conversions can also help to determine the

amount of material in front of the calorimeter.

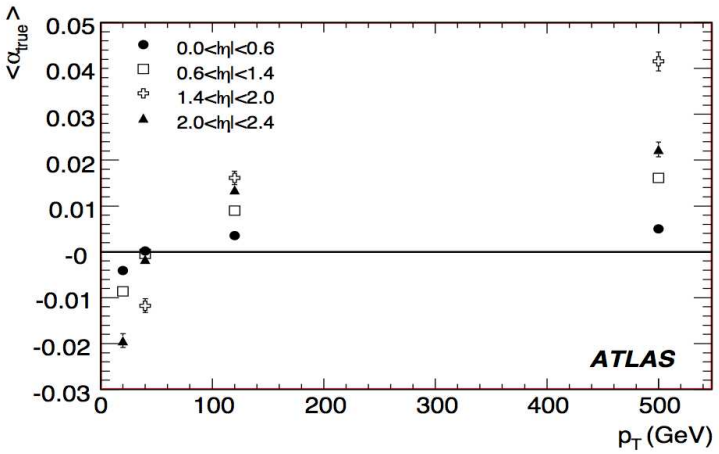

Figure B.6: $\langle \alpha_{true} \rangle$ after correction as a function of p_T for four η bins.